Alma Mater Studiorum - Università di Bologna

Dottorato di Ricerca in Ingegneria Elettronica, Telecomunicazioni e Tecnologie dell'Informazione

35° Ciclo

Settore Concorsuale: 09/F1
Settore Scientifico Disciplinare: ING-INF/02
CAMPI ELETTROMAGNETICI

Radiation Characteristics Enhancement of Planar Structures using Metasurfaces

Presentata da:
Shobit Agarwal
Supervisore:
Prof. Alessandra Costanzo
Prof. Diego Masotti

Coordinatore Dottorato:
Prof. Aldo Romani

Esame Finale Anno 2023

Author:
Shobit Agarwal

Supervisors:
Prof. Alessandra Costanzo
Prof. Diego Masotti

Institute:
Alma Mater Studiorum - Università di Bologna, Bologna campus, Italy

CONTENTS

LIST OF FIGURES

LIST OF TABLES

ABSTRACT

In view of the need for communications with distributed sensors/nodes, this thesis presents a collective study of metasurfaces applications in enhancing the radiation characteristics of antennas as well as in EM wave manipulation such as polarization conversion and anomalous reflection. This thesis presents the design of a single-port antenna with dual-mode operation and metasurfaces exploitation, which represents the front-end of a future-generation tag acting as a position sensor with identification and energy harvesting capabilities. An Archimedean spiral covers the lower European Ultra Wideband (UWB) frequency range for communication/-localization purposes, whereas a non-standard dipole operates in the Ultra High Frequency (UHF) band to wirelessly receive the energy. The objective is to have a low-profile stack-up that is insensitive to the background material. Because of their ability to manipulate EM waves, metasurfaces have piqued the interest of researchers worldwide. One such application of metasurface is used to guarantee the versatility of the proposed antenna by employing a High Impedance Surface (HIS). A conformal design, supported by 3D-printing technology, is pursued to check the versatility of the proposed architecture in view of any application involving its deformation and tracking/powering operations.

In addition, this thesis discussed two different applications of metasurfaces. One of them is focused on the designing of a polarization converter, while the other discusses an Intelligent Reflective Surface (IRS) for anomalous reflection.

The first application discusses the designing of an angularly stable super wideband Cross Polarization Conversion (CPC). The reported metasurface consists of a square Split Ring Resonator (SRR) and a circular SRR each having two cuts in

adjacent sides for polarization conversion purposes. The proposed metasurface is operating within 11 - 35GHz and having a relative impedance bandwidth of 104.3%. The design shows a stable response for oblique incidence up to 40 degrees. The Polarization Conversion Ratio (PCR) of the proposed metasurface is above 62% within the entire operating band.

The second application involves the design of an intelligent reflective surface that propagates the incoming wave in a non-conventional direction. The tunability of the IRS is achieved through an artificially developed ferroelectric material Zirconium-doped Hafnium Oxide (HfZrO). In addition to this, distributed capacitive elements (Inter-Digitated Capacitor (IDC)) are employed to tune the impedance and phase response of each meta atom. It is shown that the proposed IRS provides an anomalous reflection for normal incident waves.

ACKNOWLEDGMENTS

This work would not have been possible without all the help and support provided by others. During my time here in Italy and in particular at the Alma Mater Studiorum - Università di Bologna, I had the honor of meeting a lot of interesting people, many of whom became friends. To all of you, I hereby say: *Thank You for everything! This would not have been possible without you!* However, there are a couple of individuals who deserve special mention.

Firstly, I would like to thank my supervisor **Prof. Alessandra Costanzo** for providing me this opportunity. She was always available in the hour of need and provided optimized solutions. I must admit that she brings out the best character of yourself. I also want to thank my co-supervisor **Prof. Diego Masotti** for his continuous discussions about my research and personal life experiences. I really enjoyed working with him and I have not seen such a humble man like him.

Furthermore, I also want to thank all the members of the *Alma Mater Studiorum - Università di Bologna Electromagnetic research group* for the many discussions and valuable inputs along the way. The research group invovles Dr. Giacomo Paolini, Dr. Francesca Benassi, Dr. Ghulam Murtaza, Dr. Mazen Shanawani, Mr. Enrico Fazzini, Mr. Simone Trovarello and other MS students. I enjoyed my time with these people in technical discussions as well as enjoying life outside the campus.

I also want to thank my wife **Manisha**, who took care of my parents and her pregnancy during the many days and nights that I spent in Italy and welcomed me with open arms filled with endless love whenever I visited India.

DEDICATION

To my family without which a person is nothing !

ACRONYMS

AR	Axial Ratio
balun	Balanced To Unbalanced Unit
CP	Circular Polarization
CPC	Cross Polarization Conversion
DSRR	Double Split Ring Resonator
EH	Energy Harvesting
EM	ElectroMagnetic
FBR	Front-to-back Ratio
FCC	Federal Communications Commission
HfZrO	Zirconium-doped Hafnium Oxide
HIS	High Impedance Surface
HRP	High Rate Pulse Repetition Frequency
IDC	Inter-Digitated Capacitor
IR-UWB	Impulse Radio-Ultra Wideband
IRS	Intelligent Reflective Surface
LHM	Left Handed Metamaterial
MS	Metasurface
NIM	Negative Index Material
PCR	Polarization Conversion Ratio
PEC	Perfect Electric Conductor

PMC	Perfect Magnetic Conductor
PNA	Power Network Analyzer
RF	Radio Frequency
RFID	Radio Frequency Identification
SRR	Split Ring Resonator
SWB	Super Wideband
UHF	Ultra High Frequency
UWB	Ultra Wideband
WPT	Wireless Power Transfer

1

INTRODUCTION

OBJECTIVE

The chapter discusses a brief history of the research objectives of this thesis. Metasurface (MS), one of the thrust research areas, has gained a lot of attention in recent years due to their wide range of applications. In this thesis, MSs are exploited for three different applications viz. back radiation shielding of planar antennas, cross-polarization conversion, and IRS for anomalous reflections. The author believes this thesis provides an in-depth study of interesting and diverse research problems.

1.1 ULTRA WIDE BAND SYSTEMS: INTRODUCTION TO INNOVATIONS

Ultra Wideband (UWB) signals are typically defined as having an instantaneous spectral occupancy of more than 500 MHz or a fractional bandwidth of more than 20% [1]. To generate these signals, an antenna is typically powered by extremely short-duration electrical pulses (duration on the order of one nanosecond or less). Further, Impulse Radio-Ultra Wideband (IR-UWB) systems, which are also based on very short-duration / high bandwidth pulses, have been the focus of a lot of recent research and development in the field of wireless communications. UWB systems have been around for some time. Actually, they predate all other radio communication methods by many decades. Heinrich Hertz constructed the first

experimental spark-gap transmitter in 1887 to verify Maxwell's theory of Electro-Magnetic (EM) waves [2]. Transatlantic impulse transmissions in 1901 were made possible by the telegraph systems that Guglielmo Marconi developed. Fifty years after Marconi's inventions, radar applications using impulse radio transmissions became more common, most notably in the military [3].

The United States government issued the First Report and Order in the year 2002 in which the commercialization of UWB technology and the use of UWB devices without a licence was approved by the Federal Communications Commission (FCC). Between 3.1 and 10.6 GHz, the FCC allocated a band of the unlicensed radio spectrum with a maximum power spectral density of -41.3 dBm/MHz; a separate spectral mask was assigned to each device class, allowing UWB radios to function by superimposing coexisting Radio Frequency (RF) systems, as shown in Fig. 1.1 where total spectrum is divided into three broad ranges: sub-GHz channel, low-band High Rate Pulse Repetition Frequency (HRP), and high-band HRP UWB channels denoted by band group 0, 1, and 2, respectively [1]. Concerning Europe, it is essential to remember that on February 21, 2007, a decision was published by the European Communities Commission to allow the radio spectrum to be used for equipment employing UWB technology in a coordinated fashion across the European Union community [4].

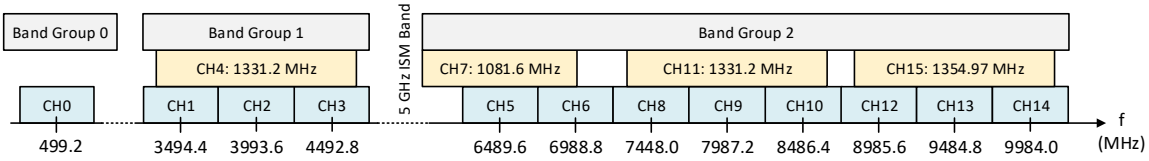

Figure 1.1: UWB spectrum band allocation.[1]

With the exponential growth of mobile devices like smartphones, tablets, etc., there is a desire to achieve wireless and automatic power, as mobile devices require regular recharging. Some proven ways to charge these gadgets include inductive or resonant coupling [5, 6]. However, these methods are not very useful in many real-world contexts as the charger and the unit have to be in close proximity. Energy-efficient connectivity, which can be achieved through RF Energy Harvesting (EH)

or Wireless Power Transfer (WPT) technology, is another major obstacle to the development of future wireless networks. This kind of technology can extend the battery life span, making it useful for potential wireless devices.

In this thesis, a UWB antenna is part of the preliminary activity: its characteristic is to be a dual-mode antenna working also in the UHF band (for energy autonomy reasons) and to have just a single input port.

1.1.1 *RFID Technology*

Radio Frequency Identification (RFID) is a type of Automatic Identification (AutoID) technology that identifies objects through the exchange of data between a tag and a reader using radio waves. Real-time item recognition using RFID technology is becoming increasingly popular in a variety of industries, including logistics, automotive, surveillance, automation systems, etc. [7]. The components of an RFID system are readers and tags. To access the data on the tags that are affixed to the items, the reader uses a wireless connection to interrogate them. A schematic representation of the basic RFID system is shown in Fig. 1.2. Passive or semi-passive RFID tags, in which the energy required for tag-reader communication is gathered from the reader's signal or the surrounding environment, are the least expensive RFID tags with the most economic potential. Based on backscatter modulation, passive RFID tags modify their antenna reflection characteristics in response to information input [8].

More advanced RFID systems in the future should be able to precisely localize tags and provide trustworthy identification. Accurate submeter-level real-time localization, tag management for a large number of tags, extremely low power consumption, a small footprint, and an affordable cost will emerge as new critical issues [9]. Unfortunately, current RFID [10], wireless sensor network (WSN) [11] technologies, such as those based on the ZigBee standard, are only able to partially meet the majority of these requirements. RFID systems that rely on tradi-

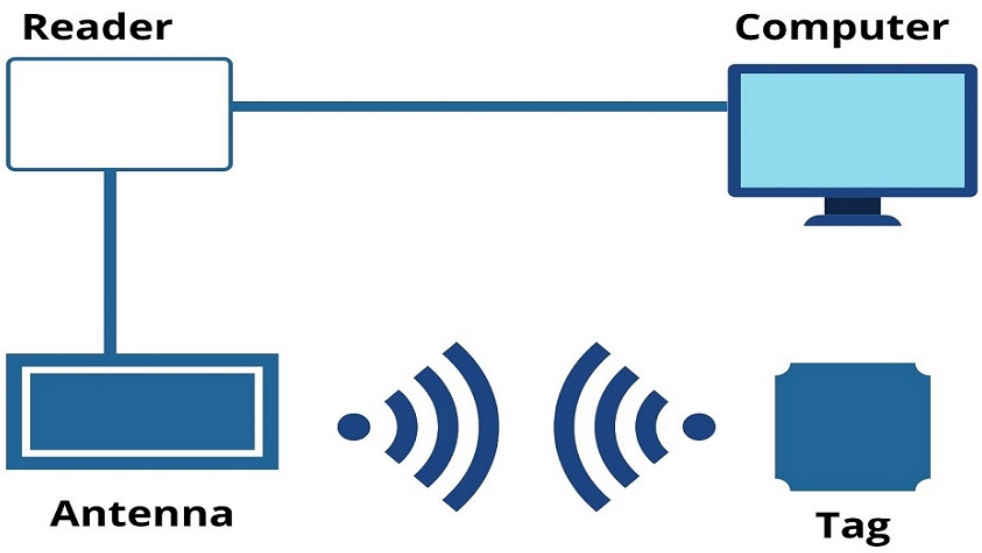

Figure 1.2: Components of an RFID system.

tional continuous wave-oriented communication in the UHF band are inherently insecure because of issues like multipath signal cancellation (caused by the signal's extremely narrow bandwidth) and narrowband interference[7, 12–14].

In its IR-UWB implementation, the UWB technology, which is characterized by the transmission of pulses with a length that is sub-nanosecond in duration, is a promising technology for a wireless solution for the next-generation RFID. Wideband transmissions have the ability to resolve multipath, reduce frequency-dependent fading, and provide very accurate localization based on estimates of signal time-of-arrival. UWB's potential advantages include, but are not limited to, low transmitter power consumption, extremely accurate submeter-level ranging and positioning capability, multipath robustness (better area coverage), low detection probability (higher security), multiple devices operating simultaneously in confined spaces, and large numbers of devices (efficient multiple channel access and interference mitigation) [13, 15–17].

Even though passive methods based on back-scatter signalling seem to be superior when cheap cost and compact size criteria become mandatory, IR-UWB transmitters have been successfully used for active tags because of their low power

consumption [18]. However, back-scatter modulation-based UWB RFID systems are still in their infancy, and there are a number of concerns that need to be looked at [19].

Therefore, hybrid RFID tags can be used as a possible solution that can be powered using energy harvested in UHF band, while the UWB band is used for passive localization and communication. The IR-UWB and RFID technologies are combined in this thesis to provide a promising solution for future-generation RFID tags with both localization and energy autonomy capabilities.

1.2 METAMATERIALS: ARTIFICIAL MATERIALS TO MANIPULATE THE PROPAGATION OF EM WAVES

Metamaterials were not the first successful medium to employ synthetic components to produce particular EM responses. In reality, Jagadish Chandra Bose used twisted copper wires in a microwave experiment to examine polarization as early as 1898 [20]. With Bell Labs research, particularly Kock's metallic delay lens [21], the idea of artificial dielectrics really took off in the 1940s and persisted throughout the century. Additionally, the history of artificial magnetism, or magnetism produced without magnetic components, may be discovered in a textbook on classical antennas [22]. Since the 1960s, artificial plasmas or artificially created media with negative permittivity ($\varepsilon(\omega)$) have been discovered [23, 24]. However, the majority see the debut of John Pendry's artificial magnetism in 1999 [25] and the important publication numerically analyzing the first structure with concurrently negative $\varepsilon(\omega)$ and negative permeability ($\mu(\omega)$) as the "genesis" of metamaterials. These articles established a paradigm change that made it possible for artificial materials, which Walser later referred to as metamaterials [26], to acquire more exotic characteristics than their forebears throughout a wider span of the EM spectrum, notably into much shorter wavelengths. A standard metamaterials classification based on permittivity and permeability is shown in Fig. 1.3 where DPS, EMG, DNG and

MNG correspond to double positive, epsilon negative, double negative and mu negative materials, respectively. The desired metamaterials of this work fall under the DNG category. Additionally, the dielectric properties of a material are defined using ε and μ. In general, there are two values for each ε and μ that are known as relative/real (ε_{rel}, μ_{rel}) and effective (ε_{eff}, μ_{eff}). Real permittivity and permeability are intrinsic properties of a material which characterize its ability to store electrical and magnetic energy, respectively. On the other hand, effective permittivity and permeability are composite parameters that consider the contributions of the constituent materials and their arrangement. They are important parameters in the design and analysis of EM devices and the study of EM wave propagation through materials.

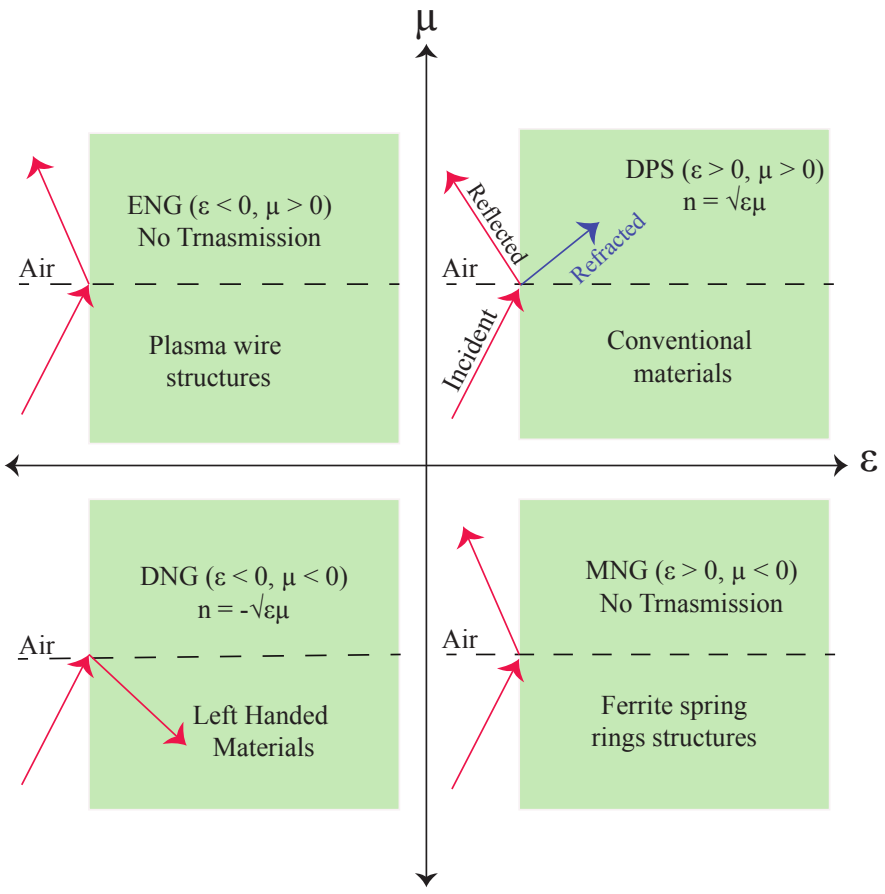

Figure 1.3: Metamaterials classification based on permittivity and permeability. Reproduced from [27]

John Pendry published a study on a magnetic substance made up of nonmagnetic resonant components in 1999 [25]. While most natural materials were con-

strained to interact strongly with magnetic fields at low frequencies, Pendry was able to tailor the response to higher frequencies because these structures had a tunable magnetic response. The Double Split Ring Resonator (DSRR), shown in Fig. 1.4, was one of many magnetic metamaterials described by Pendry that gained the most traction in the field and produced a frequency band of negative $\mu_{eff}\ (\omega)$ in the microwave regime. In 2000, Smith developed a Negative Index Material (NIM),

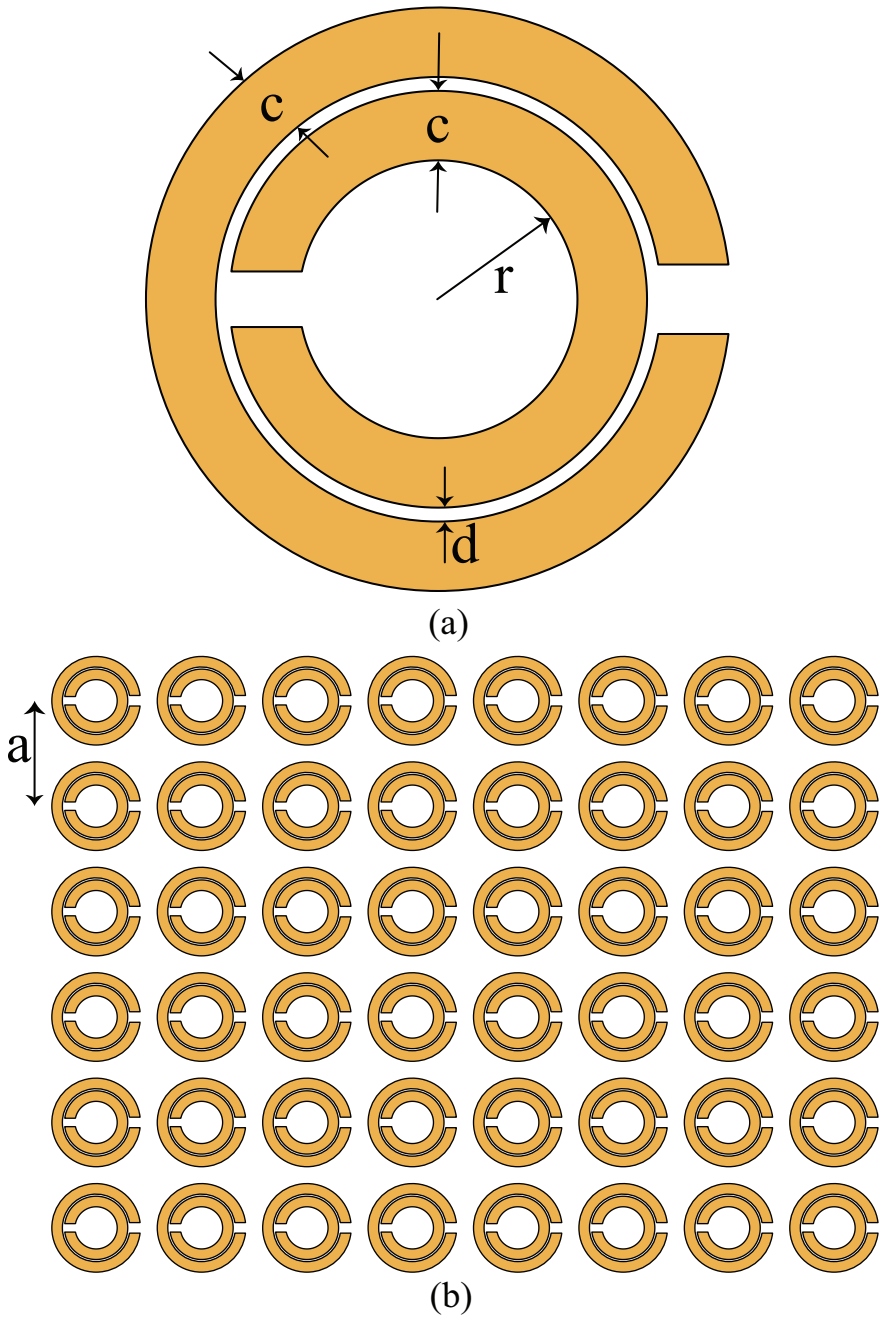

Figure 1.4: Design of double split ring resonator behaving as a negative index metamaterial (a) unit cell (b) square array (a=10mm, r=2mm, c=1mm, d=0.1mm). Redrawn from [25]

which is a substance with concurrently negative values of $\varepsilon_{eff}(\omega)$ and $\mu_{eff}(\omega)$, causing it to have a refraction index $\eta_{eff}(\omega) < 0$. Since then, metamaterials have demonstrated the ability to accomplish a variety of features across a wide bandwidth of the EM spectrum, including customized absorption and emission [28], multi-band response [29], or even dynamic performance [30]. Metamaterials may be smoothly incorporated into a wide range of devices thanks to their comprehensive design freedom, including super lenses [31], invisibility cloaks [32], and spatial light modulators [33].

1.2.1 *Metasurfaces: A simplified and effective form of metamaterials*

Planar metamaterials with sub-wavelength thickness are called MS. They might be thought of as the bulk metamaterials' equivalent planar versions that contain a large number of constituent elements in a given direction [34–36]. Instead of the constitutive parameters that are used to define their bulk metamaterial counterparts, MS are described by their sheet impedance and boundary conditions. Furthermore, the metamaterial's complicated 3D shape makes it challenging to produce at the micro- and nanoscale, which limits its usefulness. On the other hand, by designing periodic patterns on planar substrates, MS are simpler to manufacture. The arrangement of the MS might be single [37, 38] or multi-layer [39–41], but the overall thickness must be substantially less than the operating wavelength (λ). Compared to bulk metamaterials, they offer minimal loss in the direction of propagation because of their sub-wavelength thickness. Metasurfaces' interaction with EM waves is powerful enough to give valuable functionality despite their planar shapes.

Significant advancements in theoretical formulation for the study and design of MSs have been made during the past years. An overview of analytical and numerical methods for analyzing 2D and 3D metamaterials is provided in [42]. The analysis of electrically thin metamaterials or MSs has demonstrated that stand-

ard effective medium approximation approaches do not give physically significant parameters. An effective electric and magnetic susceptibility tensor can be used to represent a MS. As an alternative, the authors in [43] model the MS as a periodic arrangement of sub-wavelength metallic/dielectric unit cells acting as artificial atoms (meta-atoms), which can be electrically polarized or magnetized. Additionally, electric current is generated at the surface as a result of the electric and magnetic polarization, and this current may be directly linked to the input electric field using the metasurface's average surface impedance [44]. The equivalent circuit technique, where the MS is represented by a combination of resistance, capacitance, and inductance whose values are derived from its geometrical configuration [45, 46], is a more physically understandable way for the study and design of MSs.

In order to manage the amplitude, phase, and polarization of the reflected and transmitted waves, the underlying unit cell of a MS must be carefully designed. It is possible to construct the optical scatterers' spatial inhomogeneity inside the unit cell in such a way that, following reflection or transmission, the wave front of the interacting wave can be bent in the desired directions. In this context, researchers have shown that reflect-array MSs completely eliminate transmission and specular reflections and display anomalous reflection of impinging waves [47]. Moreover, by optimizing sub-wavelength inhomogeneous optical scatterers, such MSs offer complete phase control for the scattered EM waves.

MS can be created to achieve anomalous refraction of light upon transmission in addition to anomalous reflection. Such MSs must have input impedances that are equalized to the impedance of air/free space, or 377 Ohm, in order to be reflection-free. An anomalous refracting MS with an 86% transmission efficiency in the microwave frequency band is described in [48]. A second MS built on the idea of an optical Nano-circuit and capable of fully controlling the transmitted light's phase is described in [49]. Similar perfect anomalous refraction at terahertz, infrared, and visible light frequencies is described by MS in [50, 51].

1.3 INTELLIGENT REFLECTIVE SURFACES: A BRIEF HISTORY

In 5G and beyond cellular wireless networks, IRS is a revolutionary enabling technology for controlling radio signal propagation. In recent times, IRS has demonstrated a significant capacity for improving the calibre of communication between the access point (AP) and users. IRS is able to reflect the signal from AP to the user as a positive component by appropriately adjusting the phase shifts of the reflecting units (shown in Figure 1.5[1]). The final signal that arrives at the user can be improved by combining this component with the direct transmission component (or the undesired interference from AP can be suppressed). As a consequence, the quality of communication can be increased.

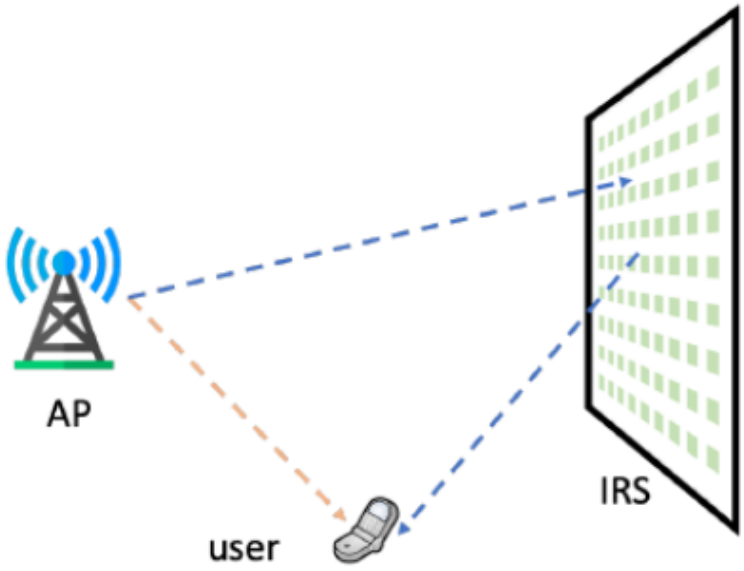

Figure 1.5: IRS deployment for efficient communication between the base station and user.

The IRS's architecture comprises of a smart controller coupled to a thin planar surface with several unit cells. The primary building block of the IRS is the unit cells, whereas the function of the smart controller is to modify how the unit cells interact with the impinging waves. The IRS can be built mostly based on the idea of metamaterials[53]. Because of this, the IRS is also referred to as a MS and is also known as a reconfigurable intelligent surface (RIS), a big intelligent surface, a

1 regenerated from [52]

set of digitally adjustable scatterers, and a surface that can be controlled by software. The unit-cell is referred to as a meta-atom, reflecting element, and scattering element in contrast. A tiny antenna that is coupled to tunable electronics circuits like positive intrinsic negative (PIN) diodes, varactors, or micro-electro-mechanical system (MEMS) switches can serve as a conceptual representation of the unit cell [54]. The configuration of the unit cell's reaction to the incident EM waves is controlled by the adjustable electronic circuits. The IRS's capacity to manipulate EM waves mostly comes from its ability to regulate how much each unit cell reflects the waves that are impinging on it.

Controlling the load impedance linked to the reflecting element is a popular way to change the unit cell's reflection coefficient [55]. For instance, suppose each element has a PIN diode acting as a tunable component. By adjusting the bias voltage of the PIN diode, which will change the load impedance linked to the element between short-circuit and open-circuit, the PIN diode may then be switched between the on and off states. As a result, the reflection coefficient between the on and off states has a 180° phase shift difference. Additionally, each unit cell may be linked to numerous PIN diodes or a varactor for complete phase shift control, allowing for a variety of connected load impedance configurations or a continuous arrangement. A variable resistor load that controls the energy dissipated as part of the incident wave in each unit cell may also be attached to regulate the amplitude of the reflection coefficient [56].

The IRS also has the primary benefit of being a very energy-efficient device because it doesn't need a power amplifier, an RF chain, or complicated signal processing capabilities. Because it doesn't require any power for transmission and instead uses its energy to operate adjustable circuits to alter the impinging wave, the IRS is well-recognized for being almost passive IRS. Active IRS, which may additionally intensify the impinging radio waves, is only conceivable by incorporating inefficient and expensive amplifiers within the unit cells [57].

1.4 AUTHOR'S CONTRIBUTIONS

This thesis focuses on enhancing the radiation characteristics of planar structures using MSs. In particular, this thesis discussed three different structures that include a single port dual band hybrid antenna for next-generation RFID systems, a cross-polarization converter for polarization conversion applications, and an IRS for non-specular reflection.

The study is conducted in three different parts corresponding to three different applications as mentioned above. The first part examines the inclusion of a HIS (a MS) layer that is placed at the bottom side of the dielectric substrate (opposite to the antenna) to improve the radiation performance at UHF and UWB bands separately. The HIS layer consists of two distinct shapes for two different frequency bands. For the UHF band, an inverted L-shaped HIS is designed while for the UWB band, to be coherent with the spiral antenna shape, a circular HIS is utilized. The proposed antenna is then investigated for future applications where conformality is an essential requirement. Therefore, the proposed design is bent in both planes and investigated for its performance at both UHF and UWB bands which is found to be intact as desired. Furthermore, in the proposed design, the feeding point is spiral antenna that has a characteristic impedance of 120Ω while the SMA connector has a characteristic impedance of 50Ω. To cater a reliable measurement, as a final step, a Balanced to unbalanced unit (balun) for smooth impedance transformation is also designed. It is demonstrated that the proposed antenna achieves the following objectives: dual-band operation at UHF and lower European UWB band, shielding from back radiation at both frequency bands and Circular Polarization (CP) at the UWB band simultaneously.

In the second part, a miniaturized MS for CPC applications is examined. The proposed MS has a wide operating bandwidth from 11 - 35GHz. Within this band, the MS is capable of transforming the polarization of the incoming waves upon reflection. A quadrature phase shift is introduced to the incoming wave hence a

horizontally polarized wave is transformed into a vertically polarized wave and vice versa. Furthermore, the polarization conversion stability of the proposed MS is also investigated for oblique incident waves. It is found that the proposed MS has angular stability up to 40° while maintaining a Super Wideband (SWB) response and miniaturized footprints. It is also worth mentioning that a novel mechanism to verify angular stability is also developed in this thesis work. The results of the newly reported method corroborate the analysis method that uses S-parameters to decide the angular stability.

In the final part of this thesis, an IRS is designed for anomalous reflection in a non-specular direction. The proposed IRS consists of unit cells having two metallic patches connected with a capacitor that behaves as a controlling circuit. As an initial step, an IRS with a fixed direction of reflection (though non-specular but not reconfigurable) is thoroughly analyzed. The direction of non-specular reflection depends on the size of the cluster of unit cells (referred to as supercell in this thesis) and power coupling to a non-specular direction can be tuned using a lumped capacitor. Later, the locally tuned MS (as each unit cell has its own control mechanism) is converted into a globally tuned IRS (where all unit cells have a common control mechanism). To accomplish this, an artificially designed ferroelectric material Zirconium-doped Hafnium Oxide (HfZrO) is utilised whose dielectric properties vary widely with the applied bias. The lumped capacitor, being an inherent component responsible for the tuning of the response, is also replaced by a distributed IDC.

1.5 ORGANIZATION OF THE THESIS

This thesis is organized as below: **Chapter 2** describes the design and performance of the proposed uni-port dual band hybrid antenna for UHF and UWB RFID applications. This chapter also discusses the design of HIS that helps in achieving CP at the UWB band as well as shielding back radiation at both UHF and UWB bands.

Following this, the next application as a cross-polarization converter is discussed in **Chapter 3**. The proposed design is compact in size and possesses a super wide-band response. The proposed MS is further analyzed for its angular stability under the oblique incident case. **Chapter 4** deals with the design of a globally controlled IRS. The proposed IRS is capable of propagating incoming wave towards a non-specular direction based on the user's need. **Chapter 5** provides a short summary of the overall proposed work and concludes this thesis.

2

PLANAR STRUCTURE-1 : UNI-PORT DUAL-BAND MICROSTRIP ANTENNA

This chapter is based on the following publications:

- ***S. Agarwal***, *D. Chadzichristodoulou, A. Quddious, D. Masotti, S. Nikolaou and A. Costanzo, "HIS Design for an Environment-Robust UHF/UWB Antenna with 3D-Printed Inclusions," 2021 51st European Microwave Conference (EuMC), 2022, pp. 817-820, doi: 10.23919/EuMC50147.2022.9783614.*

- ***S. Agarwal***, *D. Masotti, S. Nikolaou, and A. Costanzo, "Conformal Design of a High-Performance Antenna for Energy-Autonomous UWB Communication," Sensors, vol. 21, no. 17, p. 5939, Sep. 2021, doi: 10.3390/s21175939.*

- ***S. Agarwal***, *D. Chadzichristodoulou, A. Quddious, D. Masotti, S. Nikolaou and A. Costanzo, "A Hybrid RFID/Localization Antenna with HIS and 3D-Printed Inclusions," 2021 IEEE International Symposium on Antennas and Propagation and USNC-URSI Radio Science Meeting (APS/URSI), 2021, pp. 875-876, doi: 10.1109/APS/URSI47566.2021.9704750.*

- ***S. Agarwal***, *A. Costanzo and D. Masotti, "Dual-Purpose Metasurface for Background Insensitive UWB Tag : (Invited Paper)," 2021 15th European Conference on Antennas and Propagation (EuCAP), 2021, pp. 1-5, doi: 10.23919/EuCAP51087.2021.9411341.*

2.1 INTRODUCTION

The rapid proliferation of so-called "smart dust" in the context of the Internet of Things, which refers to small devices dispersed in the environment that are able to carry out fundamental sensing operations, has led to an increased interest in power-free pervasive computing [58]. In certain circumstances, this operation can be carried out by utilising resonant coupling or inductive coupling [6, 59]. However, you can only use this method in situations in which there is relatively close proximity between the charger and the device and in which the majority of the objects involved are stationary. When these limitations need to be removed, that is, when moving objects that are far from the Radio Frequency (RF) source need to be charged (such as in logistic applications), Energy Harvesting (EH) and/or Wireless Power Transfer (WPT) are the candidate technologies that will make this feasible. This is because they can extend the lifetime of the battery or completely avoid the use of the battery altogether. If the identification of the device is of the utmost significance, one way to accomplish this would be to use technology that combines Ultra High Frequency (UHF), with RFID. Moreover, if we refer to applications in which moving objects are involved, operations such as identification and localization both become, at the same time, of strategic importance: in most cases, these functionalities are offered by separate wireless systems. This chapter aims to present an advanced antenna solution that will serve as the front end of a future generation of RFID tags. This solution will successfully combine all of the aforementioned requirements, allowing it to function as an independent position sensor. In order to accomplish these goals, the UHF band is utilised, with the dual objectives of producing a tag that is compatible with the generations of RFID tags that are currently in use and producing a tag that is energy independent through the utilisation of dedicated RF energy showers [60]. In terms of localization and communication operations, the antenna makes use of the well-established Impulse Radio-Ultra Wideband (IR-UWB) technology. This technology has already

demonstrated its effectiveness, particularly in an indoor environment, by achieving sub-meter localization precision through the signal back-scattered by the tag itself despite the ultra-low power signals that are involved [60–62].

The authors of [63] designed a hybrid Ultra Wideband (UWB)-UHF antenna that has a good matching response but has unsatisfactory performance from the Axial Ratio (AR) perspective. The proposed solution draws its inspiration from this work. In addition, the development of an antenna that is insensitive to the material that is serving as the background is of the utmost significance in the case of the anticipated application as a tag for the next generation. This results in an antenna that can be used wherever it is necessary without affecting the response in any way, regardless of the material that is in the background. Because of these reasons, the current work begins with the preliminary findings of [64], in which a first idea to shield the antenna was proposed, but only for the UWB band. An extended shielding effect for both bands is presented in this chapter, along with a prototype realisation of the effect. To the best of the author's knowledge, this is the first High Impedance Surface (HIS) that is able to guarantee both the Circular Polarization (CP) and low back radiation in a frequency band (in the literature, only one of the two results is achieved at a time), while also functioning as a shield at a frequency that is completely unrelated to the first frequency (the UHF, in this case). The layout is then modified slightly due to the conformal realisation of the antenna. This additional step is taken to test the versatility of the proposed architecture for future applications that require a deformation to function properly. A planar Balanced to unbalanced unit (balun) is also added as a final step in order to ensure a safe transition from the balanced antenna to the future diplexing network in microstrip technology. This network is going to be in charge of the management of simultaneous UWB communication and UHF Energy Harvesting (EH).

2.2 HYBRID ANTENNA WITH CIRCULAR POLARIZATION IN UWB RANGE

A schematic diagram of the hybrid antenna, which is referred to as *"first antenna"* in the chapter, along with all of the parameters, is shown in Figure 2.1, and Table 2.1 lists the optimized values for the design parameters. As a first step, a paper substrate ($L_{S1} \times W_{S1}$) that has a dielectric constant (ε_{rel}) of 2.85, a thickness (h) of 5mm, and loss tangent (tanδ) of 0.053 is used. It is possible to deduce from Fig. 2.1 that the structure being discussed is made up of two distinct antennas. An archimedean spiral antenna that transmits and receives signals in the lower European UWB frequency range (3.1 - 4.8 GHz) and is used for the purposes of communication and localization. In the meantime, the long dipole antenna, which is made up of the meandered traces of the spiral in addition to the straight extensions (dark orange coloured blocks in Fig. 2.1(a)), is operating at the UHF band (868MHz) and is also considered to be a receiving antenna to receive the ElectroMagnetic (EM) energy that is capable of guaranteeing its energy autonomy.

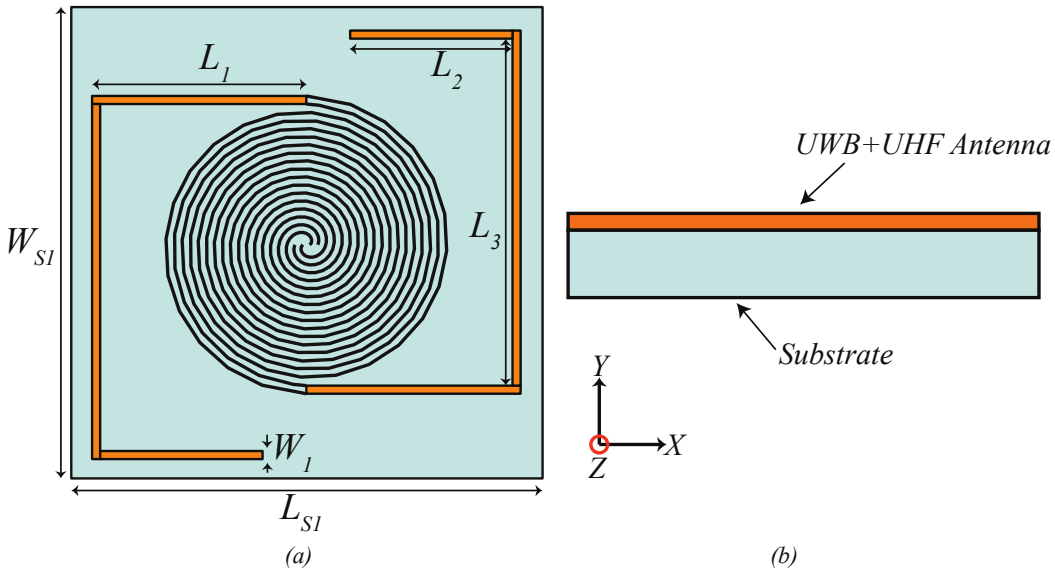

Figure 2.1: First antenna (a) Front view (b) side view.

For the UWB antenna, the design rules adhere to the standard guidelines for auto-complementary antennas presented in [65]. This means that the width of the copper traces and the empty traces are identical. In order to achieve an AR that

Table 2.1: Parameters of the first antenna.

Parameter	Value (mm)
L_{s1}	130.20
W_{s1}	130.20
L_1	63.60
W_1	2.40
L_2	48.20
L_3	103.00

is lower than that found in [63], both the width and the number of turns have been fine-tuned. There was a discernible increase not only in the length of the spiral but also in its turns. In terms of the UHF antenna, the physical length of the antenna is determined by the combination of its straight lines and spiral loops. In terms of radiation, the close loops cancel each other out, and the far-field is found to be horizontally polarized. In addition, the length of the dipole is longer than the conventional half-wavelength; more specifically, it is 2.5 times as long as the standard half-wavelength, as can be seen from the multiple resonances in the reflection coefficient.

Figure 2.2 displays the simulated results of the first antenna. Figure 2.2(a,b) make it abundantly clear that the antenna is operating flawlessly within the UHF and UWB frequency bands. As a non-linear rectifier is foreseen as a load in the UHF frequency range for EH reasons, the dipole antenna reflection coefficient is measured with respect to a 12 Ω resistance, which represents a quite typical value of the rectifier's input resistance at low impinging power levels [64]. This is done while considering that $|S_{11}|$ at the antenna balanced port is less than -10 dB. On the other hand, the UWB bandwidth is calculated relative to the standard impedance of an Archimedean spiral, which is 120 Ω [65].

The number of turns (N) and the width (w) of the traces are the two most important critical parameters in a spiral antenna [66]. These two parameters contribute the most in achieving the desired value of CP. In light of this, a comprehensive parametric study was conducted on the design presented in [63], and Figure 2.2(c)

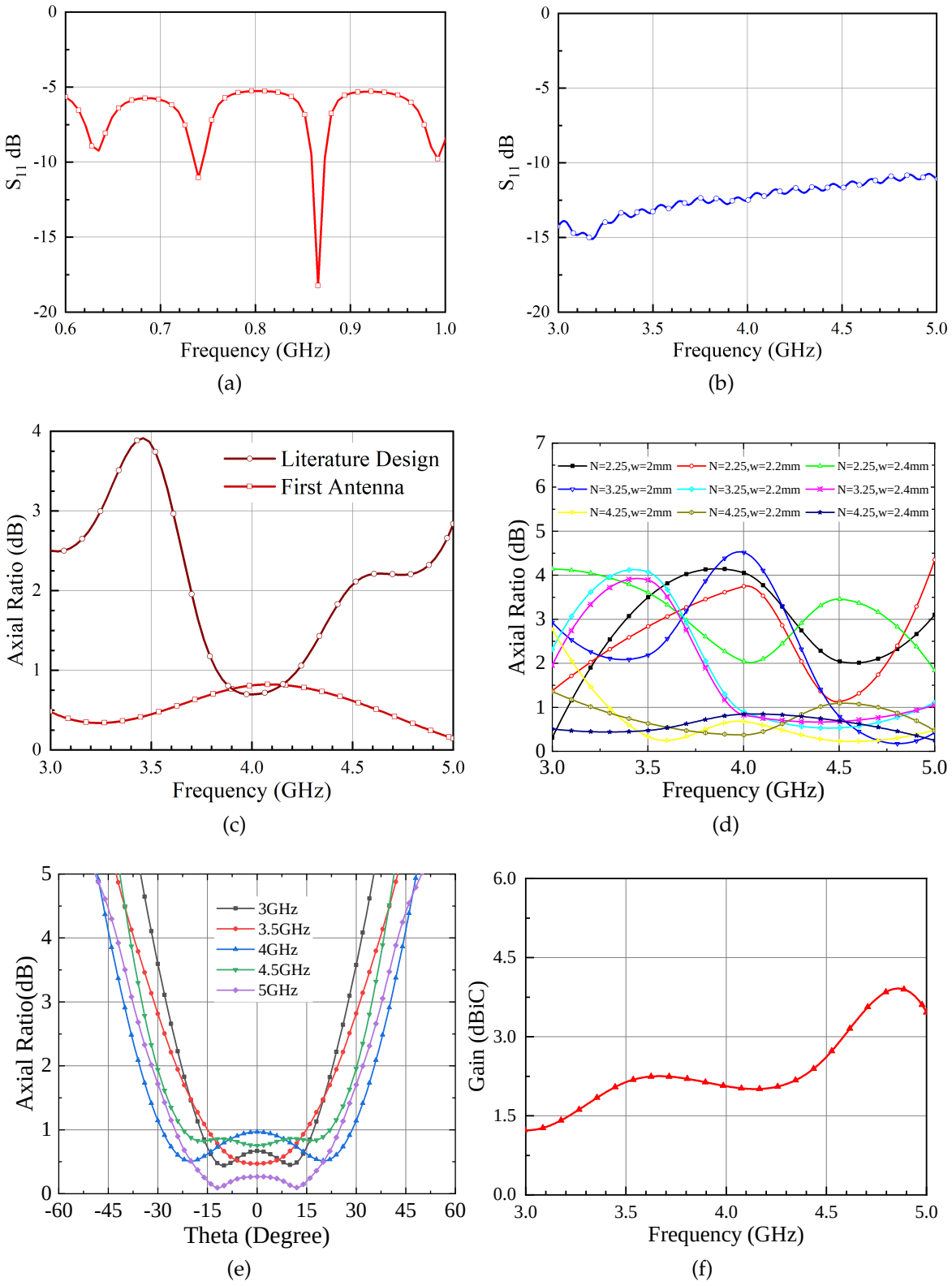

Figure 2.2: Simulated results of the first antenna (a) Reflection coefficient for UHF band (normalized to 12 Ω) (b) Reflection coefficient for UWB band (normalized to 120 Ω) (c) Axial Ratio (d) parametric analysis of AR (e) AR v/s θ (f) Gain.

displays the obtained optimized response. In addition, it can be seen from Fig. 2.2(d) that an AR below 1 dB within the UWB range is achieved for N = 4.25 and w = 2.4 mm. This is the case for the configuration in which the antenna footprint is the largest. Since the objective of this antenna involves achieving CP within the UWB range only, the AR in the UHF band is not optimized, but the radiated field at this frequency results linear polarization (AR=40 dB)". In terms of the length of the dipole, it is obviously capable of being tuned in accordance with the desired matching condition. In this particular application, the antenna length corresponds to the resonant condition (that is, the imaginary part of the antenna input port impedance is equal to zero). However, of course, a proper tuning of the length can be utilised in order to fulfil the conjugate matching condition with the RFID chip impedance [63]. In addition, the variation of AR with respect to theta(θ) is displayed in Figure 2.2(e) so that one can get a better understanding of how it varies across the beamwidth. The gain performance of the first antenna can be seen in Figure 2.2(f), which improves slightly with increase in frequency.

Following this, an analysis of the antenna's radiation performance is carried out, as can be seen in Figure 2.3. In addition to frequencies in the UWB range (3–5 GHz), the performance is demonstrated at the UHF frequency of 868 MHz as well. The findings reveal without a doubt that the antenna emits radiation in the direction of $\theta = 0^\circ$ and $\theta = 180^\circ$. This is because the structure is not supported by the ground plane, and hence the antenna performance is also affected by the platform where it is affixed. In order to ensure platform independency, an effective and wideband shielding solution must be introduced in such a way that the radiation is maximum in the broadside direction.

The use of a HIS is discussed next, which helps in mitigating back radiation.

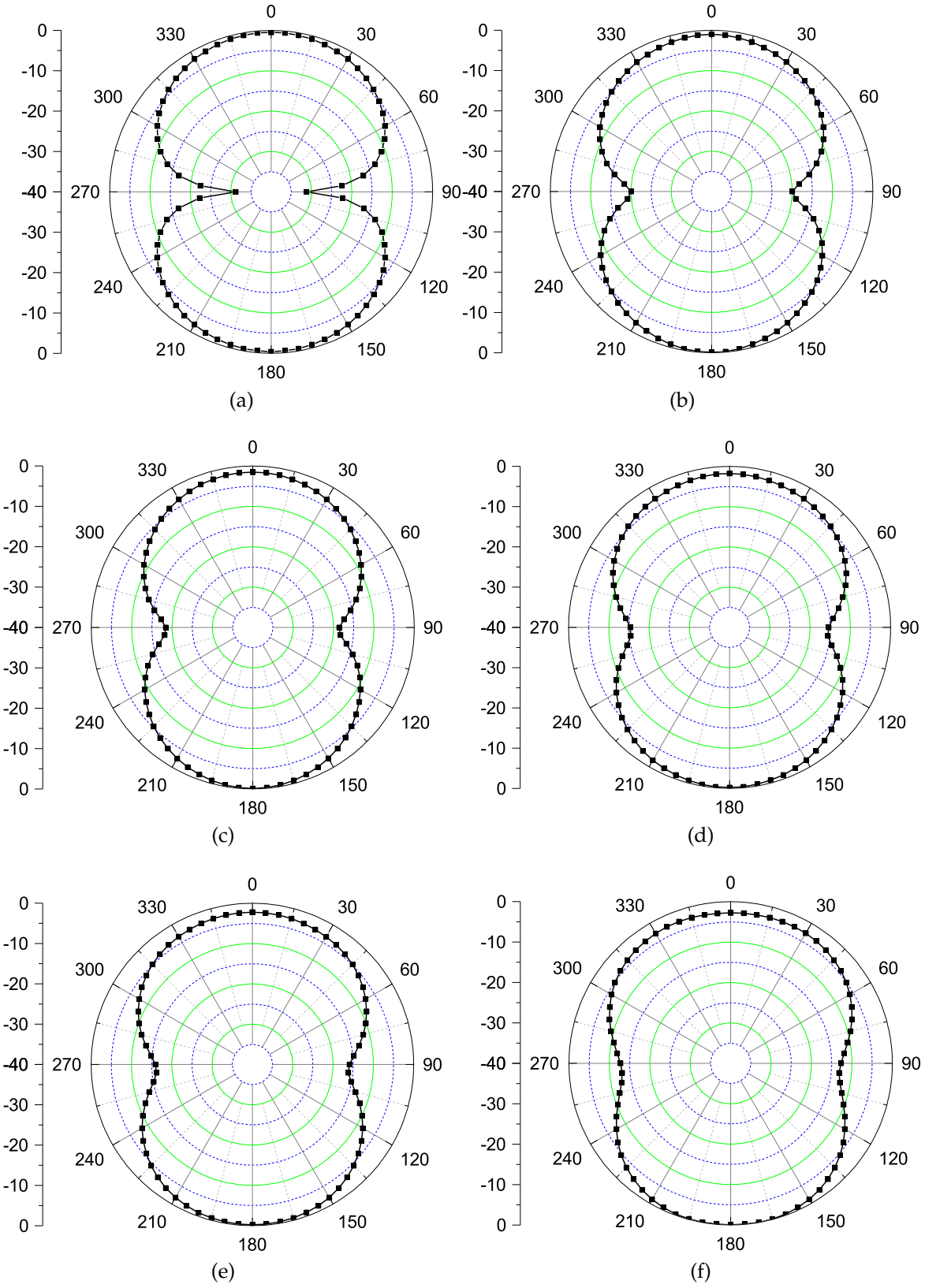

Figure 2.3: Simulated radiation characteristics (xz plane) of first antenna at (c) 3.5GHz (d) 4GHz (e) 4.5GHz (f) 5GHz.

2.3 HIGH IMPEDANCE SURFACES: A PLAUSIBLE SOLUTION FOR BACK SHIELDING

HISs, are typically made up of a combination of metallic patches placed on top of a grounded dielectric substrate [67]. The HIS can be used as a Perfect Magnetic Conductor (PMC). In contrast to Perfect Electric Conductor (PEC), a PMC does not cause any phase shift in the reflected waves; as a result, the waves that are incident and reflected continue to be coherent. The HIS structure for a UWB spiral antenna designed on a 1 mm thick paper substrate is already been reported in [64]. The HIS is re-optimized on the Rogers/RT duroid 6002 substrate (ε_{rel}=2.94, $\tan\delta$=0.0012, h=0.508mm) because the fabrication process makes it difficult to achieve the precision of 1mm paper thickness. In addition to this, a novel inverted-L-shaped HIS has also been designed on the same substrate in order to reduce the back radiation caused by a UHF dipole. When it comes to the simulation setup, a fundamental distinction can be seen between rectangular and circular HIS. The simulation can be carried out in a rectangular HIS by utilizing only a unit cell, whereas in a circular HIS, a unit ring comprising a certain number of metallic patches needs to be considered [68]. Figure 2.4 displays the entire HIS layer as well as the circular HIS. Table 2.2 provides a summary of the parameters that were optimized for the HIS layer. In this table, g_r and g_w refer to the distance between the rings and the gap between the patches within a ring, respectively. The response to the circular HIS can be found by following the instructions mentioned in [68].

To achieve a wideband performance, more HIS rings can be employed; however, it is necessary that all the rings share a common phase response over the relevant frequency range [69]. Four such rings are investigated in this work (shown in Figure 2.4(a)), with their phase responses tailored specifically to the UWB frequency band. Figure 2.5 depicts the optimized phase response of the four unit rings, which exhibits linear phase variation within the operating frequency range; then, in the subsequent simulations, the HIS is taken into account as a whole (no more as a

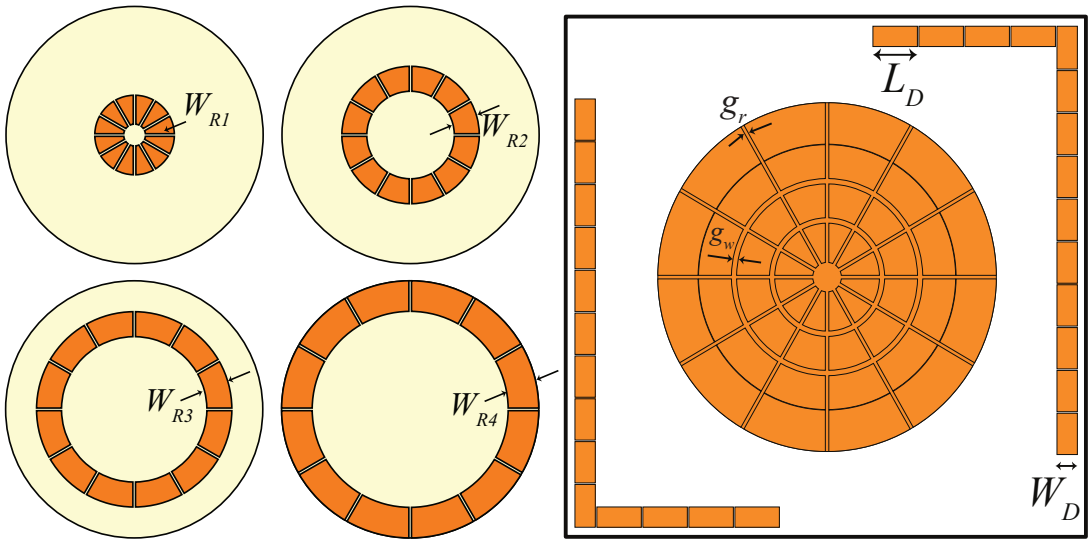

(a) (b)

Figure 2.4: (a) Four HIS rings (innermost to outermost) and (b) complete HIS layer.

Table 2.2: Optimized parameters of HIS layer.

Parameter	**Value (mm)**
W_{R1}	10.10
W_{R2}	9.49
W_{R3}	9.42
W_{R4}	9.49
g_r	0.6
g_w	0.4
W_D	5.5
L_D	9.8

combination of four separated unit rings). By introducing the same number of patches along the X- and Y-direction, symmetry is preserved, which aids in the enhancement of CP in the UWB frequency range. By primarily adjusting the width (W_{R1} – W_{R4}) in Figure 2.4, the surface phase response can be tuned within the desired frequency band. As the widths of the patches increase, the phase response shown in Figure 2.5 shifts towards lower frequency ranges (left side). In a similar way, an increase in the gap value between the patches causes a shift in the response slightly to the right (higher frequency ranges). Additionally, the importance of cell numbers to achieve linear phase response cannot be overstated. This is because

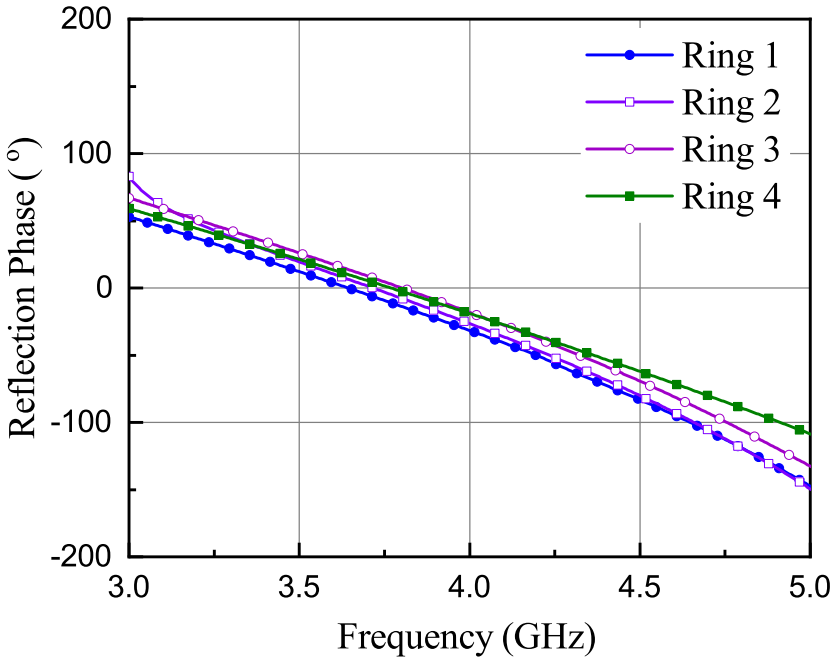

Figure 2.5: Phase response of four circular HIS rings.

the curvature effect is reduced as more patches are added to the ring. All these constraints help in tuning the desired HIS response within the frequency band of interest.

Figure 2.4(b) shows that a conventional inverted-L shaped HIS is designed [70], optimized, and placed behind the UHF band dipole antenna to act as a shield due to the linearly (in this case, horizontally) polarized field radiated by the antenna. In the following part of this chapter (Figure 2.9(a)), it is demonstrated that L-shaped HIS does not completely cancel back radiation in the UHF range, but it does improve efficiency from 57% to 76% in the UHF range. It follows that HIS plays a crucial role in keeping the stack up low profile while still providing adequate performance for both the spiral and dipole antennas.

2.4 HIGH GAIN HYBRID ANTENNA EMBRACING 3D PRINTING TECHNOLOGY

In order to avoid the complications associated with fabricating on a thick paper substrate, the first antenna has also been redesigned on a 1.5 mm thick Rogers/RO 6002 substrate. Substrate properties parameter changes necessitate re-tuning of the

antenna to achieve the desired performance. The front view of the final antenna layout is shown in Fig. 2.6(a) with all the parameters (designated as *second antenna* hereafter), while a perspective view with transparent antenna substrate is shown in Fig. 2.6(b) for better visualization of the complete structure. Table 2.3 compiles summaries of the antenna and HIS parameters and their corresponding values.

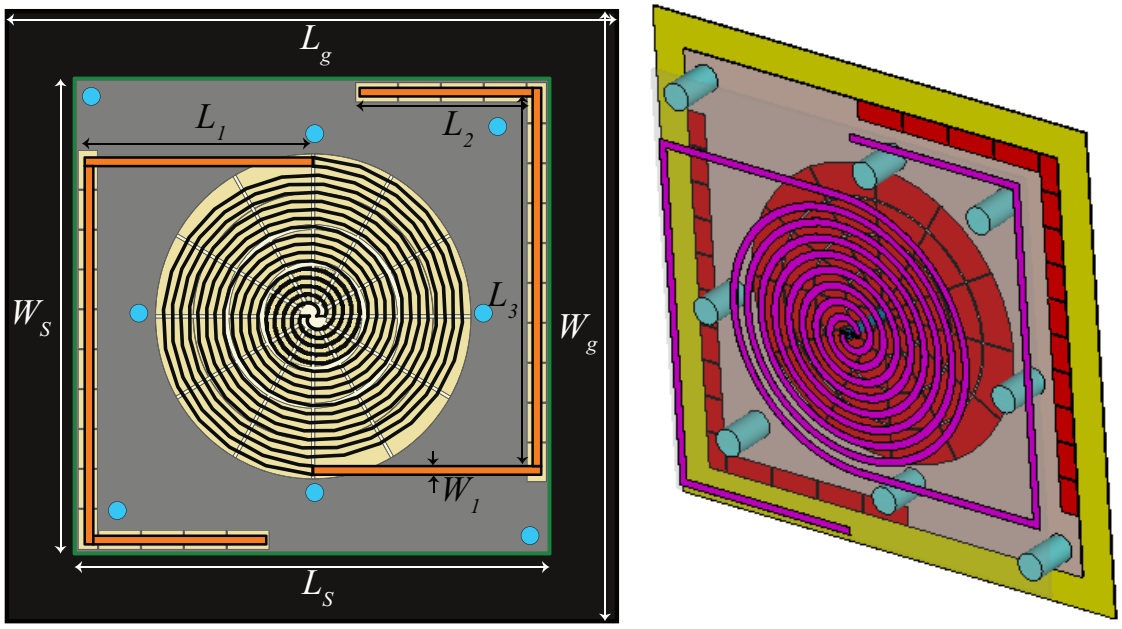

(a) (b)

Figure 2.6: High gain hybrid antenna design: (a) top view; (b) perspective view (antenna substrate is made transparent for better visualization). (second antenna).

Table 2.3: Optimized parameters of the second antenna and the HIS.

Parameter	Value (mm)	Parameter	Value (mm)
W_S	120	L_1	58.4
W_{R1}	10.10	g_r	0.6
W_g	140	L_2	52.2
W_{R2}	9.49	g_w	0.4
L_S	120	L_3	94.6
W_{R3}	9.42	W_D	5.5
L_g	140	W_1	2.2
W_{R4}	9.49	L_D	9.8

Fig. 2.7(b) shows the antenna in cross-section. The antenna has six layers, as shown in the figure: the hybrid antenna, Rogers RO/6002 substrate for antenna,

air gap, HIS layer, Rogers RO/6002 substrate for HIS, and ground plane. An air gap of 13 mm is introduced between the antenna and the HIS layer to improve the antenna's gain performance, which was diminished by the lower substrate thickness. In addition, eight 3-D printed posts are used to hold up the uppermost layer. Supporting structures (light blue cylinders) are printed using 3D technology and utilise PLA filament with ε_{rel}=3.5 and $\tan\delta$=0.04.

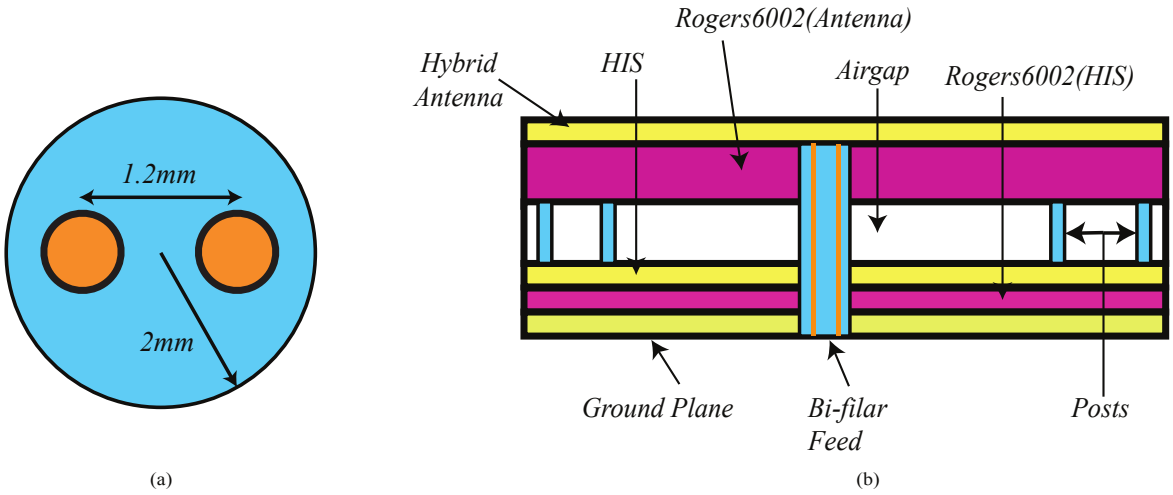

Figure 2.7: Proposed novel bi-filar feeding (a) top view (b) cross-section of complete antenna structure (not to scale)

In addition, this work proposes a novel feeding mechanism to excite the hybrid antenna. In Fig. 2.7(a) the feeding structure is shown. It consists of two conductors inserted in a PLA cylinder. Since the proposed antenna has its excitation port at the center of the spiral antenna, it is important that the characteristics impedance of the bi-filar lines should be 120 Ω which is guaranteed when the gap between the conductors is 1.2mm. The PLA cylinder not only provides insulation between the conductors but also acts as an additional support for the antenna layer.

The second antenna simulation results are displayed in Figure 2.8. The UHF antenna bandwidth, shown in Figure 2.8(a), is determined in a manner analogous to that used for the earlier design, assuming the resistive part of a voltage-doubler rectifier for low incident power, which in this case is 12Ω. UWB bandwidth, on the other hand, is roughly estimated with a standard spiral antenna impedance

[65] as depicted in Figure 2.8(b). The results demonstrate that both antennas are operating efficiently within their designated frequency range.

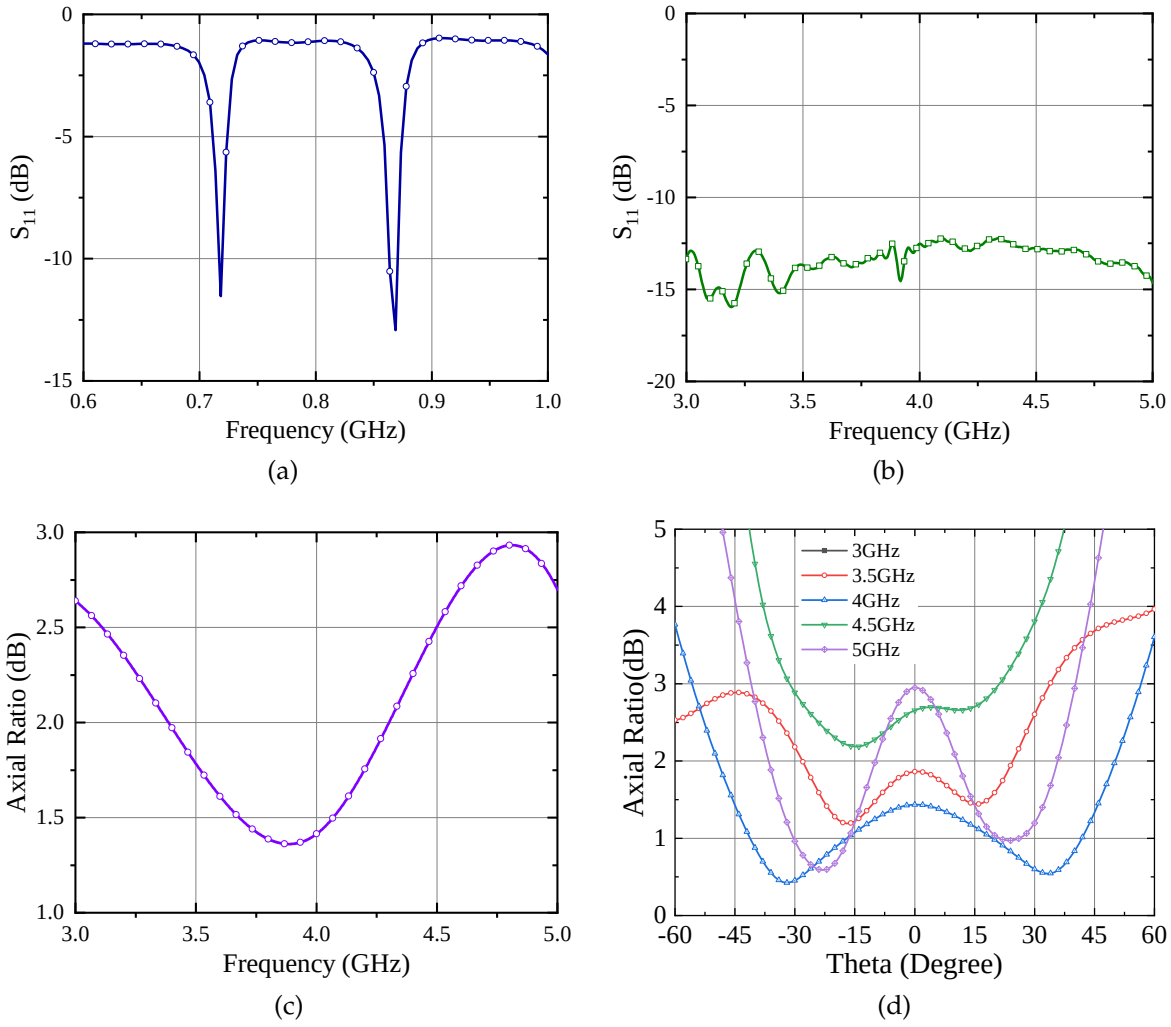

Figure 2.8: Simulated responses of second antenna (a) S_{11} for UHF band (normalized to 12 Ω) (b) S_{11} for UWB band (normalized to 120 Ω) (c) AR v/s Freq (d) AR v/s θ.

Moving on to the next step, the results of second antenna for the AR and gain are displayed in Figure 2.8(c–e), respectively. One can see from Figure 2.8(c,d) that the AR of the antenna is less than 3 dB, which ensures CP throughout the entire UWB range. In addition, the antenna's gain performance is enhanced when configured in a suspended fashion. The gain for the UWB range is ≥8 dBi, while for the UHF band it is ∼4.8 dBi.

It is anticipated that the radiation characteristics of the second antenna should get enhanced due to the fact that the HIS is now functioning as a PMC.

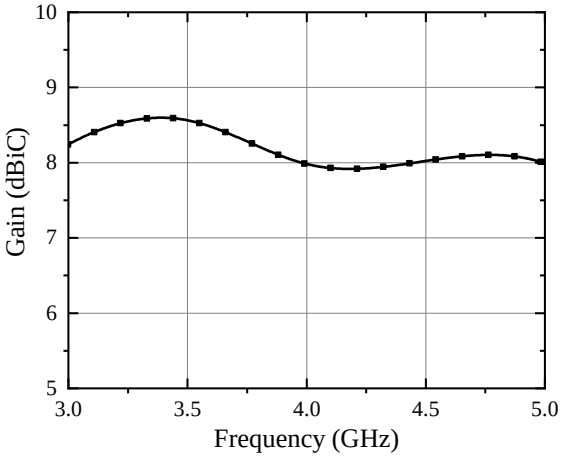

(e)

Figure 2.8: Simulated responses of second antenna (e) Gain.

Figure 2.9 illustrates the simulated radiation patterns of the antenna's E-field at six different frequencies ranging from UHF to UWB. As can be seen from the figures, the incorporation of HIS improves the back radiation by more than 20 dB for the UWB band and 10 dB for the UHF band.

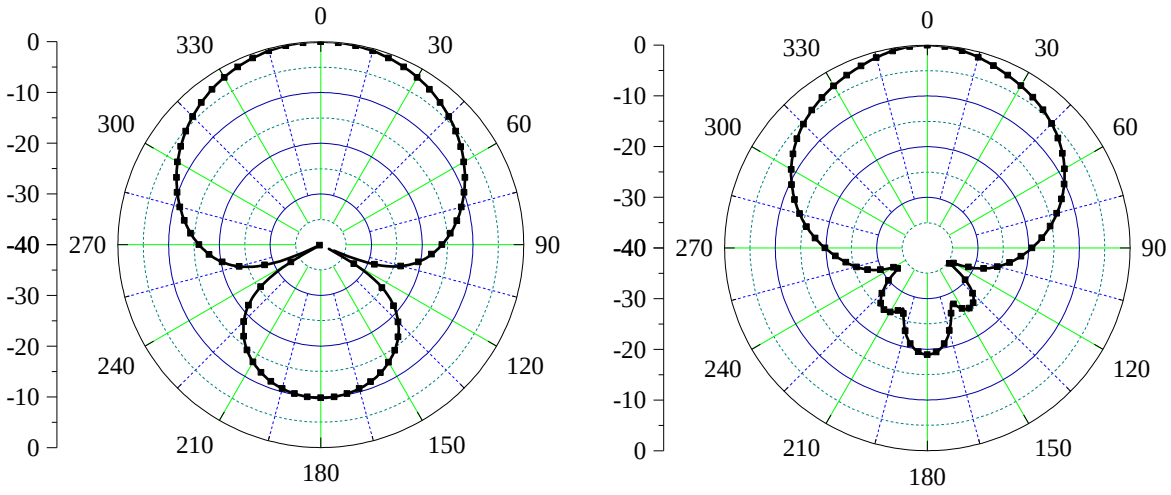

(a) (b)

Figure 2.9: Simulated radiation patterns of second antenna (xz plane) at (a) 868MHz (b) 3GHz

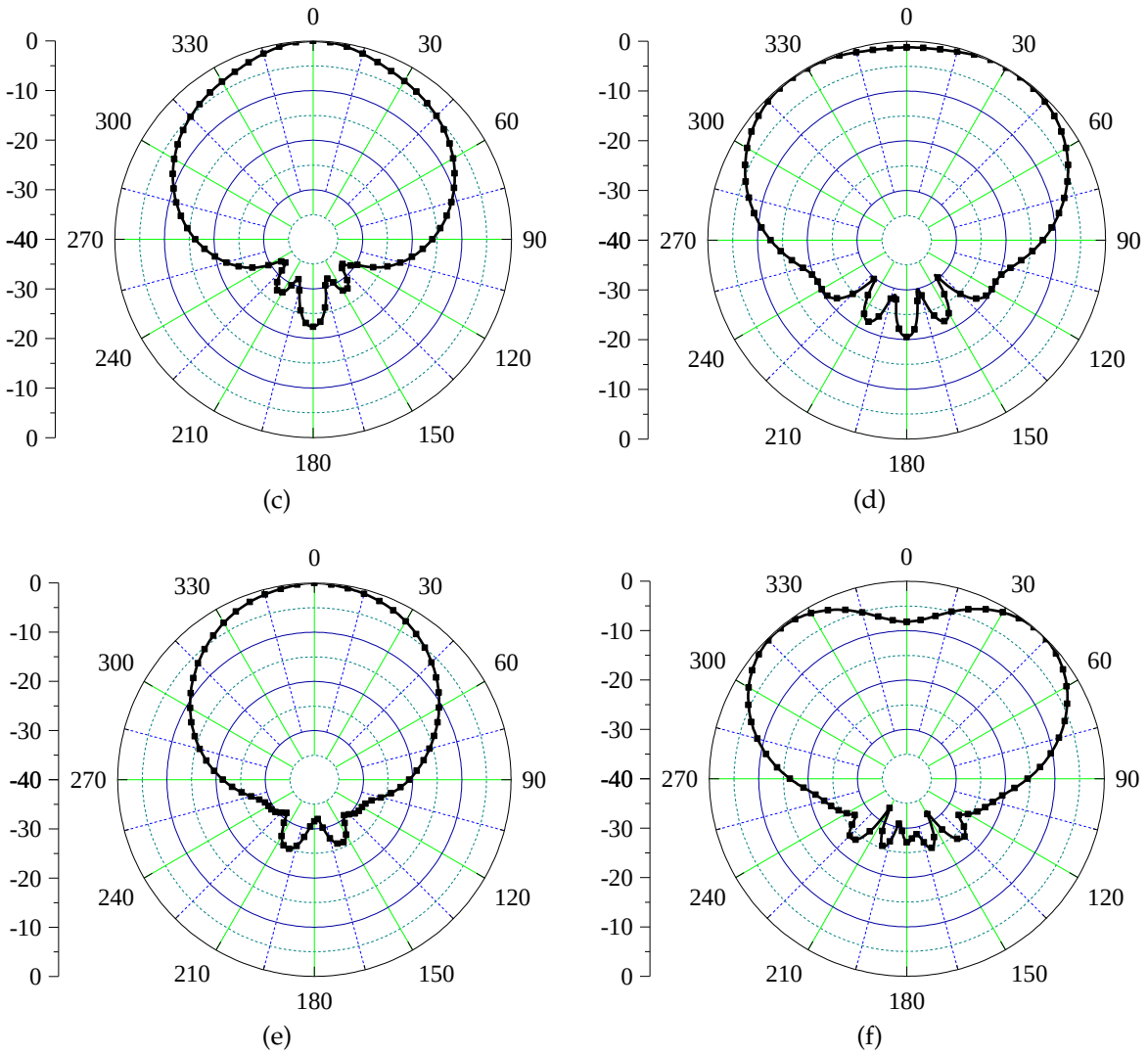

Figure 2.9: Simulated radiation patterns of second antenna (xz plane) at (c) 3.5GHz (d) 4GHz (e) 4.5GHz (f) 5GHz.

2.4.1 *Experimental validation*

In order to demonstrate that the design is reliable, a prototype of the second antenna has been fabricated (Fig. 2.10), and the characteristics of the reflection coefficient have been measured using the Agilent Power Network Analyzer (PNA) E8368B.

Due to the hindrance of direct measurement using balanced bi-filar lines by directly attaching an instrument, one of the two conductors of the bi-filar line is connected to a 120 Ω microstrip line (Fig. 2.10(c)) while other conductor is groun-

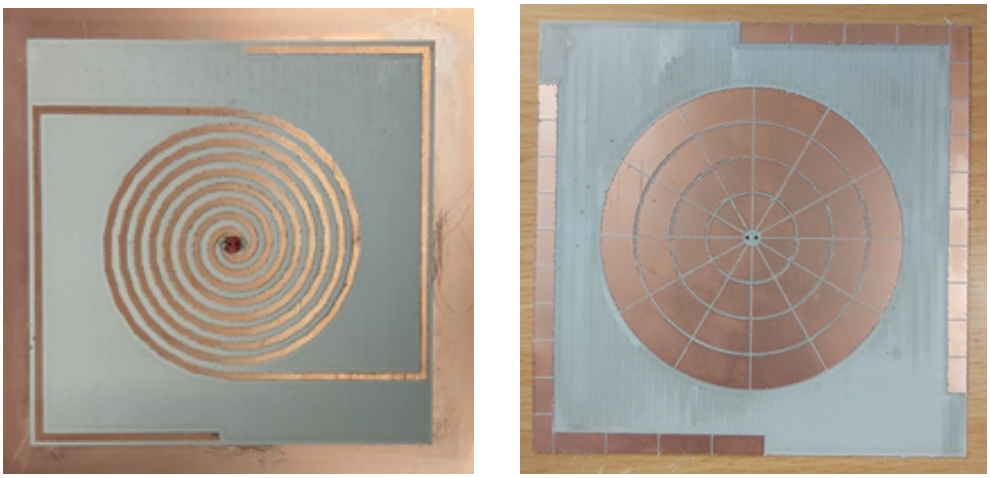

(a) (b)

(c)

Figure 2.10: Fabricated prototype (a) Hybrid antenna layer (b) HIS layer (c) Ground plane FR-4 layer with feed line

ded. The 120 Ω feed line is excited by a SMA connector, and a FR4 substrate (ε_{rel}=4.4, h=1.6mm, tan δ=0.025) layer is added behind the ground plane to support the microstrip line and the connector. This sudden change was accomplished for the sole purpose of obtaining a first measurement that can prove the correctness of the complex design. The development of a planar balun that is capable of transforming the impedance level from 120 Ω to 50 Ω is, of course, the solution that needs to be pursued in order to correctly tackle this issue. This additional step has been completed later and is described in Section **??**. Figure 2.11 demonstrates both the simulated and experimental results that are normalized to 120 Ω.

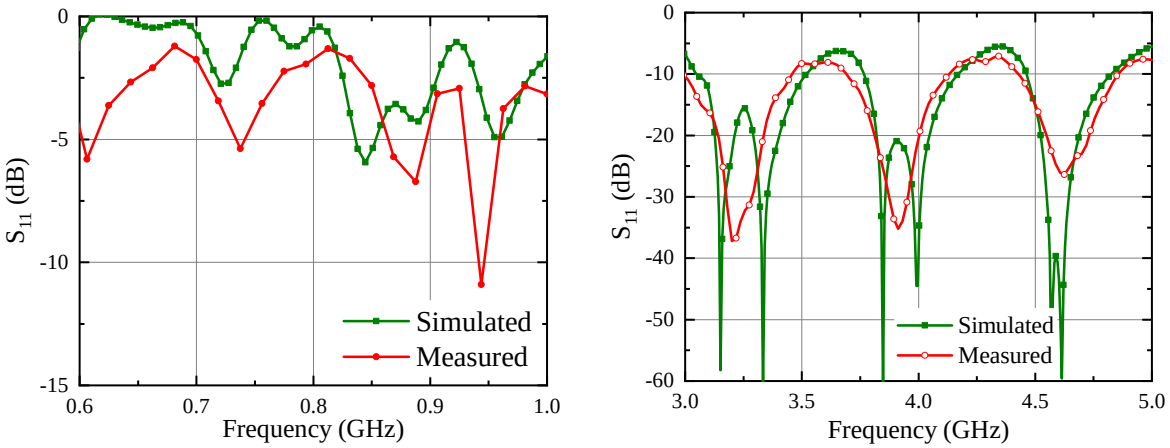

Figure 2.11: Simulated and measured reflection coefficient of the hybrid UWB antenna (a) S_{11} for UHF band (normalized to 120Ω) (b) S_{11} for UWB band (normalized to 120Ω)

Because of the unconventional transition from bi-filar to microstrip line that was used in the measurement, it can be seen in the figure that the results agree with one another quite well. However, it should be noted that these results are distinct from those that were presented earlier for the same reason.

2.5 DUAL PLANE HYBRID CONFORMAL ANTENNA WITH SUSPENDED HIS

A dual-plane conformal design of the second antenna is discussed in this section. This investigation is motivated by the fact that a future realisation of the antenna (with the diplexer, the EH circuitry, and the UWB backscatter modulator) is foreseen with flexible materials. This will allow the antenna to be easily located in a broad range of placements and for a diverse collection of applications where localization/tracking and energy autonomy are required. A wireless charging system could be installed on the fuselage of a drone so that it can be powered up without disrupting the flight. The parameters of this antenna are identical to the second antenna design reported previously in this chapter. Figure 2.12 demonstrates the simplified representation of the dual-plane conformal antenna. The bending is carried out around a hemisphere with a radius of 100mm.

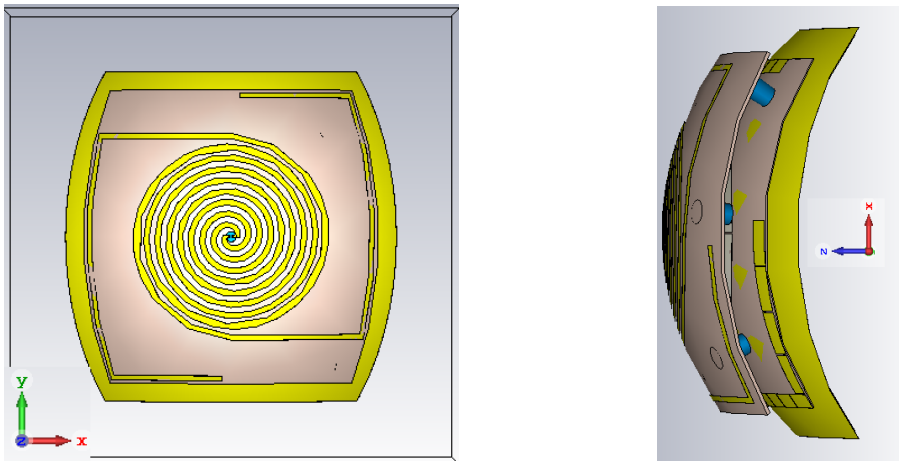

(a) (b)

Figure 2.12: Dual plane conformal antenna with suspended HIS (a) Front view (b) side view

During the process of bending the stacked antenna, it was noticed that the inverted-L-shaped HIS was no longer located behind the UHF antenna as was anticipated. This is an important point to take into consideration here. Because of this, the effect of the HIS at the UHF frequency was rendered entirely ineffective. In order to find a solution to this issue, the size of the HIS layer was increased by a factor of 1.05, because of which the antenna yields a total size of 126×126 mm^2.

The EM simulation of the antenna is performed in CST MWS and simulation results are displayed in Figure 2.13(a-f). The findings make it clear that the antenna is capable of functioning in both the UHF band and the UWB band.

Despite the significant bending, the AR performance of the antenna has not been compromised in any way, and it continues to provide CP throughout the entire UWB range. Figure 2.13(d) illustrates the gain performance. When compared to the second antenna design, the bending causes a reduction in the gain of the conformal antenna; however, this gain is still sufficient for the intended purposes. As was discussed earlier, when an antenna is bent, the UHF antenna becomes more susceptible to damage because it is located closer to the edges of the substrate. As a result, there is a noticeable decrease in the gain at the UHF band, which is 1 dBi at 868 MHz.

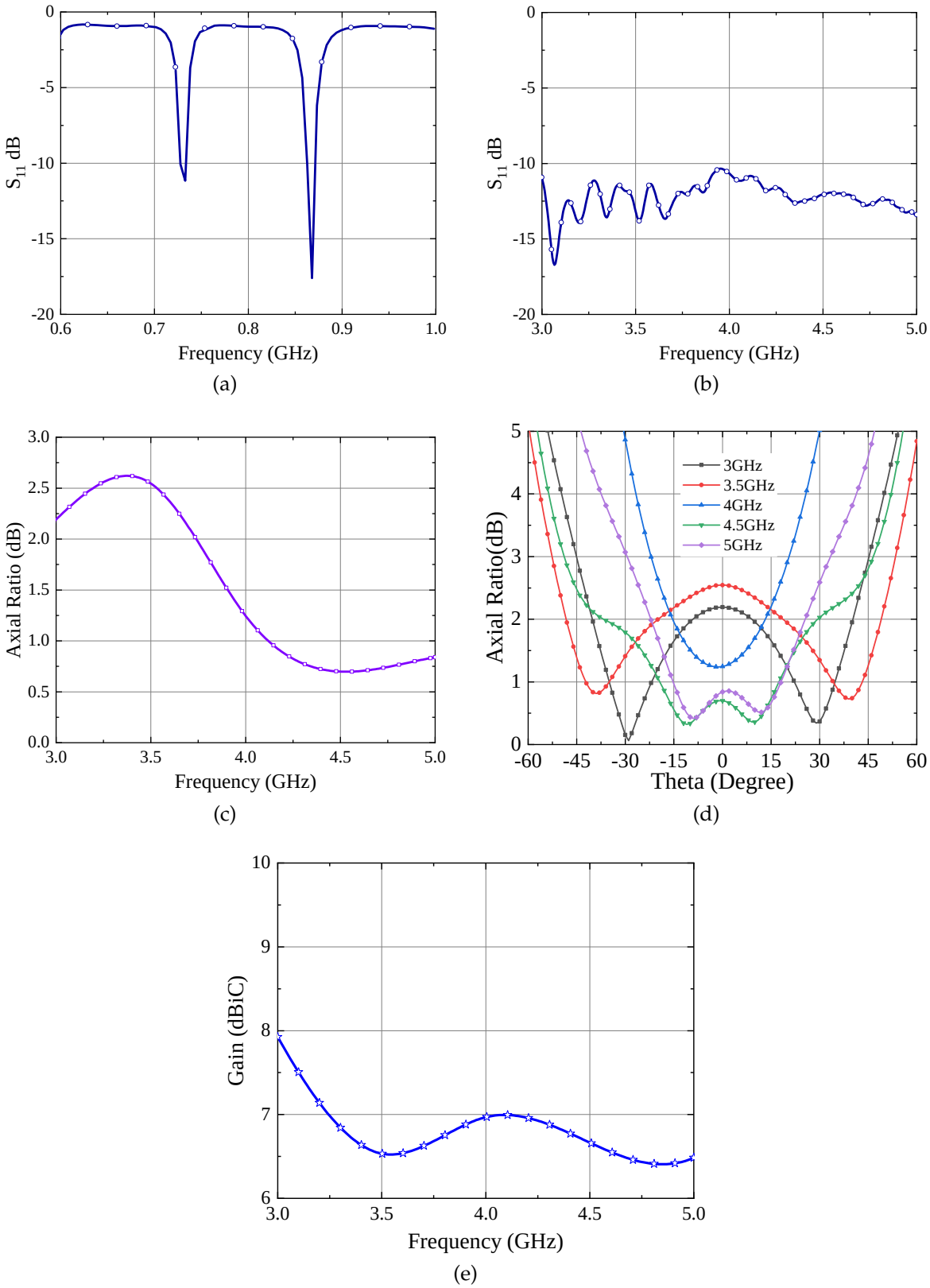

Figure 2.13: Simulated responses of dual plane conformal antenna (a) S_{11} for UHF band (normalized to 12 Ω) (b) S_{11} for UWB band (normalized to 120 Ω) (c) AR v/s Freq (d) AR v/s θ (e) Gain.

Moving on, the simulated radiation characteristics of the conformal antenna at UHF and within the UWB frequency range are shown in Fig. 2.14.

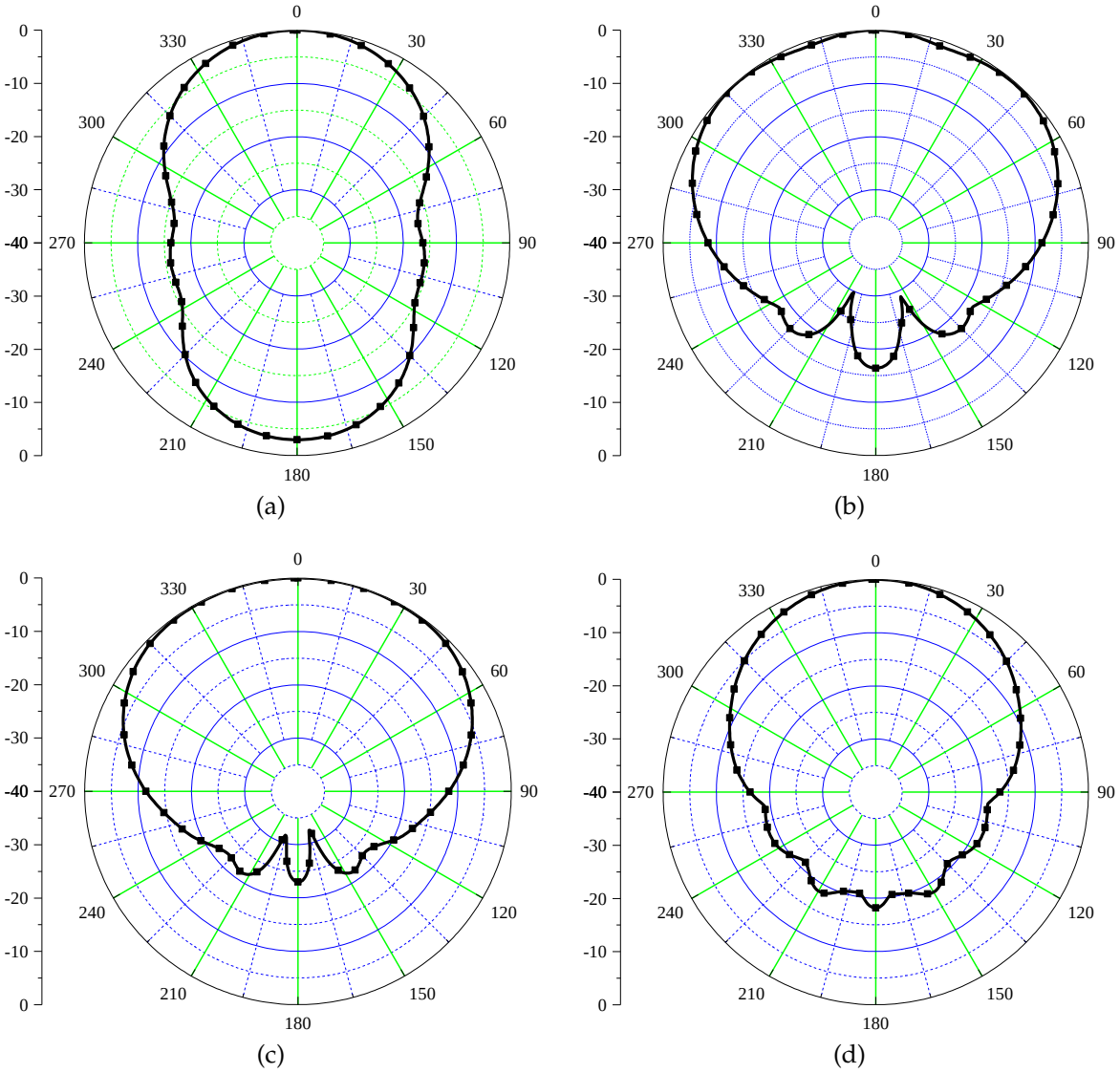

Figure 2.14: Simulated radiation patterns of dual plane conformal antenna (xz plane) at (a) 868MHz (b) 3GHz (c) 3.5GHz (d) 4GHz (e) 4.5GHz (f) 5GHz.

The UHF frequency band is where the majority of the back radiation is observed (with a Front-to-back ratio (FBR) of 3 dB). This is because when the antenna is bent in both planes, the UHF antenna, which is already located at the edge of the substrate, becomes more susceptible to back radiation and causes the antenna to flex. It is important to note that desired performance was accomplished by slightly increasing the HIS, as was described earlier. This was the reason for the improvement.

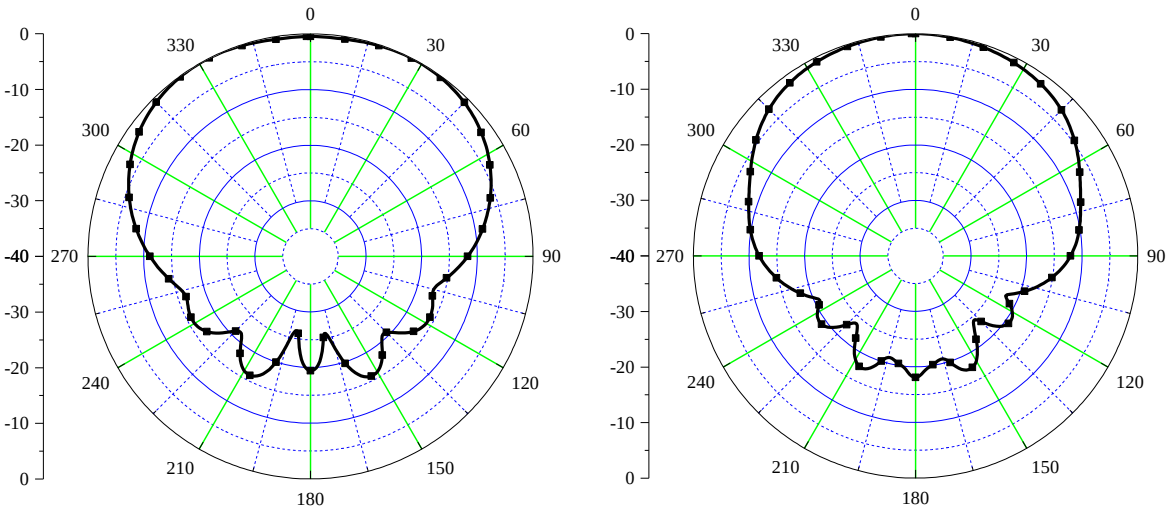

Figure 2.14: Simulated radiation patterns of dual plane conformal antenna (xz plane) at (c) 3.5GHz (d) 4GHz (e) 4.5GHz (f) 5GHz.

When looking at Fig. 2.14(b-f), we can see that the back radiation is less than -15dB for entire UWB frequency range.

2.6 UNI PORT DUAL BAND HYBRID ANTENNA: COMPLETE SOLUTION

A Balanced to unbalanced unit (balun) is a strategic part that needs to be developed for a direct connection of the dual-mode antenna to a 50 Ω instrumentation. This was previously discussed, and it is important to note that in order to feed the spiral antenna using the bi-filar line feeding structure reported in this chapter, a balun is required. As can be seen in Figure 2.15, one such balun is designed in accordance with the rules presented in [71] on a Rogers/RO 6002 substrate that has a thickness of 0.508 mm (ε_{rel} = 2.94, tan δ = 0.0012). It is made up of an un-grounded planar 120 Ω bi-filar line, as a prosecution of the vertical one whose top side is the port 1, followed by an open stub that is partially grounded and a microstrip line that is grounded, as well as a microstrip impedance step in order to reach the 50 Ω at the output port (port 2). In Table 2.4, the parameters of the balun are summarised.

The simulation results of the balun are illustrated in Figure 2.16. Within the UWB band, the transmission parameter (S_{21}) varies between -1.2dB and -1.5dB as

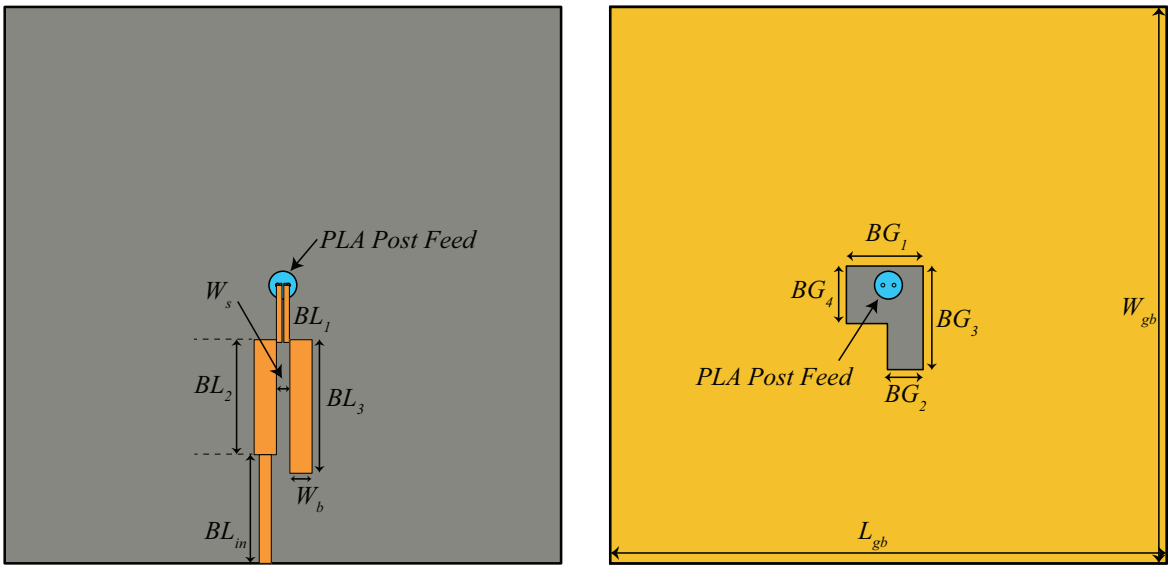

(a) (b)

Figure 2.15: Balanced to Unbalanced (Balun) design (a) Top view (b) ground plane

Table 2.4: Optimized dimensions of the proposed balun.

Parameter	Value (mm)	Parameter	Value (mm)
BL_1	5	BG_1	20
BL_{in}	8	L_{gb}	60
BL_2	12.4	BG_2	9.3
W_b	2.4	W_{gb}	60
BL_3	14.4	BG_3	27
BG_4	15	W_s	1.4

shown in Fig. 2.16(a). At 868 MHz, performance is marginally subpar but is still considered satisfactory. Naturally, the design of the balun is the result of a careful negotiation between the performance in the two different frequency ranges that are very far apart. After that, this balun is inserted behind the second antenna design.

Since the footprints of the second antenna are larger than the balun, the length of the 50-Ω feed line length (BL_{in}) is increased to 52.6mm. Figure 2.17 depicts the simulation results of the complete antenna structure.

It can be concluded from the figures that the antenna is operating as expected. However, the AR performance of the antenna suffers slightly and decreases at the

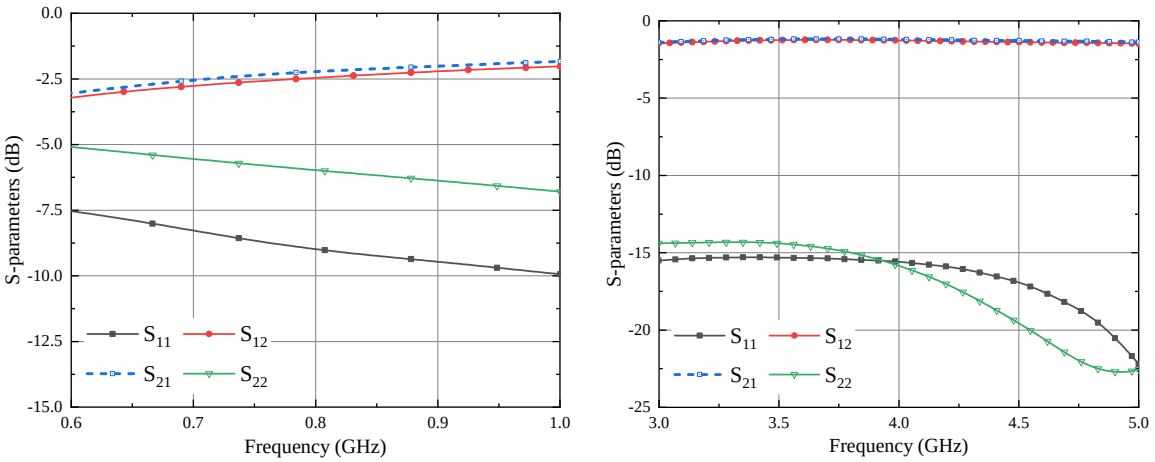

Figure 2.16: Simulated S-parameter results of planar balun at (a) UHF band (b) UWB band

beginning of the UWB band. However, within most of the UWB range the AR performance remains intact. The antenna has a good gain, with a peak value of 8.6 dBi at 4.7 GHz, an average gain of more than 7 dBi in the entire UWB band, and a gain of 3 dBi at the UHF frequency.

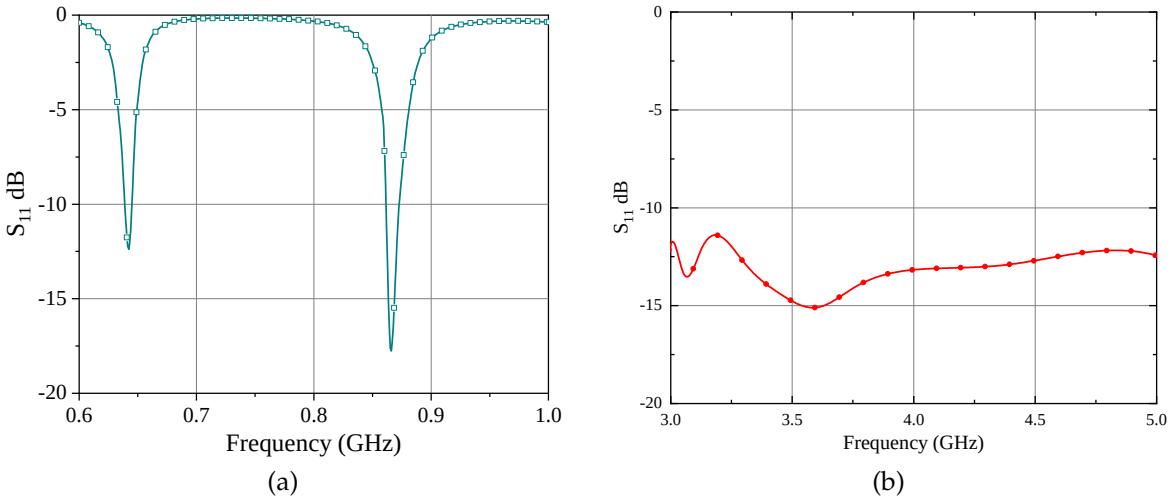

Figure 2.17: Simulated responses of dual-band hybrid antenna (a) S_{11} for UHF band (normalized to 12 Ω) (b) S_{11} for UWB band (normalized to 120 Ω)

The radiation characteristics of the antenna are then computed at each of the six frequencies shown in Figure 2.19. Following the installation of the balun, it is possible to draw the conclusion that the performance of the antenna has not been

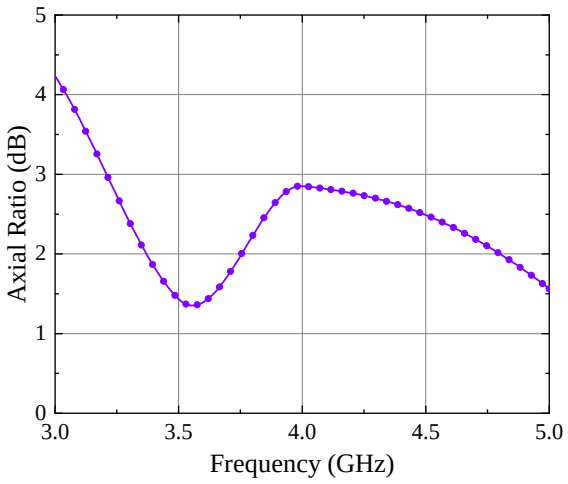

(c)

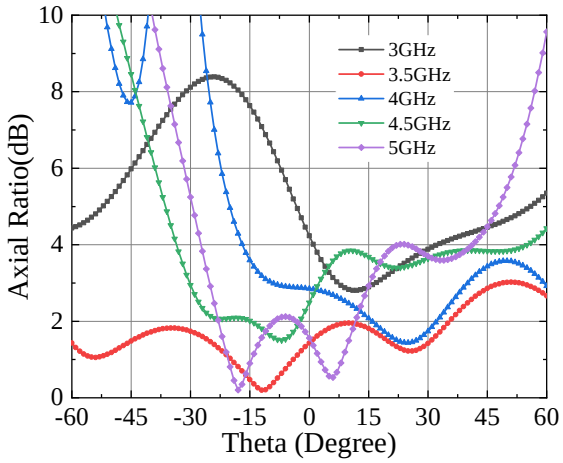

(d)

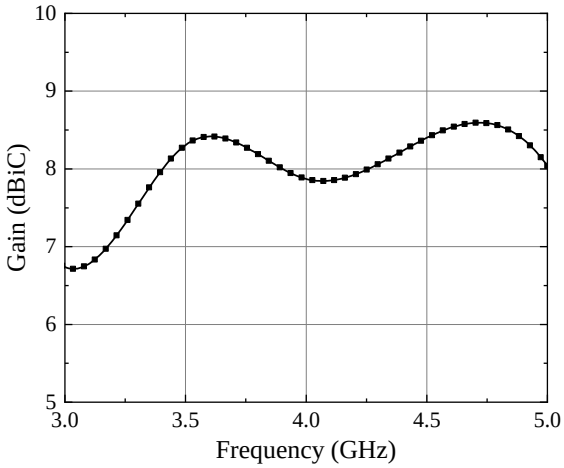

(e)

Figure 2.17: Simulated responses of dual-band hybrid antenna (c) AR v/s Freq (d) AR v/s θ (e) Gain.

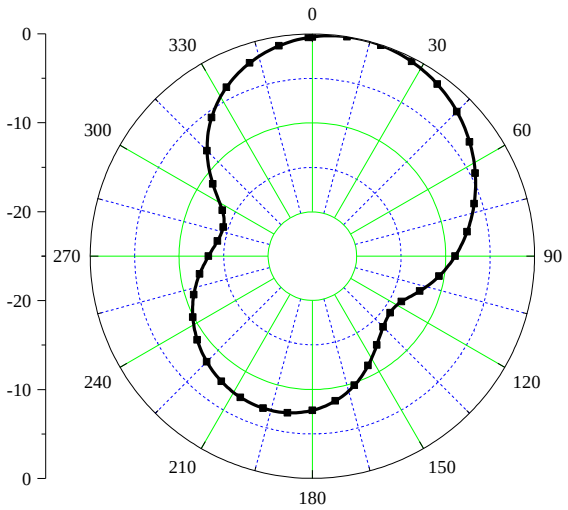

(a)

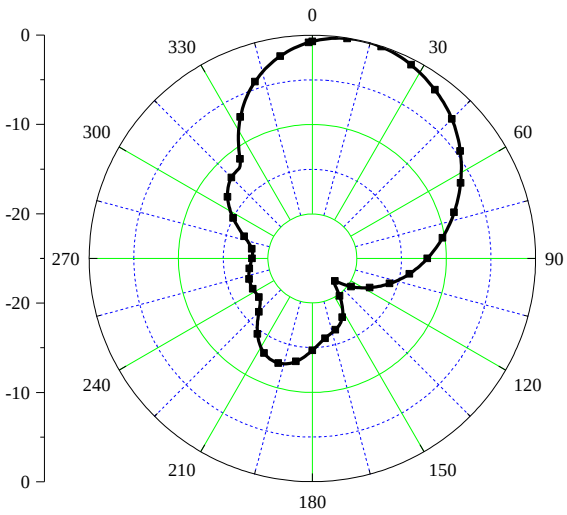

(b)

Figure 2.18: Simulated radiation patterns of the conformal antenna (xz plane) at (a) 868MHz (b) 3GHz

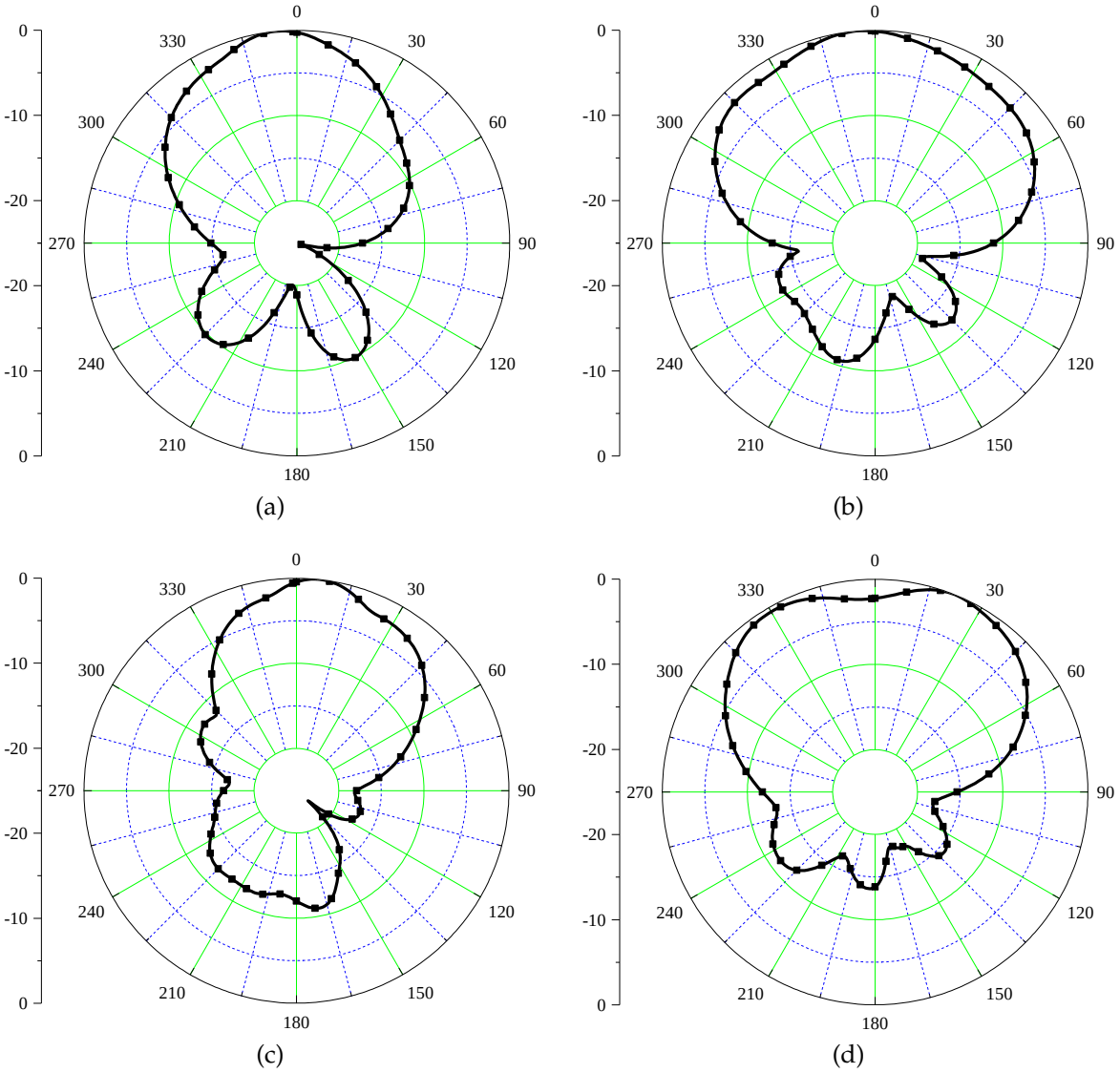

Figure 2.19: Simulated radiation patterns of the conformal antenna (xz plane) at (c) 3.5GHz (d) 4GHz (e) 4.5GHz (f) 5GHz

compromised, and it is able to reduce the amount of back radiation at both the UHF and the UWB bands. Due to asymmetric etching from the ground plane, the HIS response is affected which in turn slanted the radiation patterns slightly.

The results of a study that compared the proposed antenna with previously published research are summarised in table 2.5. It is clear from the table that the primary benefits of the proposed antenna are its single-port nature, which guarantees an easier feeding network, a more compact layout, the CP within the UWB band, and its ability to operate independently of any platform because of HIS. In addition, the robustness with regard to dual-plane bending, which is something

Table 2.5: Comparison of the proposed antenna with the existing literature.

Ref.	Separate Antennas	No. of Antenna Ports	Circular Polarization (in UWB Band)	Insensitive to Background Material	Robustness wrt Deformation	Energy Harvesting Arrangement
[59]	yes	2	no	no	N.A.	no
[63]	no	1	yes	no	N.A.	yes
[72]	no	2	no	no	N.A.	yes
[73]	yes	2	no	yes	N.A.	no
[74]	yes	2	no	no	N.A.	no
[75]	yes	2	yes	yes	N.A.	no
[76]	yes	2	yes	yes	N.A.	no
This work	no	1	yes	yes	yes	yes

that is not always studied in the literature, is very encouraging. Because of this, the proposed antenna proves its candidacy for the next-generation RFID systems.

2.7 SUMMARY

A uni-port dual-band circularly polarized antenna has been discussed in this chapter. The presented antenna serves dual purposes in two different bands, i.e. energy autonomy in the UHF band and communication/localization in the UWB band. The CP in the UWB band is controlled simultaneously with the back-radiation mechanism at widely separated frequencies thanks to a suspended high-impedance surface designed and deployed behind the antenna for the first time. The proposed multi-layer architecture's mechanical stability and novel bi-filar feeding strategy owe a great deal to the use of 3D-printed posts. Despite the bidirectional bending, the structure reveals itself to be quite robust to mechanical changes, so a conformal design of the proposed hybrid antenna is studied for future technological systems like drones that would require wireless charging while in flight. With the addition of a diplexing network, a harvesting section, and a back-scatter modulator, the proposed radiating system will be ready to take on a pivotal role in the next generation of RFID tags.

3

PLANAR STRUCTURE-2 : CROSS POLARIZATION CONVERTER FOR SWB APPLICATIONS

This chapter is based on the following publication:

- ***S. Agarwal**, G. Murtaza, A. Costanzo and D. Masotti, "A Super Wideband Angularly Stable Metasurface for Cross Polarization Conversion Applications," 2021 IEEE MTT-S International Microwave and RF Conference (IMARC), 2021, pp. 1-4, doi: 10.1109/IMaRC49196.2021.9714591.*

3.1 INTRODUCTION

This chapter focuses on the characteristics of radiation exhibited by periodic structures. Planar Metasurface (MS) based on metamaterials have been extensively researched in recent years due to their wide range of applications in various fields such as planar optics, anomalous refraction, angular momentum of light, optical vortex generation, and polarization conversion. The polarization of ElectroMagnetic (EM) waves is a crucial factor in the operation of certain devices, and transforming one type of polarization into another can be both advantageous and difficult. Traditional methods such as the Faraday effect and the optical activity of crystals have limitations, making metasurfaces a potential solution.

Different MS-based structures have been proposed in the literature to monitor and control the polarization of EM waves over a large bandwidth. For example, a dual-band anisotropic MS with cross-polarization conversion is presented in [77], which operates in the 5–9.7 GHz and 11.2–15 GHz frequency bands. In [78], an elliptical disk-ring-shaped reflective cross-polarization converter with dual-band operation (6.99–9.18 GHz and 11.66–20.40 GHz) and high conversion efficiency is reported. An angularly stable MS with high conversion efficiency is proposed in [79], which operates from 17.46 GHz to 29.85 GHz and has a Polarization Conversion Ratio (PCR) value of more than 98% throughout the operating range.

An asymmetric V-shaped resonator-based Ultra Wideband (UWB) MS for polarization conversion is presented in [80], which uses symmetric and asymmetric modes of excitation to generate multiple resonances using resonators of different sizes. The authors also designed a double-headed arrow-shaped MS for polarization conversion in [81]. In [82], a double-slit Split Ring Resonator (SRR)-based MS for cross-polarization and operating in the UWB frequency band is proposed. The same authors also reported another MS serving dual purposes of CPC and linear to circular polarization (LP-to-CP) conversion in X-band in [83]. A circular SRR with a ring printed-based MS for CPC applications is presented in [84]. Another dual-band anisotropic MS for CPC applications is reported in [85]. In [86], a MS composed of double-slit circular SRR with a Swiss-cross in the middle is reported for CPC applications.

The proposed MSs in the above-mentioned literature either have larger footprints or narrow bandwidth. Therefore, a small, flat, ultra wideband MS that is also stable in response to variations in incident wave angle is the need of the hour.

One such MS fulfilling the above requirements is discussed in this chapter. The design has miniaturized footprints, covering a wide frequency range (11–35GHz) with a high degree of angular stability w.r.t. oblique incident up to 40°. In Section 3.2, the conceptualization of the MS and corresponding results are discussed.

Next, the angular stability of the proposed MS is shown in Section 3.3. In the last, conclusions are drawn in Section 3.4.

3.2 CROSS POLARIZATION CONVERTER FOR SWB APPLICATIONS

In order to design the MS for Cross Polarization Conversion (CPC) applications having sufficiently large bandwidth, a Rogers/RT 5880 substrate with the dielectric properties (ε_{rel}=2.2, $\tan\delta$ =0.0009) and height h=2.4mm is utilised. The final layout of the proposed MS is shown in Fig. 3.1. Parameter values that have been optimised through iterative analysis are shown in Table 3.1.

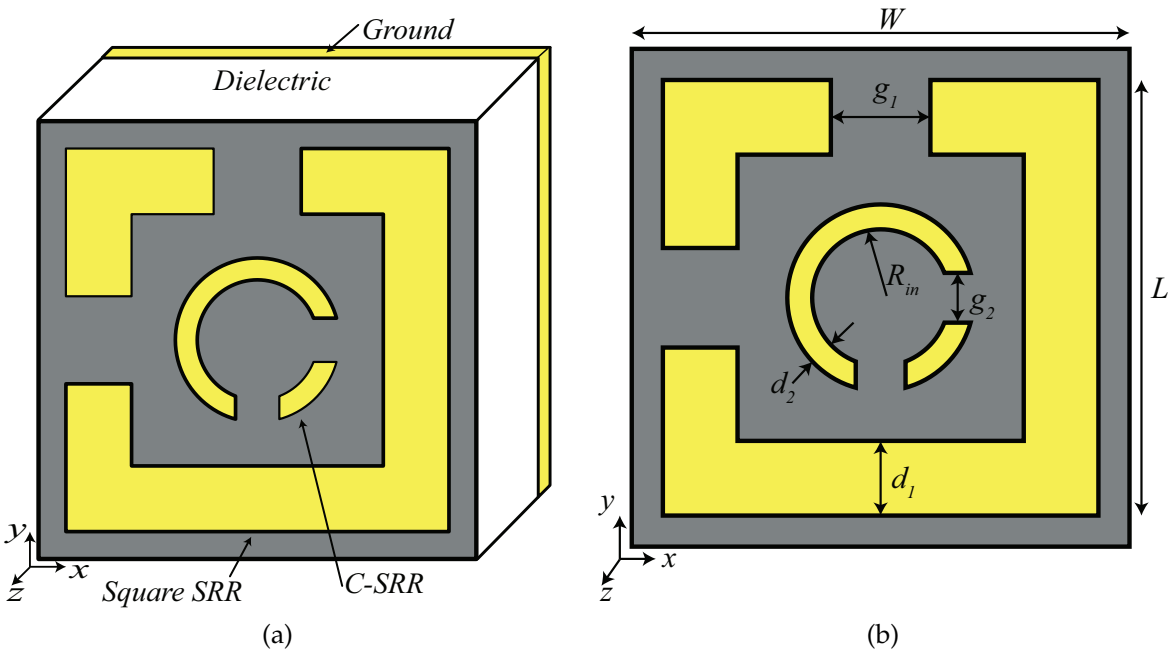

Figure 3.1: Final layout of the proposed MS (a) perspective View (b) Top view.

Table 3.1: Optimized parameters of proposed MS for CPC applications.

Parameter	Value (mm)	Parameter	Value (mm)
W	4	d_2	0.2
L	3.5	g_1	0.8
d_1	0.6	g_2	0.4
R_{in}	0.55	–	–

In order to design the proposed MS, a square substrate with dimensions of $W \times W\ mm^2$ is used, as can be seen in Figure 3.1. A circular SRR and a square SRR are designed on the top of the substrate, while the opposite side of the substrate has a complete ground plane. The SRRs and the ground plane are both designed with 35 microns thick copper. An electric current flows only along the side of an SRR where the applied electric field is parallel to the no-spilt-bearing side. Instead, electric current flows along both the spilt bearing side and the perpendicular (the side with no split) side when an electric field is applied along a spilt bearing side.

Applying this knowledge, two gaps are created in the adjacent sides of the square SRR—one gap for each linearly polarized impinging field. Plasmon resonances at higher frequencies can be generated with the help of the inner circular SRR, which helps to achieve a Super Wideband (SWB) response. Fig. 3.2 (a,b) demonstrates the simulation results in terms of the co-polarized and the cross-polarized ratios as defined in the next parts of this chapter. It's possible that the reader will have a question about the absence of a cross-polarized component after looking at the figures. As can be observed that the electric field is along the split bearing side of the SRR, it excites the current in both sides (with and without split) of the SRR. Nevertheless, the excited currents on the other side (the side with no split) are flowing in the opposite direction from one another; as a result, their effects cancel each other out [87].

CST Microwave Studio was used to design and simulate the proposed MS. Within the simulation setup, a Floquet port is utilised in the +Z direction, while periodic boundary conditions are utilised for the X- and Y-axes. An X-polarized wave, when falls on the MS, generates a co-polarized component known as R_{xx} as well as a cross-polarized component (R_{yx}) upon reflection.

Mathematically, R_{xx} and R_{yx} can be defined as Eq. (3.1):

$$R_{xx} = \frac{|E_{rx}|}{|E_{ix}|}, \qquad R_{yx} = \frac{|E_{ry}|}{|E_{ix}|} \tag{3.1}$$

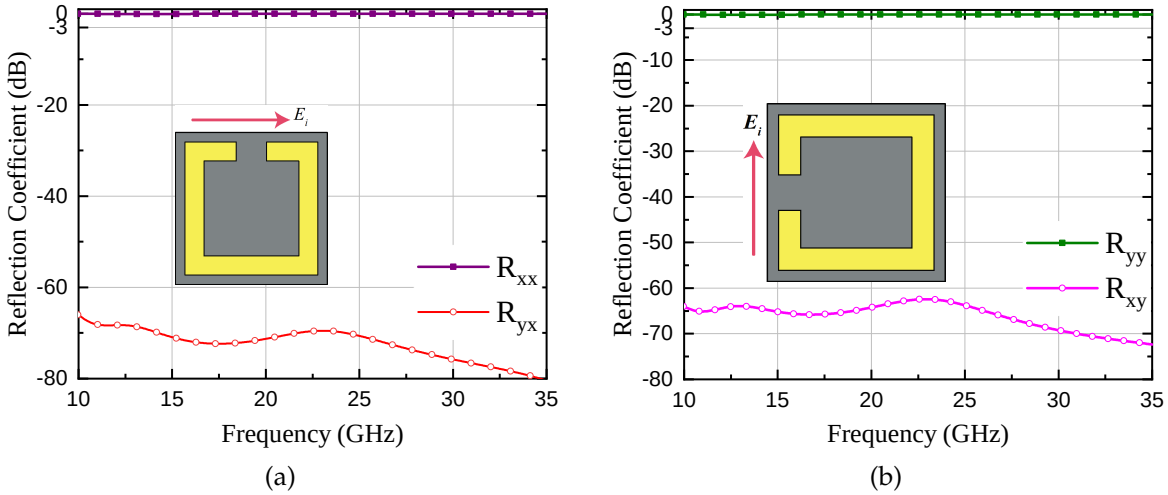

Figure 3.2: Co-polarized and cross-polarized reflection coefficient for single split cell (a) X-polarized wave (b) Y-polarized wave

Here, E_r and E_i denotes the E fields of the reflected and incident wave, respectively. Therefore, the co-polarized component is the ratio of E-fileds of identically polarized waves while the cross-polarization refers to the ratio of E-fields of Y-polarized reflected wave to the X-polarized incident wave. In the similar fashion, for Y-polarized waves, and the two ratios are defined as R_{yy} (co-polarized) and R_{xy} (cross-polarized).

The PCR is a performance indicator that is used to evaluate the effectiveness of the polarization conversion, and its definition is as follows:

$$PCR = \frac{|R_{yx}|^2}{|R_{xx}|^2 + |R_{yx}|^2} \tag{3.2}$$

The simulation results of proposed MS, when excited with X- and Y-polarized waves are depicted in Figure 3.3(a) and (b), respectively. The proposed MS can be seen to operate between 11 and 35 GHz, with three resonances located at 12.24, 16.95, and 30.22 GHz, respectively, as shown in Fig. 3.3(a). At these frequencies, the MS acts as an almost ideal polarization converter. This behaviour can also be verified by the PCR values displayed in Figure 3.4. Similarly, simulation results for the Y-polarized impinging waves are depicted in Fig. 3.3(b) in terms of co-

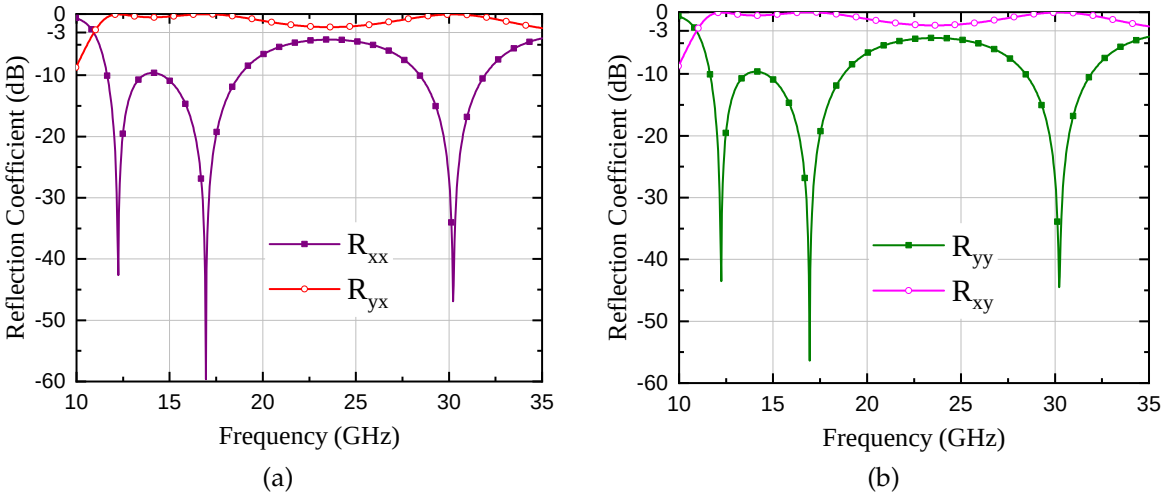

Figure 3.3: Co- and cross-polarized components for (a) X and (b) Y-polarized incident wave.

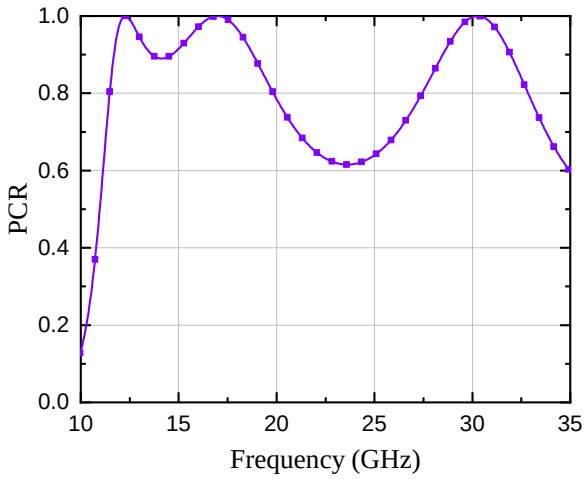

Figure 3.4: Efficiency of polarization conversion of the proposed MS.

polarized and cross-polarized components. The proposed MS, as demonstrated, is effective across the operating range for vertically polarized waves.

The PCR versus frequency response is depicted in figure 3.4 for the purpose of validating the polarization conversion efficiency of the proposed MS. The figure makes it very clear that the PCR is significantly higher than the threshold value of 60% (or 0.6 on the normal scale) [85] across the entire operating range.

3.3 STABILITY ANALYSIS FOR OBLIQUE INCIDENCE

In the real world, it is never possible to have only normal incident waves. In order to be in compliance with this, the MSs should also respond for incident waves that arrives from an angle other than normal. For both horizontally and vertically polarized waves, an oblique incident angle of up to 40° is considered while analyzing the proposed MS.

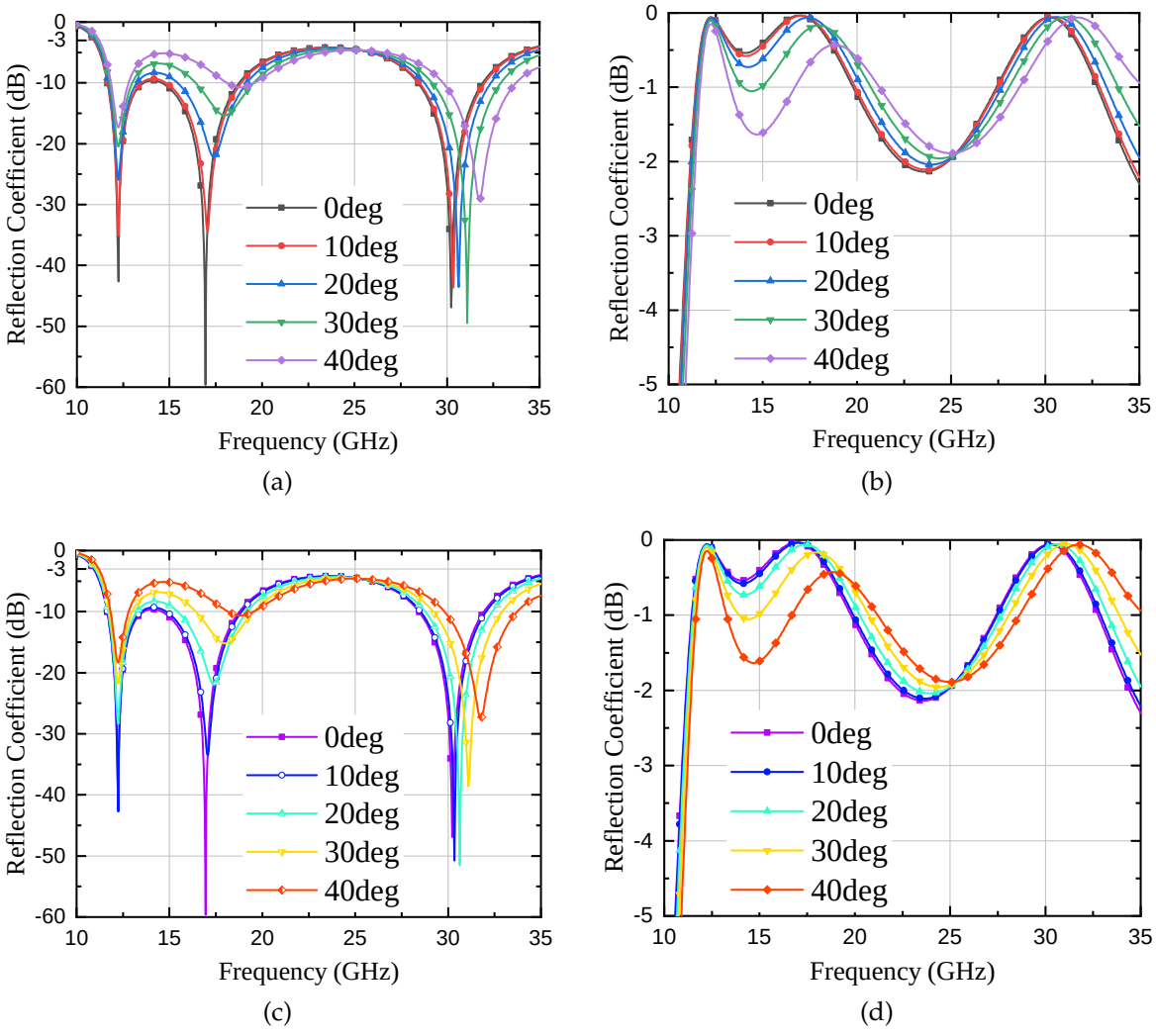

Figure 3.5: Angular stability response for oblique incidence (a) R_{xx} (b) R_{yx} (c) R_{yy} (d) R_{xy}.

The co- and cross-polarized components of a horizontally (X) polarized wave are shown in Fig. 3.5(a) and (b), respectively. While Fig. 3.5 (c) and (d) demonstrates the co- and cross-polarized components for a vertically (Y) polarized wave. It can

be concluded from these figures that the proposed MS is functional across the entire frequency band for incident waves with an angle of up to 40 degrees.

3.3.1 *A novel approach for stability analysis under oblique incidence*

To establish the angular stability of a MS, S-parameter analysis is mostly used. However, there is a lack of information regarding the excitation of MSs and the measurement of reflection angles in the existing literature. In this work, another approach to analyze the angular stability of an MS is reported. The method was successfully verified by EM simulations on three distinct MS configurations having 3×3, 6×6, and 9×9 unit cells respectively. In Figure 3.6(a) and (b), respectively, we see a schematic representation of the MS and the simulation setup that corresponds to it.

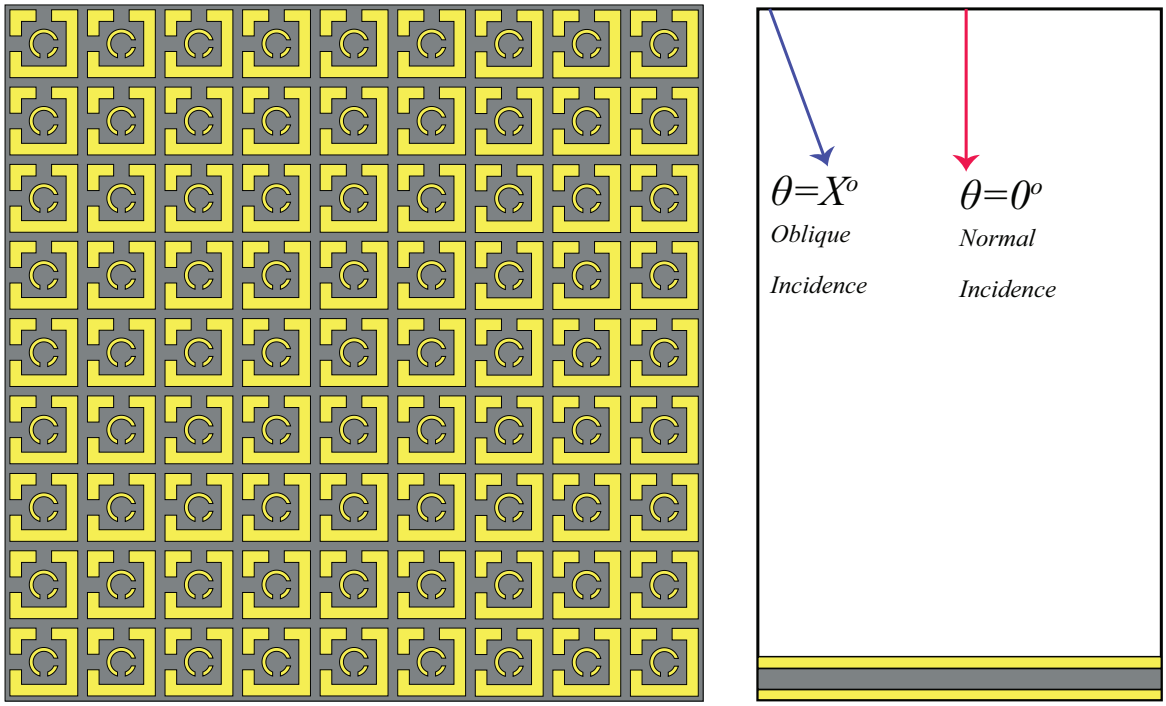

Figure 3.6: (a) Metasurface of 9×9 unit cells (b) Simulation setup.

The simulation was carried out for different incidence angles: normal incidence (θ_i=0°), oblique incidence (θ_i=15°, 35°, 40°, 45°, 60°). The direction of the reflected

beam changes depending on the incidence angle, as can be observed from the results displayed in Figs. 3.7(a-r). In the case of normal incidence, as shown in Figure 3.7(a,g,m), the direction of the reflected beam is at θ_r=0°; however, in the case of oblique incidence of 15°, as shown in Figure 3.7(b,h,n), the beam is observed at θ_r=15°; therefore, it can be concluded that the reflected beam complies with the reflection law. This is also the case when $\theta_i \leq 40°$ (Fig. 3.7(c,d,i,j,o,p)). On the other hand, when $\theta_i > 40°$ the angle of the reflected beam varies with frequency and is not identical to the angle of the incident beam. Based on these figures, it can be established beyond a reasonable doubt that the proposed MS is stable for an oblique incidence of up to 40 degrees.

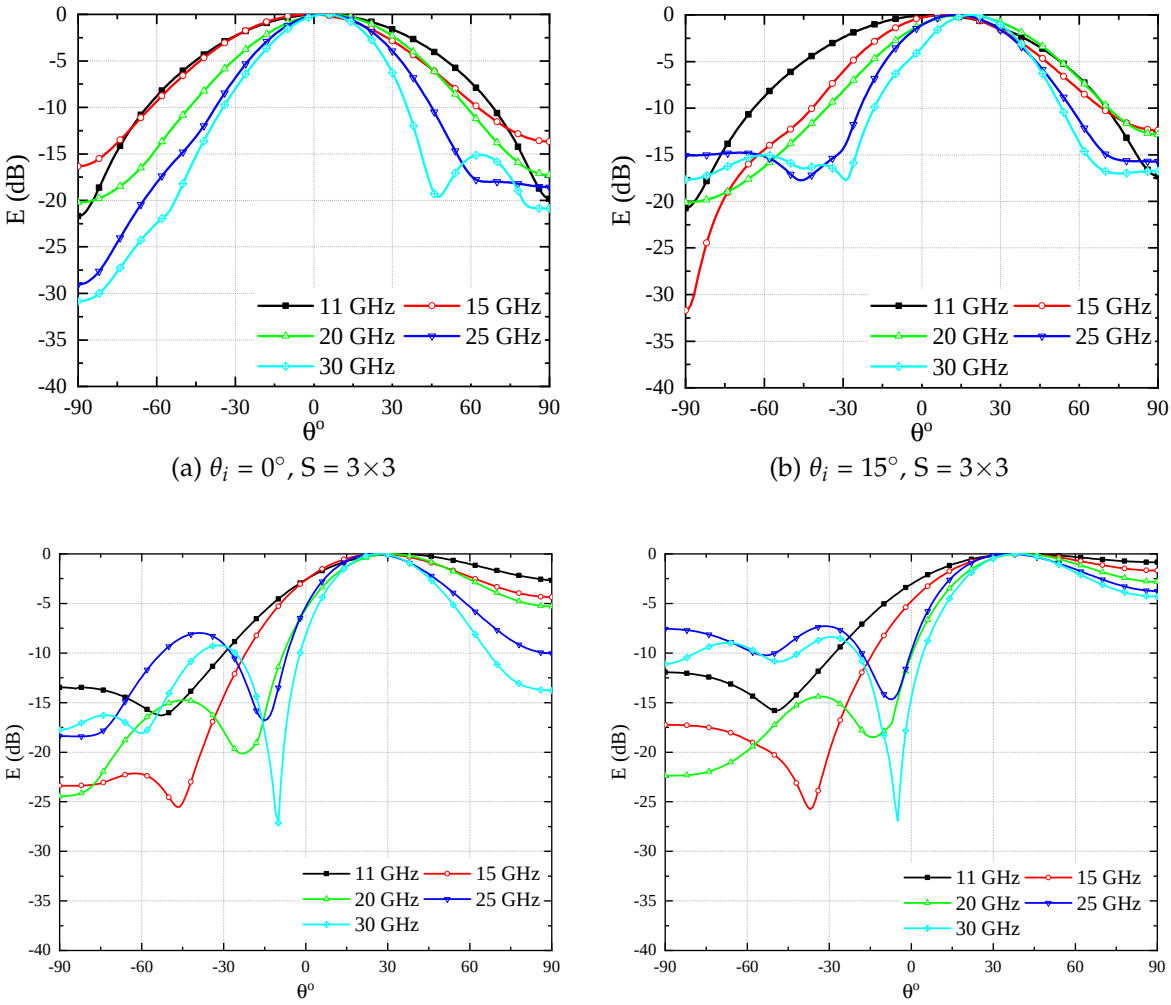

(a) θ_i = 0°, S = 3×3

(b) θ_i = 15°, S = 3×3

(c) θ_i = 35°, S = 3×3

(d) θ_i = 40°, S = 3×3

Figure 3.7: Reflection angle measurement results for proposed MS. (S indicates the size of the MS)

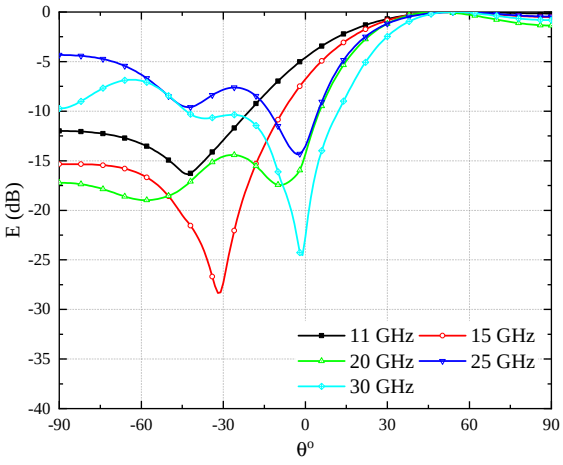

(e) θ_i = 45°, S = 3×3

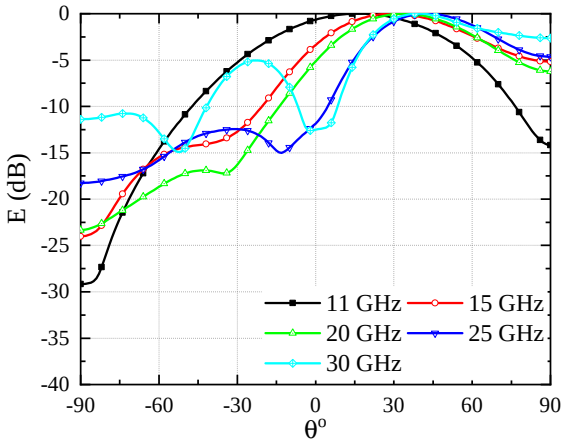

(f) θ_i = 60°, S = 3×3

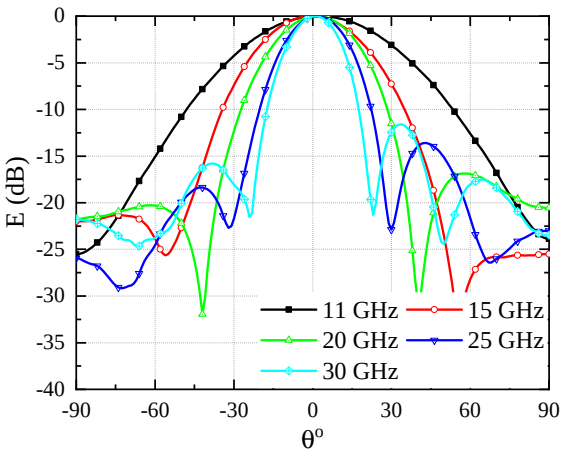

(g) θ_i = 0°, S = 6×6

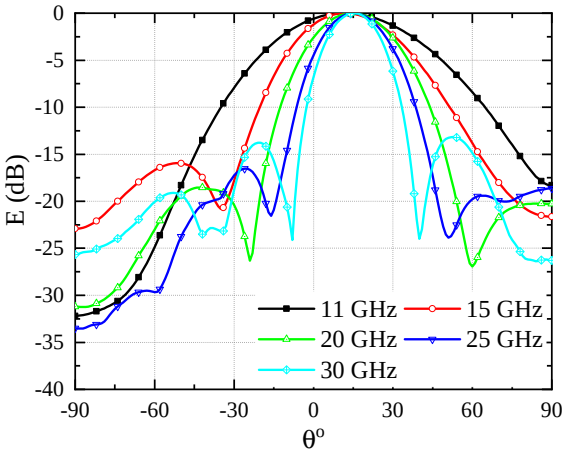

(h) θ_i = 15°, S = 6×6

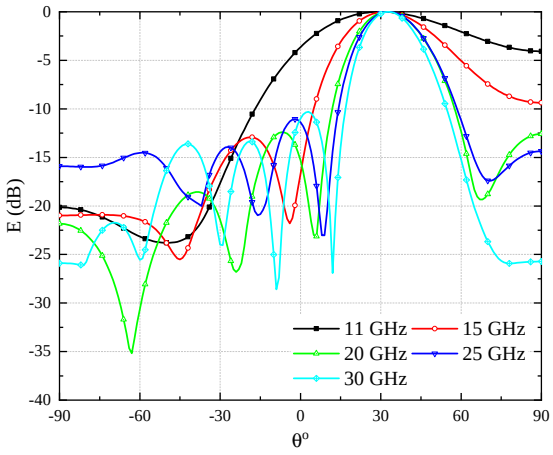

(i) θ_i = 35°, S = 6×6

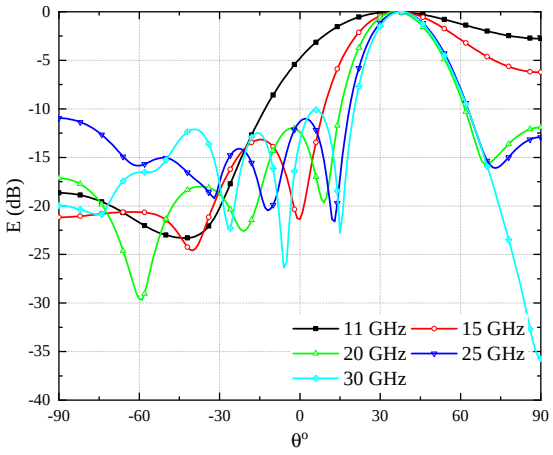

(j) θ_i = 40°, S = 6×6

Figure 3.7: Reflection angle measurement results for proposed MS. (S indicates the size of the MS)

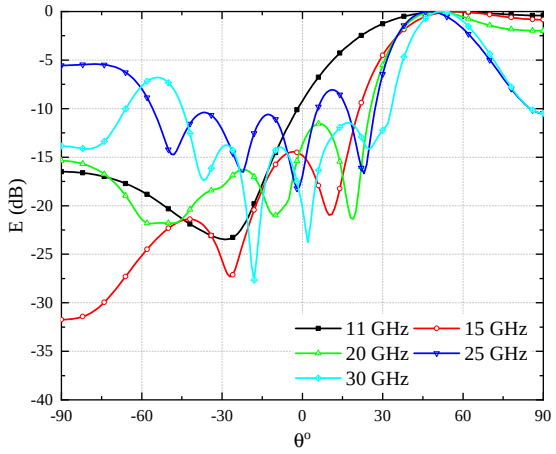

(k) θ_i = 45°, S = 6×6

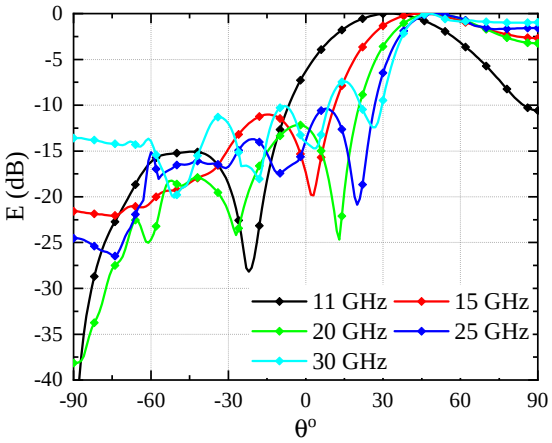

(l) θ_i = 60°, S = 6×6

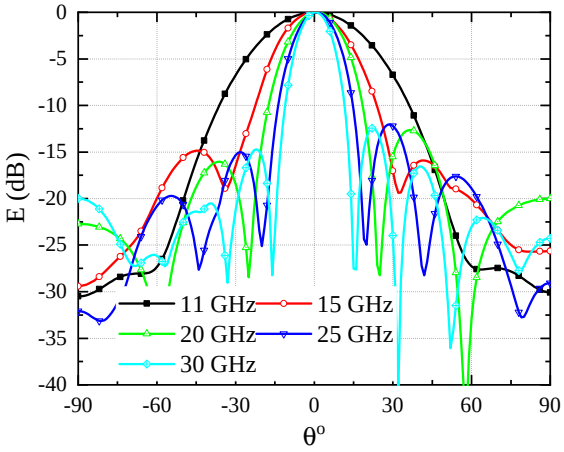

(m) θ_i = 0°, S = 9×9

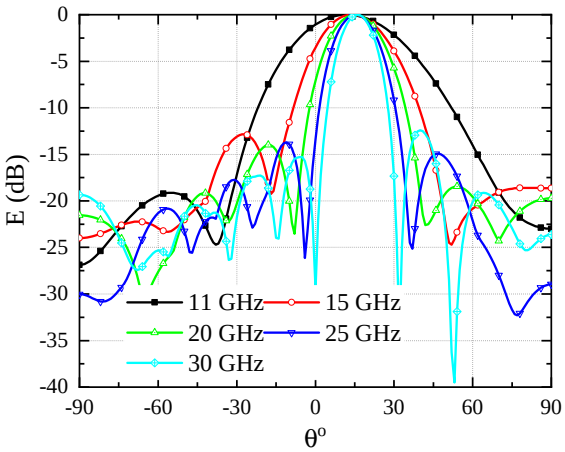

(n) θ_i = 15°, S = 9×9

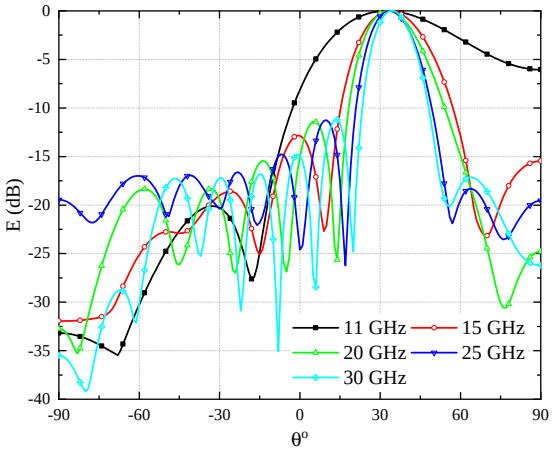

(o) θ_i = 35°, S = 9×9

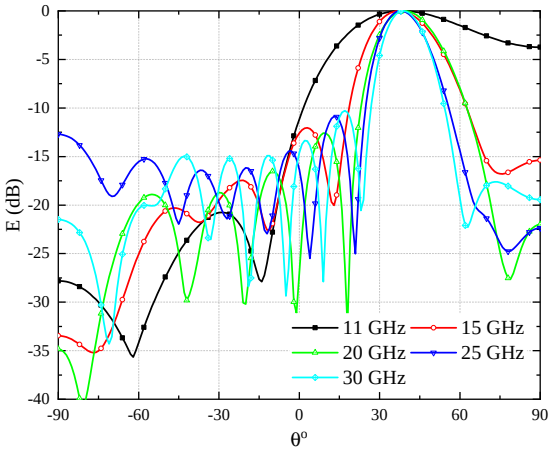

(p) θ_i = 40°, S = 9×9

Figure 3.7: Reflection angle measurement results for proposed MS. (S indicates the size of the MS)

.

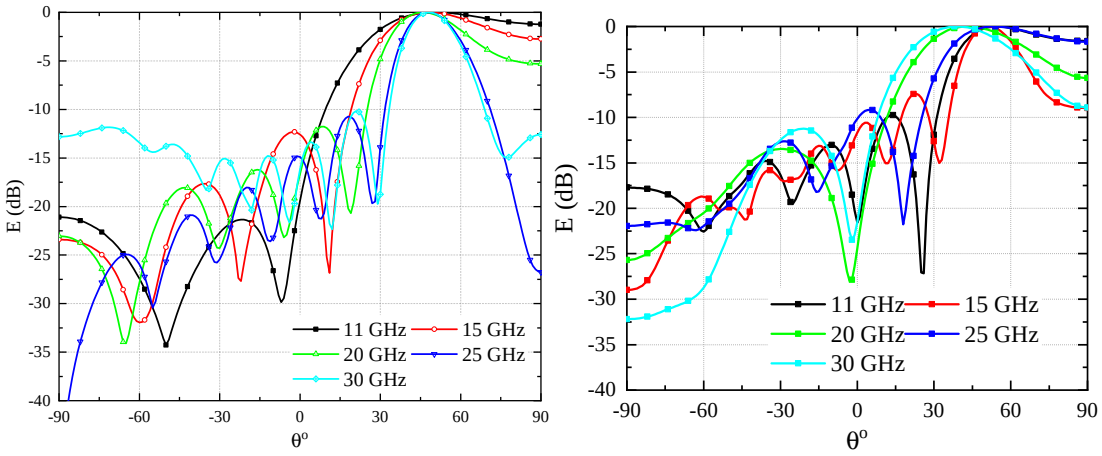

(q) θ_i = 45°, S = 9×9 (r) θ_i = 60°, S = 9×9

Figure 3.7: Reflection angle measurement results for proposed MS. (S indicates the size of the MS)

In addition, it can be concluded from Fig. 3.7 (θ_i=0°,15°) that as the size of the MS increases, the reflected beam starts to shrink, which indicates that of course, the gain of the reflecting surface increases with the size. This is as a result of the fact that as area increases, more power falls (hence less spillover) on the MS, which is responsible for the strong reflections.

A comparative study is conducted with the existing literature, and the findings are summarized in Table 3.2. It can be concluded that the proposed MS yields a higher bandwidth while maintaining miniaturized footprints.

Table 3.2: Comparison study with previous work.

Reference	**Bandwidth (GHz)**	**Size(%) compared to the proposed work**
[77]	5 - 9.7 &11.2 – 15	67.3
[78]	7 - 9.18 &11.66 – 20.40	84
[79]	16 - 32	36
[80]	6.7 - 20.7	84
[81]	6.2 - 24.3	55.5

Continued on next page

Table 3.2: Comparison study with previous work. (Continued)

[82]	5 - 15	67.3
[84]	4.2 - 13.9	84
[85]	7.4 - 10.5 &12.7 – 20	67.3
[86]	5.7 - 11.4	84
[88]	9.44 - 22.38	63.3
Proposed work	10.92 - 35	–

3.4 SUMMARY

The chapter focuses on a super wideband MS that is also stable for incoming waves impinging from an angular direction. The proposed MS has an operating frequency range starting from 11 to 35 GHz. An incident wave with X-polarization can be converted into a Y-polarized wave, and vice versa. In addition, performance under oblique incident waves is also investigated, and the results demonstrate that the proposed design operates effectively up to 40 degrees.The polarization conversion challenges faced by SWB applications may have a possible answer in the form of the proposed MS.

4

PLANAR STRUCTURE-3 : INTELLIGENT REFLECTIVE SURFACES

4.1 INTRODUCTION

The theoretical conceptualisation of manipulation of EM waves by playing with the properties of material was first reported in [25]. These were named Metamaterials. Later in 2001, an experimental validation was performed and reported in [89]. The prototype and the experimental setup are shown in Fig. 4.1 (a) and (b), respectively. As shown in Fig. 4.1 (a), a square split ring resonator structure was printed on a 0.25mm thick G10 fibreglass circuit board material. The rings and wires are on opposite sides of the boards, and the boards have been cut and assembled into an interlocking lattice.

In Fig. 4.1(b), the experimental setup used to measure the Metasurface (MS) properties is shown where the fabricated sample and the microwave absorber are kept between two aluminium plates. These plates are circular in shape with a radius of 15cm. The distance between these plates is 1.2cm. The black arrow indicates the direction of the beam refracted by the material of the positive index. The transmitted power spectrum was measured as a function of angle, θ, from the interface normal while the detector was rotated around the circumference of the circle in 1.5° increments. A waveguide to coaxial adapter with a typical X-band waveguide attached to it served as the detector.

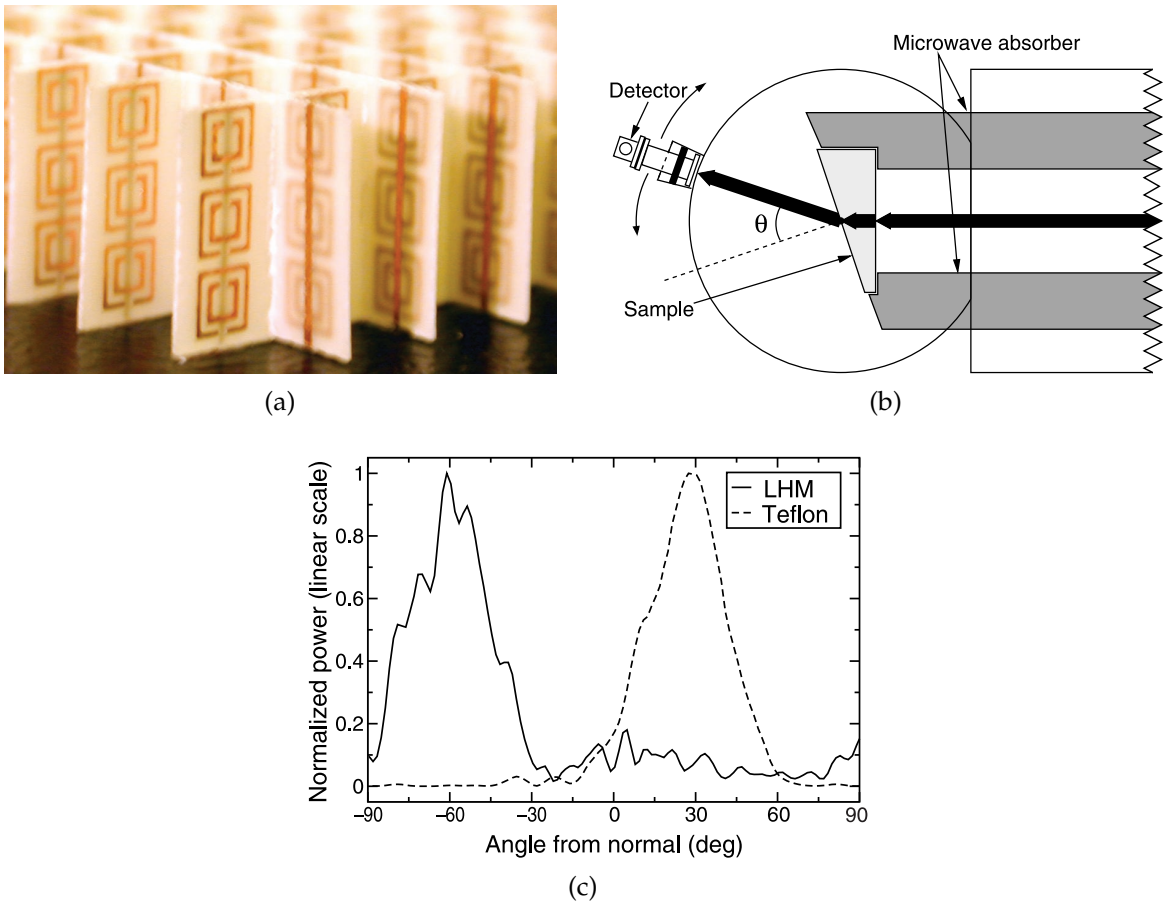

Figure 4.1: (a) Fabricated prototype of the metamaterial (b) experimental setup (c) Transmitted power (at 10.5 GHz) as a function of refraction angle [89]

Fig. 4.1(c) illustrates the transmitted power (at 10.5 GHz) as a function of the refraction angle. A Teflon sample and a Left Handed Metamaterial (LHM) have been used in the experiment. Each curve is normalized to its maximum and therefore the maximum magnitude is *1*. As can be observed from the results, the refracted peak power for the Teflon is 27°, thereby resulting in a positive refractive index of 1.4±0.1. On the other hand, for the LHM sample, the peak power is observed at -61° that results into a refractive index as -2.7±0.1.

In recent years, MS have emerged as one of the thrust research areas of wave propagation. These are 2D sheets comprising metamaterial properties [90] and are of sub-wavelength size. Intelligent Reflective Surface (IRS), in general, are the MS that can be used to manipulate ElectroMagnetic (EM) waves to achieve non-specular reflection. To change the behavior of the MS for an incoming wave, each meta atom can be configured differently. In that way, a MS can serve different

purposes based on users' needs [91, 92]. Within the scope of this thesis work, one MS is proposed that can fulfil two objectives simultaneously, an absorber and a reflector by means of the novel exploitation of tunable ferroelectric materials.

Metasurfaces, based on reconfigurability, can be divided into two broad categories i.e. locally tuned MS and globally tuned MS.

4.1.1 *Locally Tuned Metasurfaces*

As the name implies, locally tuned MSs have an independent control mechanism for each unit cell. Though the degree of freedom increases the complexity of the circuits increases respectively. These MS are mainly used to achieve specular/ non-specular reflection [93, 94], polarization conversion [95], absorber [96], to generate hologram [97] etc.

To achieve tunability, non-linear components such as diodes, transistors, and Integrated circuits are used within each unit cell to manipulate the overall response of the MS. With all these components it is only possible to achieve two states corresponding to on/off conditions. To mitigate this, digital coding can be utilized to achieve more number of states [98, 99].

4.1.2 *Globally Tuned Metasurfaces*

Contrary to locally tuned MSs, these MS achieve tunability by means of external conditions. Therefore, each unit cell does not have an independent control mechanism and results in a much simpler structure. In the literature, a polarization converter capable of working in two different states is reported [100]. A pin-diode is connected with an array of unit cells to change the states. Similarly in [101], a pin diode is used to change the MS behavior from a polarization converter to a reflector by changing the impedance and phase profile of the MS. An interesting

approach to control the absorption rate using biasing of the transistor is reported in [102].

Another possibility to achieve tunability is by introducing different materials which change their properties with different inputs. This can include semiconductor materials [30], Graphene liquid crystals and polymers [103–105].

4.1.3 *Applications of the Metasurfaces*

As described earlier, metasurfaces have strong capabilities to manipulate EM waves using linear and non-linear devices. Though there are thousands of possibilities for MS applications, however, some major areas where MSs can play a vital role are shown in Fig. 4.2[1].

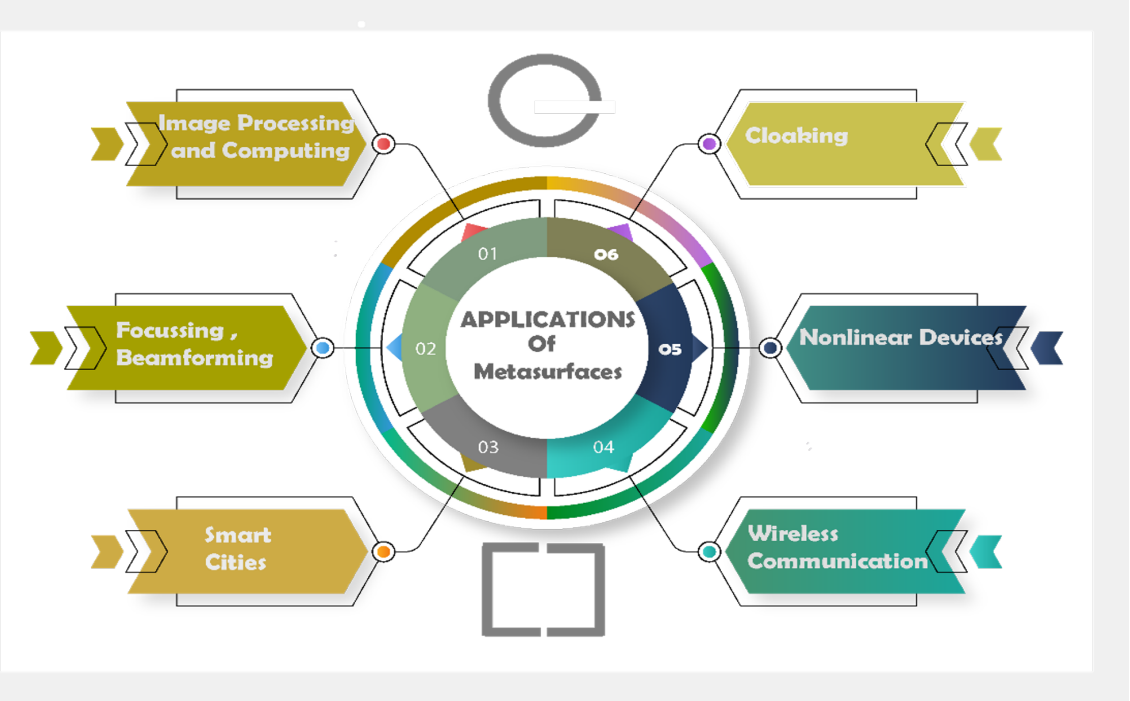

Figure 4.2: Major application areas of the metasurfaces.

Starting from 5G, the concept of a smart environment has gained high attention. To facilitate these environments, an array of intelligent reconfigurable MS is needed. Many researchers around the globe are investigating the inclusion pos-

1 Image taken from freepik.com and edited.

sibilities of IRS in next-generation communication systems [106, 107] and channel models that are suitable to incorporate such structures [108]. For localization and/or tracking applications, the main lobe must follow the object which, in general, is known as beam-steering. IRS can serve the purpose of beam-steering and beam-splitting [109, 110] that can be exploited for localization as well as multi-user coverage. In addition to this, a thorough investigation of the usage of IRS in smart cities is reported in [111].

EM waves can also be radiated with good efficiency through MSs. With the help of a modulated MS, highly directive leaky wave antennas are designed to control the surface wave [112]. Antennas of this type are commonly used in radars. [113]. Using a MS in guiding structures can reduce their size [114]. [114].

Regarding image processing applications, metasurfaces can be used to reproduce the image of an object by means of amplitude and phase information of EM wave using Hologram technique [97].

One such application of the IRS is designing a MS for anomalous reflection which is discussed next in detail.

4.2 IRS FOR ANOMALOUS REFLECTION

When a wave impinges on a reflective surface, it gets reflected as per Snell's law. However, it is of paramount importance to deflect the incoming waves (from a fixed Tx) to a non-specular direction for a complete coverage solution. This type of manipulated wavefront is known as anomalous reflection. One such MS for anomalous reflection is presented in [94] which is the foundation of our current research discussed later in this thesis.

A schematic of the proposed unit cell is shown in Fig. 4.3. The intelligent MS comprises two metallic patches over a continuous ground plane. The metallic thickness of both the patch and the ground plane is 17.5μm while the gap between patches is 1mm. The MS is designed on a 1.016mm thick Rogers/RT5880 (ε_{rel} =

2.2, $\tan\delta = 0.0009$) substrate. The MS can be used for two different applications i.e. tunable perfect absorption (TPA) for different incidence angles and tunable anomalous reflection (TAR) toward different directions. To achieve them, a tunable

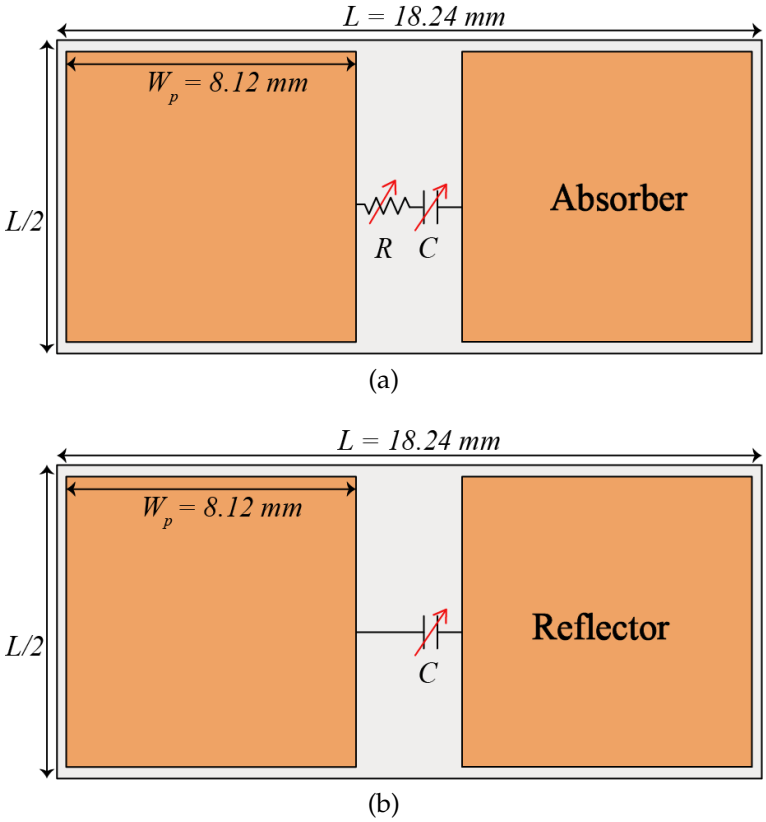

Figure 4.3: Unit cell of the intelligent MS (a) absorber (b) reflector [94]

integrated circuit (IC) is introduced between the metallic patches of the unit cell, as schematically shown in Fig. 4.3. The ICs can be modelled as continuously tunable, lumped complex impedance loads, with a tunable capacitance C (negative reactance) and a tunable resistance R. The capacitance typically controls the spectral position of the resonance, while the resistance controls its strength and absorption level. As a result, TPA is a rather straightforward task as when the unit cell is tuned to have resonance at 5GHz by changing the capacitance C, perfect absorption can be achieved by tuning the resistance R. Realization of TAR, however, is more demanding. To achieve the anomalous reflection the size of the unit cell should be as sub-wavelength as possible. This helps in fine resolution in reflection angles [94].

The simulation of the unit cell was performed in the commercially available EM software Ansys HFSS. The simulation setup and corresponding results of the

absorber and reflector shown in Fig. 4.3 are shown in Fig. 4.4. The MS is excited

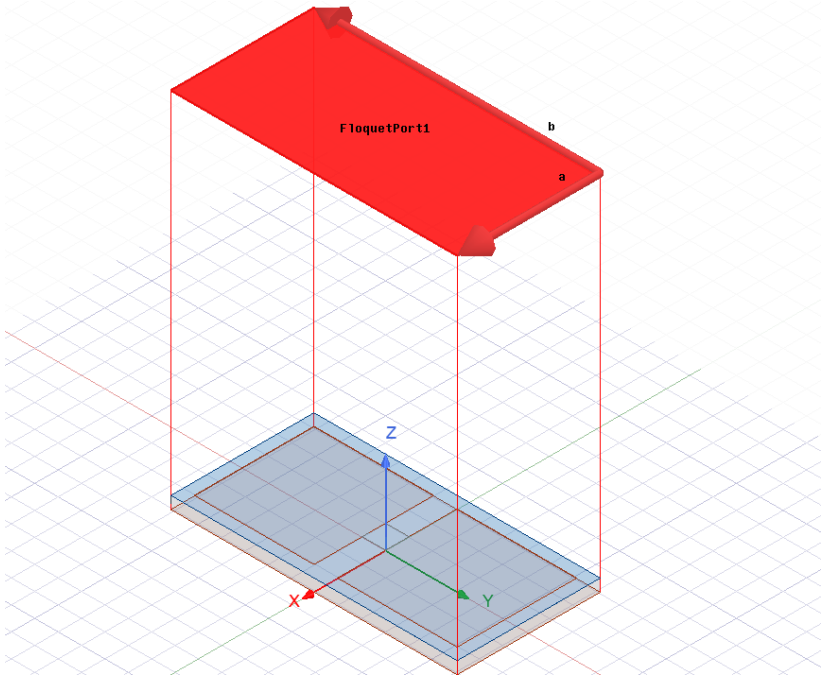

(a)

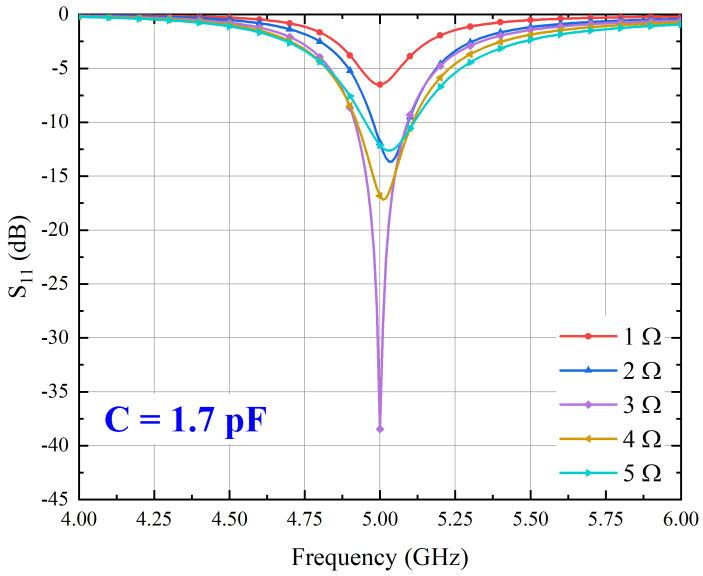

(b)

Figure 4.4: (a) Simulation setup and results of the proposed unit cell (b) simulation results of the absorber

using a plane wave impinged through the Floquet port placed at $\lambda/4$ distance in +Z direction. In the $\pm$Y and $\pm$X directions, periodic boundary conditions (PEC and PMC) are applied. This is a conventional method to simulate periodic structures that compute the responses by extending them infinitely in X and Y directions.

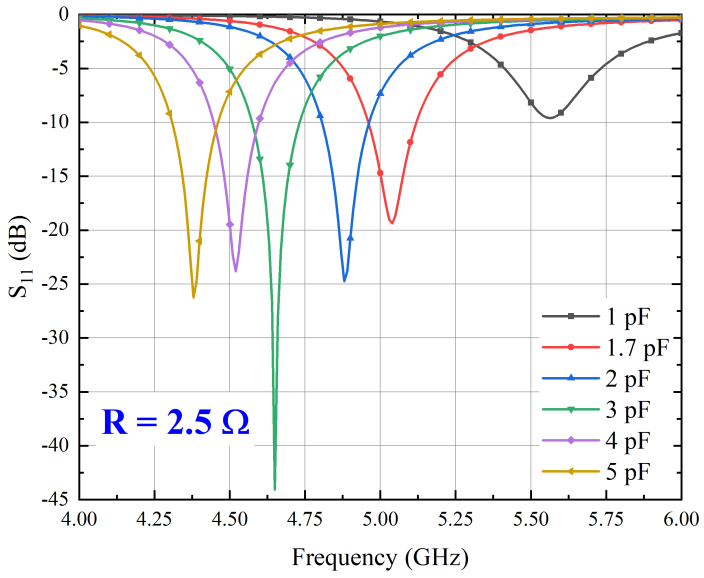

(c)

Figure 4.4: (c) simulation results of the reflector [94]

The simulation results of the unit cell behaving as an absorber and reflector are shown in Fig. 4.4 (b) and (c). It can be observed from the figure that the absorption level increases with increasing resistance for a constant capacitor. Similarly, for a fixed resistance, the operating frequency can be tuned by changing the capacitance value. To optimize the response for 5 GHz, the value of capacitance required is 1.7pF as shown in Fig. 4.4(b).

4.2.1 *Supercell configuration*

To achieve anomalous reflection (hence R=0Ω) along with the sub-wavelength size of the unit cell, the phase profile of the reflection coefficient with capacitance is equally important. For fine-tuning the capacitance values, the phase variation must be as wider as possible. The reflection coefficient magnitude and phase variation with capacitance are shown in Fig. 4.5. As can be observed from the figure, the magnitude of the reflection coefficient is almost flat indicating nearly perfect reflection, while the phase changes rapidly between 1-2pF. This range helps in achieving the desired response of anomalous reflection. A schematic of a supercell consisting of

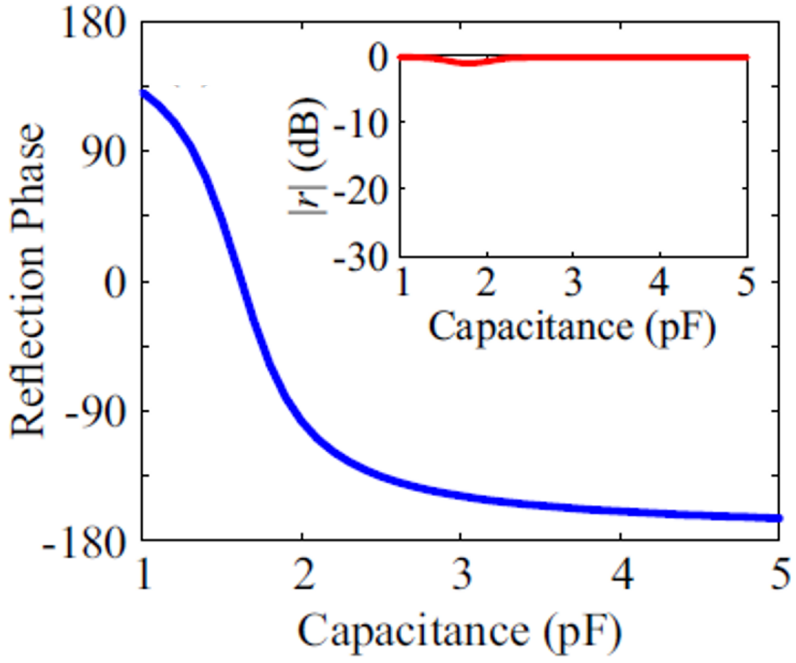

Figure 4.5: Magnitude and phase profile of the reflection coefficient of the unit cell. [94]

8-unit cells is shown in Fig. 4.6. Depending on the size of the supercell, the num-

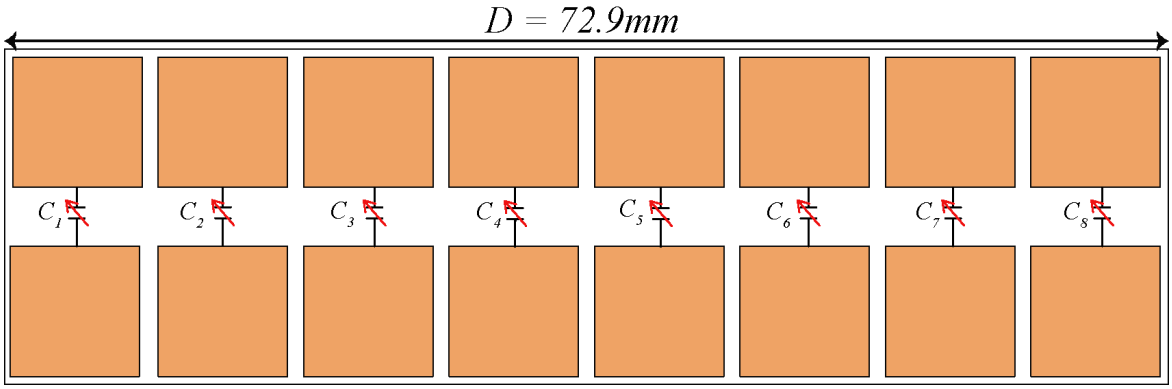

Figure 4.6: Supercell consisting 8-unit cells.

ber of diffraction modes, m, for wavefront are calculated. To achieve anomalous reflection, the total length of the supercell (D) must be greater than $1\lambda_0$. If the size is within $1\lambda_0 < D < 2\lambda_0$, the number of diffraction modes would be two (m=$\pm$1) besides specular mode (m=0). It is important to mention that three modes must be calculated during simulation setup to correctly observe the supercell response(Fig. 4.7). When the MS is excited, the incoming wave can be reflected in any of these

modes. The angle of diffraction mode can be calculated using Eq. 4.1. Simulation setup and diffraction modes illustration are shown in Fig. 4.7.

$$\theta_r = arcsin(\frac{m\lambda_0}{D}) \tag{4.1}$$

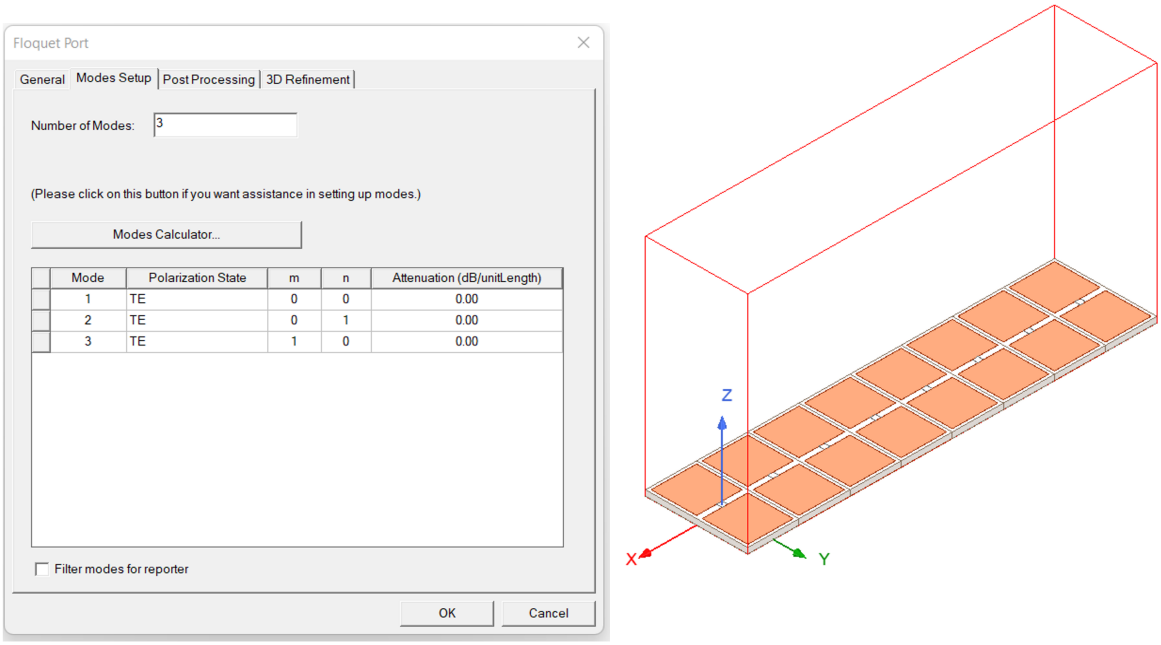

(a)

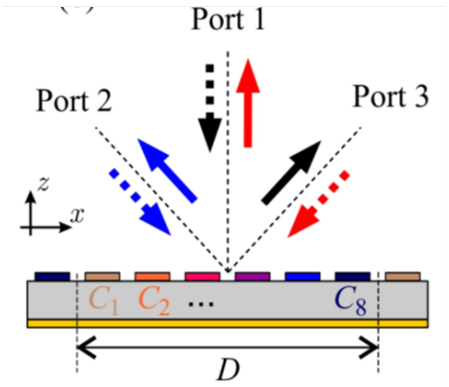

(b)

Figure 4.7: (a) EM simulation setup of a supercell (b) diffraction modes

From Eq. 4.1, it can be concluded that as the size of the supercell increases, the reflection angle range widens. For the presented supercell, the total size is $\sim 1.2\lambda_0$ which reflects the incoming wave towards θ_r=56.3°. The simulated response of the supercell is shown in Fig. 4.8. One can observe from the results that at 5GHz,

incoming power is coupled from port 1 to port 3 ($|S_{13}|$=0dB). Therefore, we can say that an anomalous reflection is happening between ports 1 and 3 while at port 2, retro-reflection is observed i.e. the reflected wave is in opposite direction to the incoming wave.

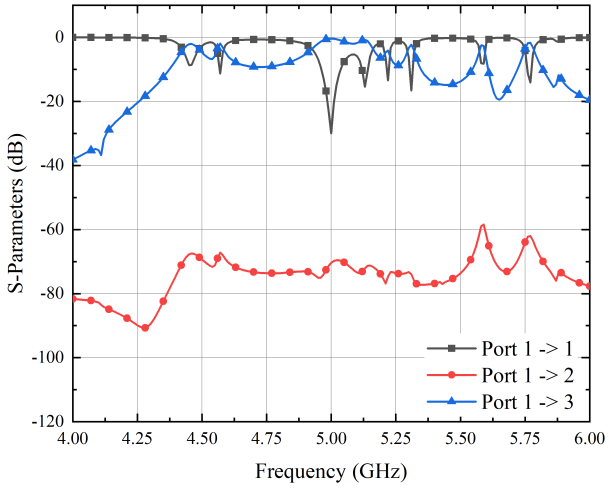

Figure 4.8: Simulated response of the presented supercell. The incoming signal is being directed towards port 3 (at θ_r=56.3°).

Since the reflections in other unwanted directions are being suppressed, it is equally important to compute the efficiency of the system. The efficiency, η, can be calculated using S-matrix as follows:

$$\eta_i = max_x \frac{|S_{xi}|^2}{\sum_x |S_{xi}|^2} \tag{4.2}$$

where the summation over x runs through the number of ports. The efficiency of the presented system is 98%.

4.3 IRS FOR ANOMALOUS REFLECTION USING FERROELECTRIC MATERIALS

Taking inspiration from the previous section, an IRS for anomalous reflection is discussed in this section. It is to be noted that though the idea seems similar, there is a substantial difference in the materials used to design the MS as well

as to control the direction of reflection. The new stack-up comprises a 525μm thick High Resistivity Silicon (HRSi) substrate on which an ultra-thin layer of Zirconium-doped Hafnium Oxide (HfZrO) ferroelectric material is developed. In this way a low-cost, CMOS-compatible, rare-earth-free solution is achievable. Moreover, it loses its hybrid nature (where lumped components have to be soldered ex-post) and assumes a monolithic one, with an increased level of accuracy.

4.3.1 *Ferroelectric Materials : Why?*

Semiconductor materials have found significant importance in achieving tunability, however, due to the forward conduction region the voltage tunability gets limited. On the other hand, ferroelectric materials do not have any forward conduction region that allows for improved power handling and simpler biasing compared with semiconductor materials. Moreover, ferroelectric materials are less complicated to process for a given Q factor and operating frequency and are easy to integrate with other high-Q passive components, which reduces the overall cost of implementation. [115, 116].

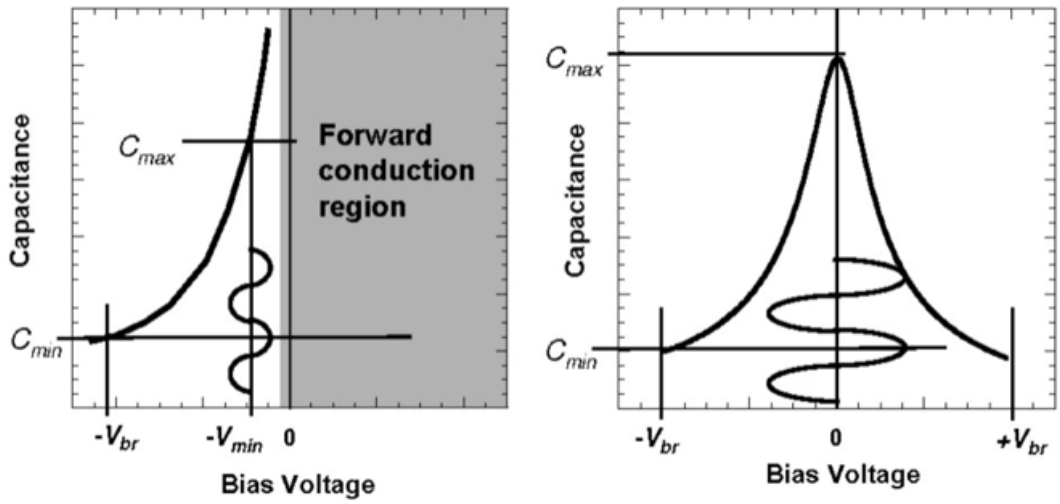

Figure 4.9: Semiconductor varactor (left) and ferroelectric-base device (right) capacitance trend at different input power levels [115].

As a consequence of the fast development in terms of miniaturization and integration on silicon, **HfZrO** ferroelectric material has gained great interest. This material is exploited within the framework of the H2020-NANO-EH European project. The project emphasizes Energy Harvesting (EH) solutions under the paradigm of next-generation IoT, using new nanomaterials that are environmentally friendly.

HfZrO is based on doped HfO_2 that assists following properties:

- Fully CMOS compatible
- Nanometer-thickness (other ferroelectric such as BST have µm-order thickness)
- Large tunability at very low dc voltages

Based on the properties, this material finds its application in decoupling capacitors, phase shifters, microwave antenna arrays and many more. In [117] dielectric properties of HfZrO are reported within the microwave range. It is worth mentioning that material is dispersive in nature and has a large tuning range of dielectric constants with applied bias.

As shown in Fig. 4.10(a), the relative permittivity of HfZrO varies from 35 to 10 within the 1-10GHz frequency range. Variations of ε_{rel} and $\tan\delta$ with applied bias are shown in Fig. 4.10(b). It is important to mention that effect of biasing on dielectric properties is experimentally measured at 10GHz.

4.3.2 *Proposed IRS using HfZrO*

To exploit the properties of HfZrO, an intelligent MS for anomalous reflection is proposed. As the initial step, the unit cell designs shown in Fig. 4.3 are optimized on the new stack-up. The stack-up includes a $525\mu m$ thick silicon substrate with a 10nm thin sheet of HfZrO. The reason behind the ultra-thickness of HfZrO is that it starts losing ferroelectric properties as the thickness increases. The new unit cell

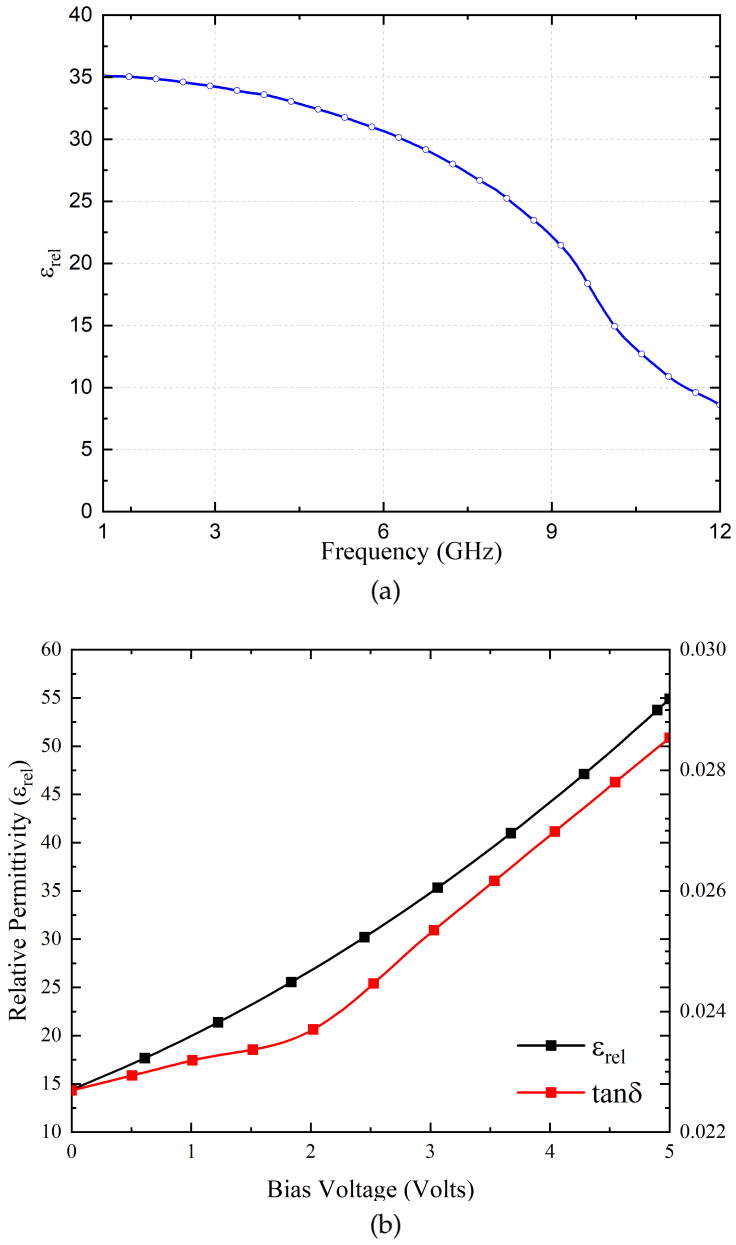

Figure 4.10: HfZrO dielectric properties (a) relative permittivity v/s frequency (b) ε_{rel} and $\tan\delta$ v/s bias voltage (redrawn from [117])

designs are shown in Fig. 4.11 and their corresponding results are shown in Fig. 4.12.

As shown, the new patch dimension is 6.3mm with a gap of 1mm in between. Also from Fig. 4.12(b), it can be observed that the capacitor is shifting the operating frequency towards the left similar to the previous design. Next a supercell consisting of 10-unit cells (therefore D=73mm) is designed. The schematic of the proposed supercell is shown in Fig. 4.13(a).

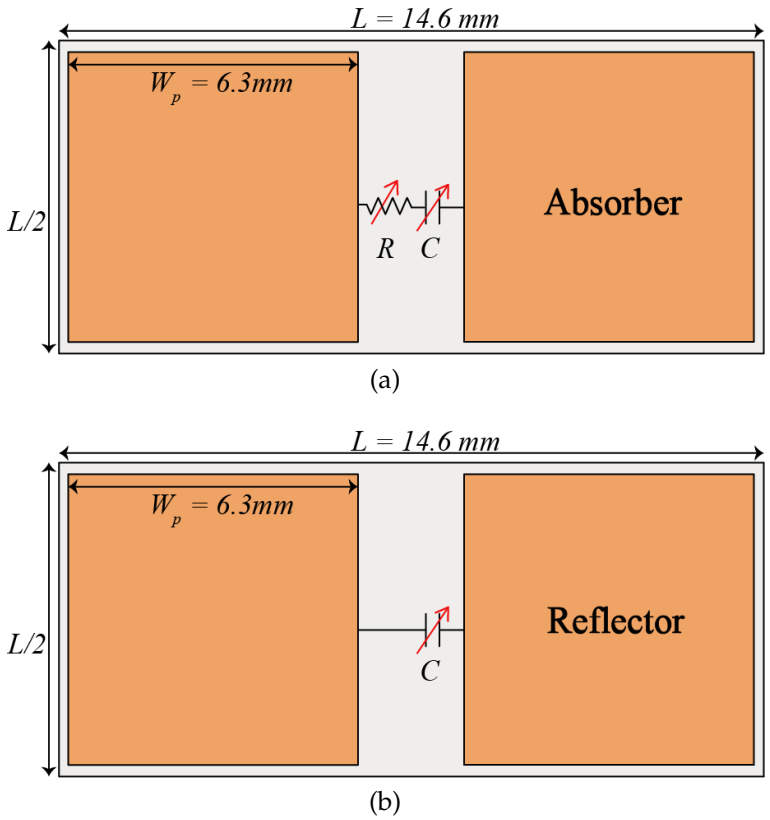

Figure 4.11: Unit cell of the intelligent MS (a) absorber (b) reflector

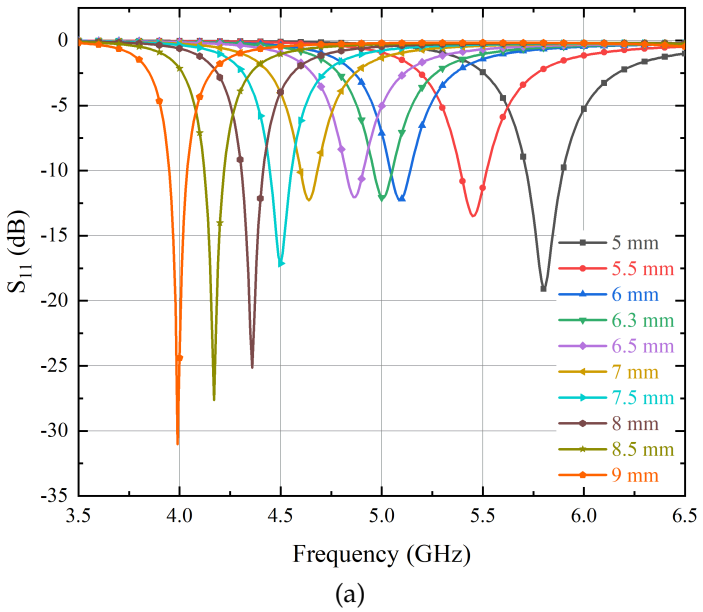

(a)

Figure 4.12: Simulated results of the proposed IRS (a) patch dimension

As established earlier, achieving anomalous reflection magnitude and phase profile of the unit cell with capacitance is highly important. In this work, we have adopted the capacitance within the range of 1 to 6pF. The simulated response of the unit cell with varying capacitance is shown in Fig. 4.13(b). From the figure, it

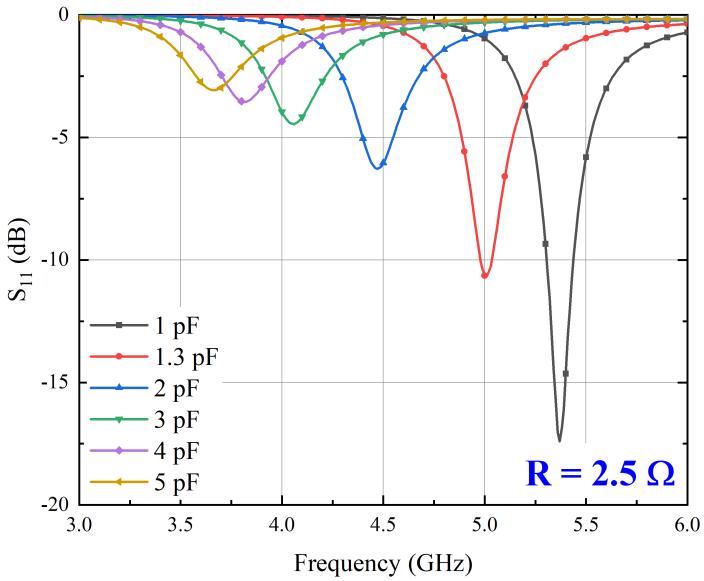

(b)

Figure 4.12: Simulated results of the proposed IRS (b) capacitance tuning

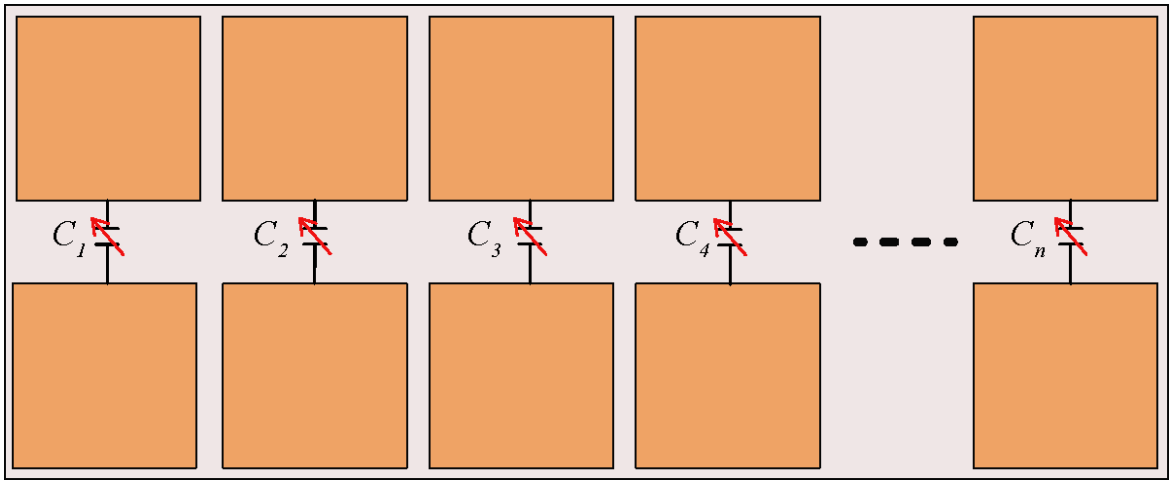

(a)

Figure 4.13: (a) Schematic of the proposed supercell

can be concluded that the proposed IRS is working as an almost perfect reflector for the entire range of capacitors, however, a very small deflection is observed near 5pF. A steep phase response is recorded between 4 and 5pF which can help in tuning the desired response. Since the total dimension of the supercell is $\sim 1.2\lambda_0$, the number of diffraction modes would be two (m=$\pm$1) besides specular mode (m=0) and the angle of reflection θ_r=56.3$\circ$. The simulated response of the supercell is shown in Fig. 4.14. From the results, it can be concluded that power is coupled

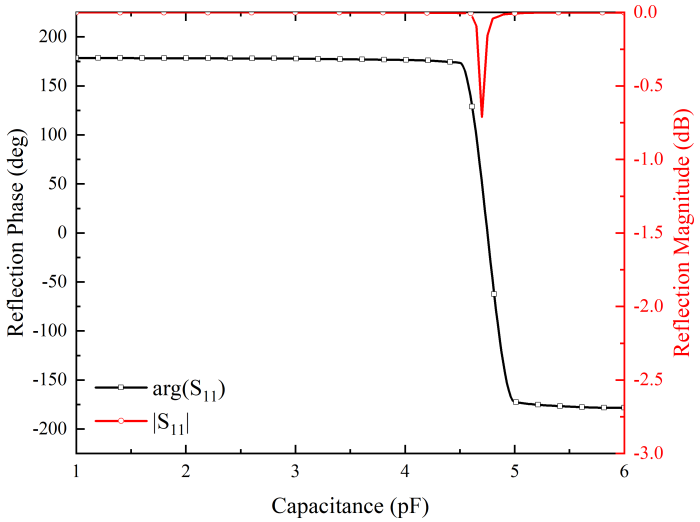

(b)

Figure 4.13: (b) magnitude and phase profile of the reflection coefficient with capacitance.

between ports 1 and 3, providing anomalous reflection, while retro-reflection is observed at port 2.

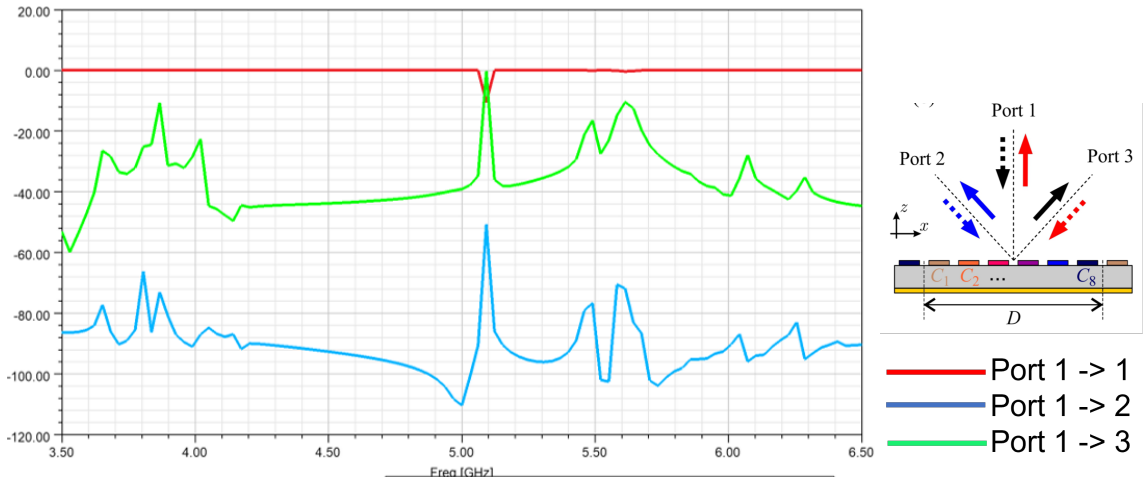

Figure 4.14: Simulated response of the proposed supercell.

At this moment, the proposed IRS is a locally tuned MS where each unit cell response is controlled using a lumped capacitor. To convert the current IRS from local to global tuned MS two changes are recommended in the design:

1. Inclusion of a ferroelectric substrate (HfZrO) above HRSi.

2. Replacement of lumped capacitors with printed capacitors.

For the second objective, an Inter-Digitated Capacitor (IDC) is used. The design and analysis of IDC are explained in the following section.

4.3.3 *Inter-digitated capacitor (IDC)*

Inter-Digitated Capacitor (IDC) is a distributive element and the ferroelectric material properties can be exploited to change its behavior. A schematic of a conventional IDC is shown in Fig. 4.15. As shown in the figure, the capacitance of an

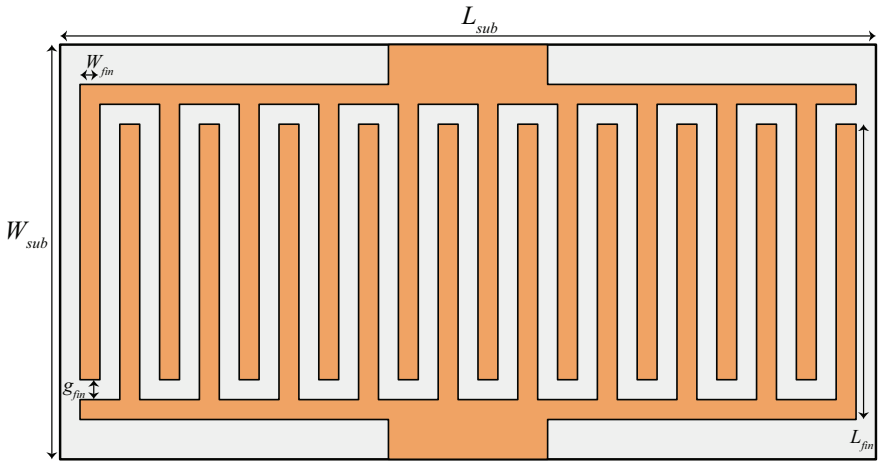

Figure 4.15: Schematic of the IDC with N=10, L_{sub}=2.05mm, W_{sub}=1mm, W_{fin}=0.05mm, g_{fin}=0.05mm, L_{fin}=0.74mm

IDC strongly depends on the number of fingers (N), length of the finger (L_{fin}), and width of the finger ((W_{fin}). To fine-tune the capacitance value, one can play with the gap between the fingers (g) and the end gap at the fingers (g_e). A parametric study was conducted to analyze IDC behaviour with the number of fingers (N) and width of fingers (W_{fin}). The simulated results of the parametric study are shown in Fig. 4.16.

From Fig. 4.16, it can be observed that the capacitance increases with an increase in N and W_{fin}. To calculate the capacitance value corresponding to a particular value of N (or W_{fin}), the mathematical equation shown below can be utilized:

$$C = \frac{-j}{2\pi\ f\ Im[Z]} \tag{4.3}$$

Following this, the capacitance is found to be 0.66pF for N=3 while it increases to 4.63pF for N=12. Similarly, for W_{fin}=0.02mm the capacitance is 1.47pF and for W_{fin}=0.16mm, it increases to 7.44pF. In the first analysis (varying N) W_{fin} was

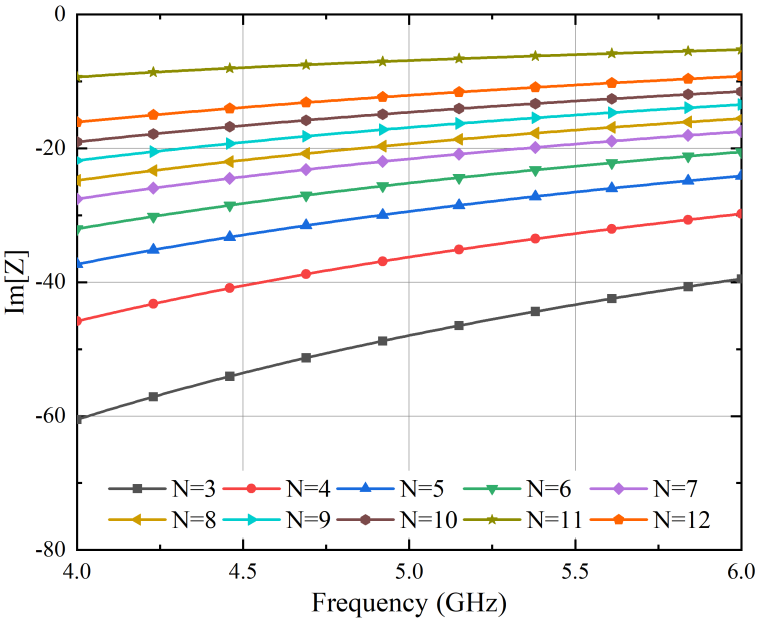

(a)

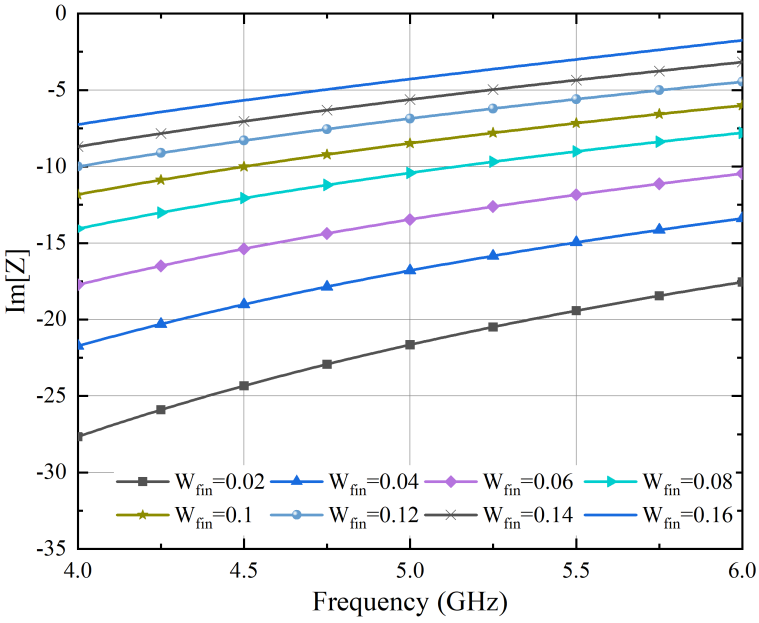

(b)

Figure 4.16: Parametric analysis of IDC with (a) number of fingers (N) (b) width of fingers (W_{fin}).

fixed at 0.05mm while for the second analysis (varying W_{fin}) N was fixed at 10. It is also worth mentioning that due to the restricted gap between unit cell patches, the degree of freedom is restricted for (L_{fin}) and g_e.

In the next step, to exploit the tunability with biasing of the HfZrO, an ultra-thin layer of a few nanometers is placed on the silicon substrate. Since length to height aspect ratio is very high, the EM simulator is not able to detect the HfZrO layer. To

mitigate this issue, local mesh settings are applied to the HfZrO layer. In the local mesh settings, the max. length of the tetrahedron was chosen to be 10nm. The unit cell with local mesh settings and the new stack up is shown in Fig. 4.17.

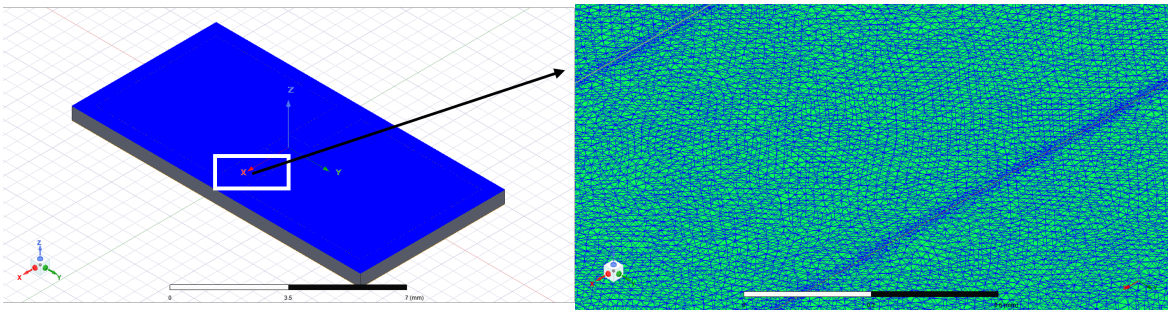

(a)

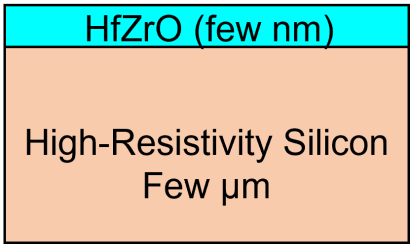

(b)

Figure 4.17: (a) HfZrO with local mesh settings (max length of tetrahedron 10nm) (b) final stack up for proposed IRS

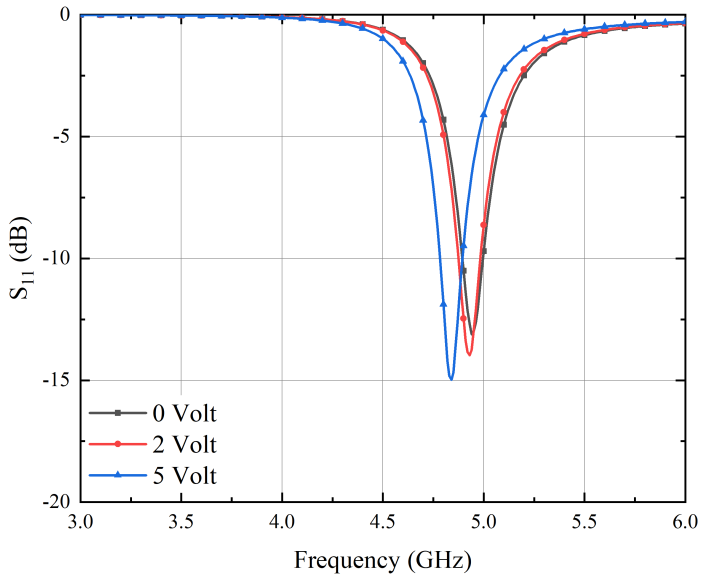

Figure 4.18: Simulation results for different biasing of HfZrO.

Although rigorous mesh settings were applied to the HfZrO layer, the EM solvers are not able to consider the layer during simulation. The simulation results

of the unit cell for different biasing are shown in Fig. 4.18. From the results, it is clearly visible that the reflection coefficient response shifts only 200-300 MHz when biasing voltage is varied from 0 to 5 volts. Under normal circumstances, f_0 at 5 volts should be half of f_0 at 0 volts as ε_{rel} at 5 volts is four times the 0 volts.

To address this issue, co-simulation with circuit solvers (Keysight ADS in this case) is adopted to analyze the proposed MS. As a first step, a non-linear circuital model for a HfZrO-based IDC is developed which is discussed in detail in the following subsection.

4.3.4 *Non-Linear Circuital Model for HfZrO-based IDC*

As established in the previous section, EM simulations of nanometric devices inhibiting nanometric substrates can make the simulations longer and less accurate ($\sim$ days). It is of paramount importance to introduce a circuital model that can avoid the use of EM simulations. The model can be integrated with EM and circuital co-simulations, leading to fast and accurate simulations ($\sim$ seconds). Additionally, the model takes into account the non-linear properties of the device. Based on experimental measurements provided by a partner of the European project NANO-EH, realized on a HfZrO-HRSi multi-layer, a non-linear circuital model has been developed by one of my colleagues. Firstly, as shown in Fig. 4.19, a circuital model of IDC is considered. The circuit is already validated for correctly modelling co-

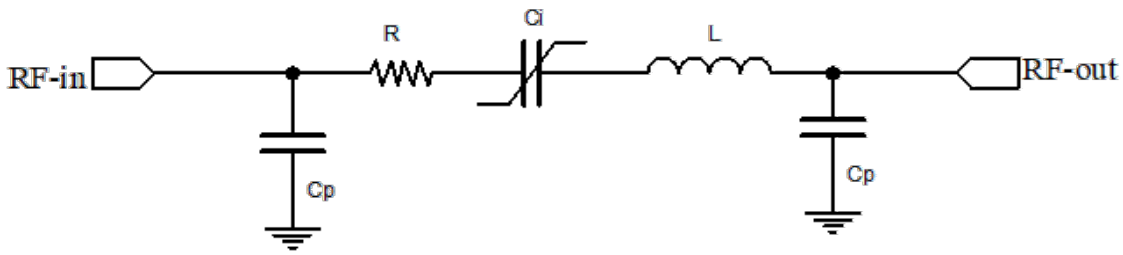

Figure 4.19: Equivalent circuit adopted to develop the non-linear IDC model [118]

planar IDCs [118]. In the circuit, non-linear C_i represents the capacitance between

the IDC fingers. R models the metallization losses. L describes the parasitic inductance of metallization. C_p describes parasitic capacitance between the signal line of the CPW and the lateral ground plane [119].

4.3.5 *Unit cell with Non-linear IDC Model*

Once the non-linear circuital model of IDC is developed, it has been incorporated with the proposed unit cell for achieving the tunability of the structure with HfZrO biasing. Initially, the EM solver response of the unit cell is imported into the Keysight Advanced Design System (ADS) and then the circuital IDC model is connected between the patches. The simulation setup is shown in Fig. 4.20. From the

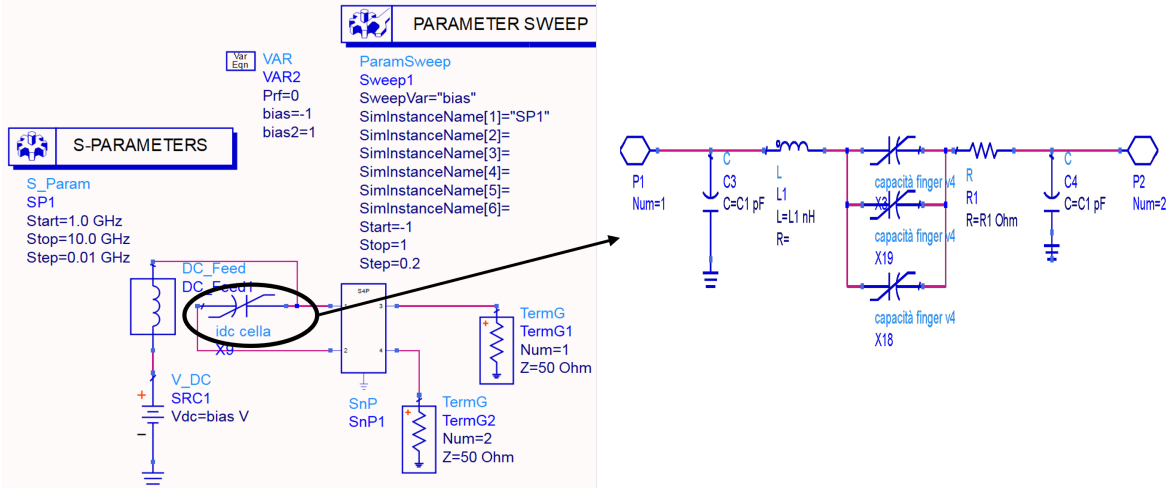

Figure 4.20: Simulation setup of the proposed unit cell with circuital IDC model.

figure, it can be observed that the EM simulation result represents a four-port system. Two of the four ports are input and output ports (hence, incident and reflected wave, respectively) while between the other two ports, non-linear IDC is connected. For high capacitance value, more capacitors can be connected in parallel, however, the effect of parasitic elements needs to be considered. The simulation results of the proposed unit cell with a non-linear IDC model are shown in Fig, 4.21.

It can be observed from the figure that as the bias voltages change from -1 volt to +1 volt, the resonance frequency shifts towards the left. Therefore, it can be con-

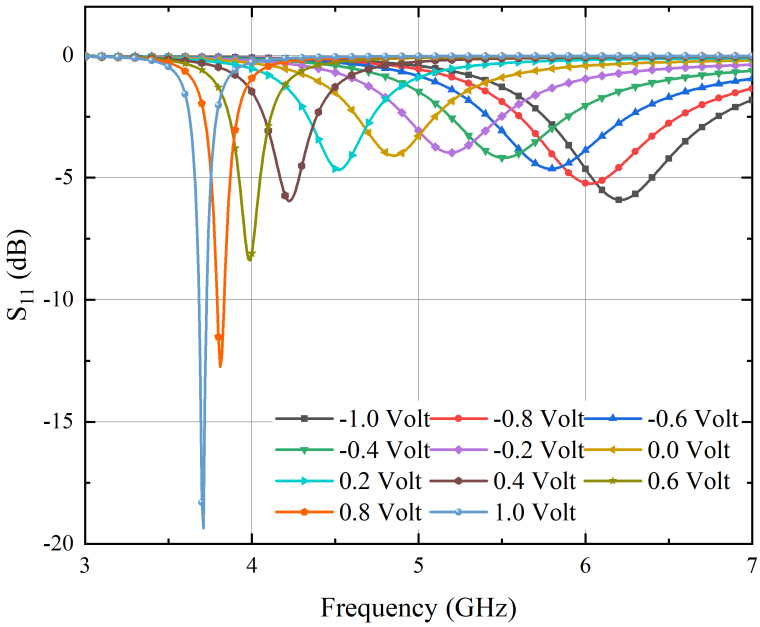

Figure 4.21: Simulation result of the proposed unit cell with circuital IDC.

cluded that the non-linear model of IDC is able to incorporate the HfZrO biasing effects.

4.3.6 *Supercell with Non-linear IDC Model*

As the final step, to achieve anomalous reflection, a similar strategy of co-simulation has been adopted. For a supercell designed using 10 unit cells, a 23-port EM simulation (HFSS) result file is imported in circuit solver (ADS) where 3 ports are for input and reflection (m=0,$\pm$1) and 20 ports are to connect IDC. A simulation setup is shown in Fig. 4.22.

As mentioned earlier, for high capacitance value, more IDC can be connected in parallel, however, the parasitic effect has to be considered and mitigated. The process of optimization to achieve higher capacitance is an ongoing research activity.

4.4 SUMMARY

In this chapter, a detailed methodology to design an intelligent reflective surface is discussed. The proposed MS can achieve two different purposes, absorption and reflection when controlled locally using a lumped RC network. Further, to propagate the incoming waves in a non-specular direction, a cluster of a certain number of unit cells is designed to have different capacitor values for different unit cells. The phase profile of the unit cell with respect to the capacitor values is of paramount importance and helps to tune the desired response. In the final part, global tuning is applied by introducing an artificially designed ferroelectric material HfZrO. The material changes its dielectric properties with the applied bias and therefore the overall response of the structure changes. The lumped capacitor is also replaced with IDC for complete microstrip technology and to enable tuning with HfZrO biasing, However, due to technical difficulties of the EM simulators regarding aspect ratio it is not possible to simulate the structure. To overcome this issue, a non-linear circuital model of IDC is developed with which initial results

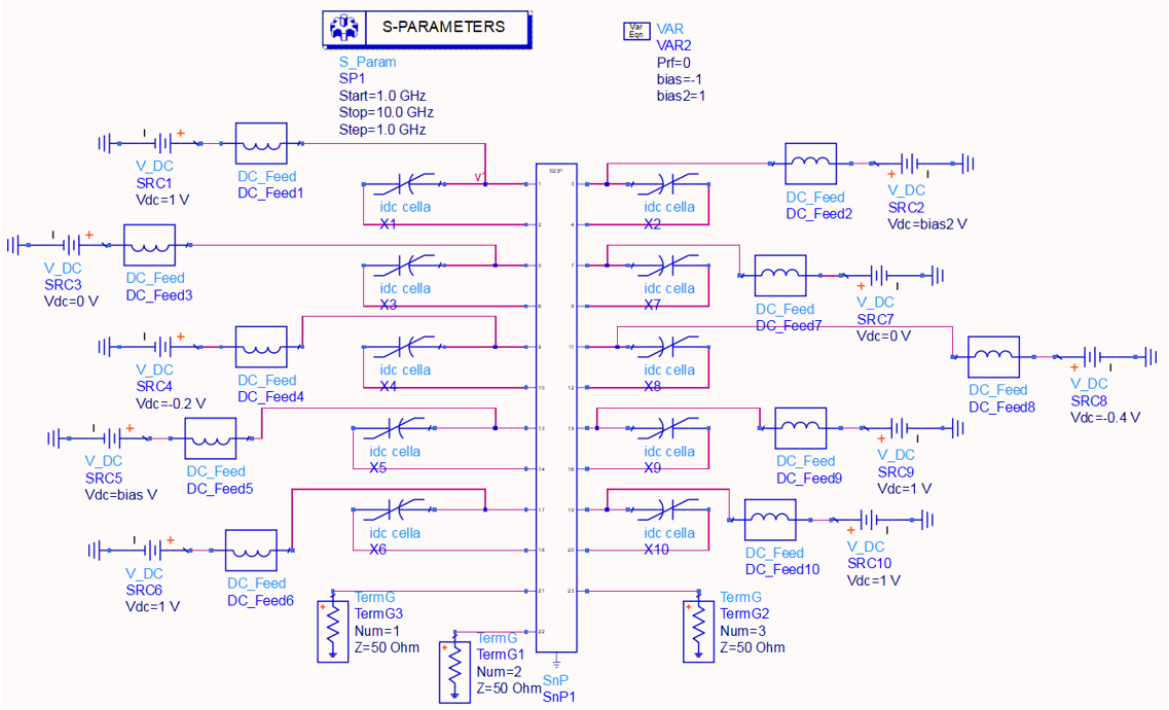

Figure 4.22: Simulation setup of the proposed supercell with circuital IDC model.

have been obtained. The tunable anomalous reflection is part of ongoing research activity.

5

CONCLUSIONS

The thesis focuses on applications of metasurfaces in radiation performance enhancement of planar structures. In particular, three structures are discussed that include an antenna, a polarization converter and an intelligent reflective surface for anomalous reflection.

As the first application, a circularly polarized hybrid conformal antenna serving dual purposes of energy autonomy and UWB communication is designed. A suspended high impedance surface is designed and deployed behind the antenna offering, for the first time, a simultaneous control of the back-radiation mechanism at highly separated frequencies, and of the circular polarization in the UWB band. The exploitation of 3D-printed posts plays a strategic role for both the mechanical stability and the original bi-filar feeding strategy of the proposed multi-layer architecture. Furthermore, a conformal design of the proposed hybrid antenna is studied for future technological systems that would require wireless charging while flying: despite the bidirectional bending, the structure reveals itself to be quite robust to mechanical changes. The proposed radiating system will be able to play a crucial role as an RFID tag of the next generation as soon as it is equipped with the diplexing network, the harvesting section, and the back-scatter modulator.

Further, an angularly stable super wideband metasurface is designed for cross polarization applications. The proposed metasurface has a bandwidth of 24GHz starting from 11GHz to 35GHz. The proposed metasurface is capable of converting the orientation of linearly polarized waves to its orthogonal vector. In addition,

the performance under oblique incident waves is also studied and results show that proposed design operates well up to 40°. It should not left unmentioned that a novel method is reported to validate the angular stability of the proposed metasurface along with S-parameter analysis. Demonstrated results prove the veracity of the proposed methodology.

In the final part of the thesis, a detailed methodology to design intelligent reflective surfaces has been discussed. The proposed metasurface achieves dual purposes of absorption as well as reflection by means of a series RC circuit. When carefully engineered, a cluster of unit cells (termed as supercell) can serve as an anomalous reflector that propagates the incoming waves to a non-conventional direction. Further, An artificially designed ferroelectric material (HfZrO) is used to introduce the tunability with the applied bias. To achieve anomalous reflection, the lumped capacitor has also been replaced with IDCs. However, the optimization of the response has to be tuned and is a part of ongoing research activity.

BIBLIOGRAPHY

[1] F. C. Commission *et al.*, 'Federal communications commission revision of part 15 of the commission's rules regarding ultra-wideband transmission system from 3.1 to 10.6 GHz', *Washington, DC, USA*, 2002.

[2] A. A. Huurdeman, *The worldwide history of telecommunications*. John Wiley & Sons, 2003.

[3] F. Nekoogar, *Ultra-Wideband Communications: Fundamentals and Applications Fundamentals and Applications*. Prentice Hall Press, 2011.

[4] W. Hirt, 'The european UWB radio regulatory and standards framework: Overview and implications', in *2007 IEEE International Conference on Ultra-Wideband*, IEEE, 2007, pp. 733–738.

[5] H. J. Visser and R. J. Vullers, 'Rf energy harvesting and transport for wireless sensor network applications: Principles and requirements', *Proceedings of the IEEE*, vol. 101, no. 6, pp. 1410–1423, 2013.

[6] S. Scorcioni, L. Larcher, A. Bertacchini, L. Vincetti and M. Maini, 'An integrated rf energy harvester for uhf wireless powering applications', in *2013 IEEE Wireless Power Transfer (WPT)*, IEEE, 2013, pp. 92–95.

[7] K. Finkenzeller, *RFID handbook: fundamentals and applications in contactless smart cards, radio frequency identification and near-field communication*. John Wiley & Sons, 2010.

[8] V. Chawla and D. S. Ha, 'An overview of passive RFID', *IEEE Communications Magazine*, vol. 45, no. 9, pp. 11–17, 2007.

[9] B. Anggorjati, K. Çetin, A. Mihovska and N. R. Prasad, 'RFID added value sensing capabilities: European advances in integrated RFID-WSN middleware', in *2010 7th Annual IEEE Communications Society Conference on Sensor, Mesh and Ad Hoc Communications and Networks (SECON)*, IEEE, 2010, pp. 1–3.

[10] E. Ngai, K. K. Moon, F. J. Riggins and Y. Y. Candace, 'RFID research: An academic literature review (1995–2005) and future research directions', *International Journal of Production Economics*, vol. 112, no. 2, pp. 510–520, 2008.

[11] R. Verdone, D. Dardari, G. Mazzini and A. Conti, *Wireless sensor and actuator networks: technologies, analysis and design*. Academic Press, 2010.

[12] D. Kim, M. A. Ingram and W. W. Smith, 'Small-scale fading for an indoor wireless channel with modulated backscatter', in *IEEE 54th Vehicular Technology Conference. VTC Fall 2001. Proceedings (Cat. No. 01CH37211)*, IEEE, vol. 3, 2001, pp. 1616–1620.

[13] D. S. Ha and P. R. Schaumont, 'Replacing cryptography with ultra wideband (UWB) modulation in secure RFID', in *2007 IEEE International Conference on RFID*, IEEE, 2007, pp. 23–29.

[14] C. Mutti and C. Floerkemeier, 'CDMA-based RFID systems in dense scenarios: Concepts and challenges', in *2008 IEEE International Conference on RFID*, IEEE, 2008, pp. 215–222.

[15] M. Z. Win and R. A. Scholtz, 'Impulse radio: How it works', *IEEE Communications letters*, vol. 2, no. 2, pp. 36–38, 1998.

[16] D. Dardari, A. Conti, U. Ferner, A. Giorgetti and M. Z. Win, 'Ranging with ultrawide bandwidth signals in multipath environments', *Proceedings of the IEEE*, vol. 97, no. 2, pp. 404–426, 2009.

[17] Y. Shen and M. Z. Win, 'Fundamental limits of wideband localization—Part I: A general framework', *IEEE Transactions on Information Theory*, vol. 56, no. 10, pp. 4956–4980, 2010.

[18] R. J. Fontana and S. J. Gunderson, 'Ultra-wideband precision asset location system', in *2002 IEEE Conference on Ultra Wideband Systems and Technologies (IEEE Cat. No. 02EX580)*, IEEE, 2002, pp. 147–150.

[19] D. Dardari and R. D'Errico, 'Passive ultrawide bandwidth RFID', in *IEEE Global Telecommunications Conference*, IEEE, 2008, pp. 1–6.

[20] J. Bose, 'The rotation of plane of polarisation of electric waves by a twisted structure', *Current Science*, vol. 70, no. 2, pp. 178–180, 1996.

[21] W. E. Kock, 'Metallic delay lenses', *Bell System Technical Journal*, vol. 27, no. 1, pp. 58–82, 1948.

[22] S. A. Schelkunoff and H. T. Friis, *Antennas: theory and practice*. John Wiley & Sons, 1952.

[23] W. Rotman, 'Plasma simulation by artificial dielectrics and parallel-plate media', *IRE Transactions on Antennas and Propagation*, vol. 10, no. 1, pp. 82–95, 1962.

[24] J. Brown, 'Artificial dielectrics having refractive indices less than unity', *Proceedings of the IEE-Part IV: Institution Monographs*, vol. 100, no. 5, pp. 51–62, 1953.

[25] J. B. Pendry, A. J. Holden, D. J. Robbins and W. Stewart, 'Magnetism from conductors and enhanced nonlinear phenomena', *IEEE transactions on microwave theory and techniques*, vol. 47, no. 11, pp. 2075–2084, 1999.

[26] R. M. Walser, 'Electromagnetic metamaterials', in *Complex Mediums II: Beyond Linear Isotropic Dielectrics*, SPIE, vol. 4467, 2001, pp. 1–15.

[27] Z. Chen, B. Guo, Y. Yang and C. Cheng, 'Metamaterials-based enhanced energy harvesting: A review', *Physica B: Condensed Matter*, vol. 438, pp. 1–8, 2014.

[28] C. M. Watts, X. Liu and W. J. Padilla, 'Metamaterial electromagnetic wave absorbers', *Advanced materials*, vol. 24, no. 23, OP98–OP120, 2012.

[29] C. M. Bingham, H. Tao, X. Liu, R. D. Averitt, X. Zhang and W. J. Padilla, 'Planar wallpaper group metamaterials for novel terahertz applications', *Optics Express*, vol. 16, no. 23, pp. 18 565–18 575, 2008.

[30] H.-T. Chen, W. J. Padilla, J. M. Zide, A. C. Gossard, A. J. Taylor and R. D. Averitt, 'Active terahertz metamaterial devices', *Nature*, vol. 444, no. 7119, pp. 597–600, 2006.

[31] J. B. Pendry, 'Negative refraction makes a perfect lens', *Physical review letters*, vol. 85, no. 18, p. 3966, 2000.

[32] D. Schurig, J. J. Mock, B. Justice, S. A. Cummer, J. B. Pendry, A. F. Starr and D. R. Smith, 'Metamaterial electromagnetic cloak at microwave frequencies', *Science*, vol. 314, no. 5801, pp. 977–980, 2006.

[33] D. Shrekenhamer, J. Montoya, S. Krishna and W. J. Padilla, 'Four-color metamaterial absorber THz spatial light modulator', *Advanced Optical Materials*, vol. 1, no. 12, pp. 905–909, 2013.

[34] N. Meinzer, W. L. Barnes and I. R. Hooper, 'Plasmonic meta-atoms and metasurfaces', *Nature Photonics*, vol. 8, no. 12, pp. 889–898, 2014.

[35] H.-T. Chen, A. J. Taylor and N. Yu, 'A review of metasurfaces: Physics and applications', *Reports on Progress in Physics*, vol. 79, no. 7, p. 076 401, 2016.

[36] M. Decker, I. Staude, M. Falkner, J. Dominguez, D. N. Neshev, I. Brener, T. Pertsch and Y. S. Kivshar, 'High-efficiency dielectric Huygens' surfaces', *Advanced Optical Materials*, vol. 3, no. 6, pp. 813–820, 2015.

[37] W. Liu, S. Chen, Z. Li, H. Cheng, P. Yu, J. Li and J. Tian, 'Realization of broadband cross-polarization conversion in transmission mode in the terahertz region using a single-layer metasurface', *Optics Letters*, vol. 40, no. 13, pp. 3185–3188, 2015.

[38] N. Yu, F. Aieta, P. Genevet, M. A. Kats, Z. Gaburro and F. Capasso, 'A broadband, background-free quarter-wave plate based on plasmonic metasurfaces', *Nano Letters*, vol. 12, no. 12, pp. 6328–6333, 2012.

[39] K. Konstantinidis, A. P. Feresidis and P. S. Hall, 'Broadband sub-wavelength profile high-gain antennas based on multi-layer metasurfaces', *IEEE Transactions on Antennas and Propagation*, vol. 63, no. 1, pp. 423–427, 2014.

[40] Z. Wei, Y. Cao, X. Su, Z. Gong, Y. Long and H. Li, 'Highly efficient beam steering with a transparent metasurface', *Optics express*, vol. 21, no. 9, pp. 10 739–10 745, 2013.

[41] P.-C. Li and E. T. Yu, 'Flexible, low-loss, large-area, wide-angle, wavelength-selective plasmonic multilayer metasurface', *Journal of Applied Physics*, vol. 114, no. 13, p. 133 104, 2013.

[42] C. R. Simovski, 'On electromagnetic characterization and homogenization of nanostructured metamaterials', *Journal of Optics*, vol. 13, no. 1, p. 013 001, 2010.

[43] E. F. Kuester, M. A. Mohamed, M. Piket-May and C. L. Holloway, 'Averaged transition conditions for electromagnetic fields at a metafilm', *IEEE Transactions on Antennas and Propagation*, vol. 51, no. 10, pp. 2641–2651, 2003.

[44] Y. Zhao, N. Engheta and A. Alù, 'Homogenization of plasmonic metasurfaces modeled as transmission-line loads', *Metamaterials*, vol. 5, no. 2-3, pp. 90–96, 2011.

[45] G. Valerio, Z. Sipus, A. Grbic and O. Quevedo-Teruel, 'Accurate equivalent-circuit descriptions of thin glide-symmetric corrugated metasurfaces', *IEEE Transactions on Antennas and Propagation*, vol. 65, no. 5, pp. 2695–2700, 2017.

[46] D. L. Sounas, T. Kodera and C. Caloz, 'Electromagnetic modeling of a magnetless nonreciprocal gyrotropic metasurface', *IEEE Transactions on Antennas and Propagation*, vol. 61, no. 1, pp. 221–231, 2012.

[47] S. Sun, K.-Y. Yang, C.-M. Wang, T.-K. Juan, W. T. Chen, C. Y. Liao, Q. He, S. Xiao, W.-T. Kung, G.-Y. Guo *et al.*, 'High-efficiency broadband anomalous reflection by gradient metasurfaces', *Nano Letters*, vol. 12, no. 12, pp. 6223–6229, 2012.

[48] C. Pfeiffer, N. K. Emani, A. M. Shaltout, A. Boltasseva, V. M. Shalaev and A. Grbic, 'Efficient light bending with isotropic metamaterial Huygens' surfaces', *Nano Letters*, vol. 14, no. 5, pp. 2491–2497, 2014.

[49] F. Monticone, N. M. Estakhri and A. Alu, 'Full control of nanoscale optical transmission with a composite metascreen', *Physical Review Letters*, vol. 110, no. 20, p. 203 903, 2013.

[50] H. Cheng, S. Chen, P. Yu, W. Liu, Z. Li, J. Li, B. Xie and J. Tian, 'Dynamically tunable broadband infrared anomalous refraction based on graphene metasurfaces', *Advanced Optical Materials*, vol. 3, no. 12, pp. 1744–1749, 2015.

[51] A. Belardini, F. Pannone, G. Leahu, M. Larciprete, M. Centini, C. Sibilia, C. Martella, M. Giordano, D. Chiappe and F. B. de Mongeot, 'Asymmetric transmission and anomalous refraction in metal nanowires metasurface', *Journal of the European Optical Society-Rapid Publications*, vol. 7, 2012.

[52] *Https://zhuanlan.zhihu.com/p/345457427*.

[53] T. J. Cui, M. Q. Qi, X. Wan, J. Zhao and Q. Cheng, 'Coding metamaterials, digital metamaterials and programmable metamaterials', *Light: Science & Applications*, vol. 3, no. 10, e218–e218, 2014.

[54] M. Di Renzo, A. Zappone, M. Debbah, M.-S. Alouini, C. Yuen, J. De Rosny and S. Tretyakov, 'Smart radio environments empowered by reconfigurable intelligent surfaces: How it works, state of research, and the road ahead', *IEEE Journal on Selected Areas in Communications*, vol. 38, no. 11, pp. 2450–2525, 2020.

[55] B. O. Zhu, J. Zhao and Y. Feng, 'Active impedance metasurface with full 360 reflection phase tuning', *Scientific Reports*, vol. 3, no. 1, pp. 1–6, 2013.

[56] H. Yang, X. Chen, F. Yang, S. Xu, X. Cao, M. Li and J. Gao, 'Design of resistor-loaded reflectarray elements for both amplitude and phase control', *IEEE Antennas and Wireless Propagation Letters*, vol. 16, pp. 1159–1162, 2016.

[57] M. E. Bialkowski, A. W. Robinson and H. J. Song, 'Design, development, and testing of X-band amplifying reflectarrays', *IEEE Transactions on Antennas and Propagation*, vol. 50, no. 8, pp. 1065–1076, 2002.

[58] A. Costanzo and D. Masotti, 'Wirelessly powering: An enabling technology for zero-power sensors, iot and d2d communication', in *2015 IEEE MTT-S International Microwave Symposium*, IEEE, 2015, pp. 1–4.

[59] C. C. Cruz, J. R. Costa and C. A. Fernandes, 'Hybrid uhf/uwb antenna for passive indoor identification and localization systems', *IEEE Transactions on Antennas and Propagation*, vol. 61, no. 1, pp. 354–361, 2012.

[60] N. Decarli, A. Guerra, F. Guidi, M. Chiani, D. Dardari, A. Costanzo, M. Fantuzzi, D. Masotti, S. Bartoletti, J. S. Dehkordi *et al.*, 'The greta architecture for energy efficient radio identification and localization', in *2015 International EURASIP Workshop on RFID Technology (EURFID)*, IEEE, 2015, pp. 1–8.

[61] A. Costanzo, D. Dardari, J. Aleksandravicius, N. Decarli, M. Del Prete, D. Fabbri, M. Fantuzzi, A. Guerra, D. Masotti, M. Pizzotti *et al.*, 'Energy autonomous uwb localization', *IEEE Journal of Radio Frequency Identification*, vol. 1, no. 3, pp. 228–244, 2017.

[62] N. Decarli, M. Del Prete, D. Masotti, D. Dardari and A. Costanzo, 'High-accuracy localization of passive tags with multisine excitations', *IEEE Transactions on Microwave Theory and Techniques*, vol. 66, no. 12, pp. 5894–5908, 2018.

[63] M. Fantuzzi, D. Masotti and A. Costanzo, 'A novel integrated UWB–UHF one-port antenna for localization and energy harvesting', *IEEE Transactions on Antennas and Propagation*, vol. 63, no. 9, pp. 3839–3848, 2015.

[64] S. Agarwal, A. Costanzo and D. Masotti, 'Dual-purpose metasurface for background insensitive uwb tag', in *2021 15th European Conference on Antennas and Propagation (EuCAP)*, IEEE, 2021, pp. 1–5.

[65] W. Wiesbeck, G. Adamiuk and C. Sturm, 'Basic properties and design principles of uwb antennas', *Proceedings of the IEEE*, vol. 97, no. 2, pp. 372–385, 2009.

[66] C. A. Balanis, *Antenna theory: Analysis and Design*. John wiley & sons, 2016.

[67] D. F. Sievenpiper, 'High-impedance electromagnetic surfaces.', 2000.

[68] J. Sarrazin, A.-C. Lepage and X. Begaud, 'Circular high-impedance surfaces characterization', *IEEE Antennas and Wireless Propagation Letters*, vol. 11, pp. 260–263, 2012.

[69] M. A. Amiri, C. A. Balanis and C. R. Birtcher, 'Analysis, design, and measurements of circularly symmetric high-impedance surfaces for loop antenna applications', *IEEE Transactions on Antennas and Propagation*, vol. 64, no. 2, pp. 618–629, 2016.

[70] S. Clavijo, R. E. Diaz and W. E. McKinzie, 'Design methodology for sievenpiper high-impedance surfaces: An artificial magnetic conductor for positive gain electrically small antennas', *IEEE transactions on antennas and propagation*, vol. 51, no. 10, pp. 2678–2690, 2003.

[71] T. B. Lim and L. Zhu, 'Compact microstrip-to-cps transition for uwb application', in *2008 IEEE MTT-S International Microwave Workshop Series on Art of Miniaturizing RF and Microwave Passive Components*, IEEE, 2008, pp. 153–156.

[72] M. A. Ziai and C. B. John, 'Uwb/uhf rfid tag', in *2015 Loughborough Antennas & Propagation Conference (LAPC)*, IEEE, 2015, pp. 1–3.

[73] W. An, Z. Shen and J. Wang, 'Compact low-profile dual-band tag antenna for indoor positioning systems', *IEEE Antennas and Wireless Propagation Letters*, vol. 16, pp. 400–403, 2016.

[74] X. Shan and Z. Shen, 'Miniaturized uhf/uwb tag antenna for indoor positioning systems', *IEEE Antennas and Wireless Propagation Letters*, vol. 18, no. 12, pp. 2453–2457, 2019.

[75] X. Gao and Z. Shen, 'Uhf/uwb tag antenna of circular polarization', *IEEE Transactions on Antennas and Propagation*, vol. 64, no. 9, pp. 3794–3802, 2016.

[76] N. Zhang, X. Li, H. Zhu, G. Gao and Z. Qi, 'Compact and circular polarization uhf/uwb rfid reader antenna', in *2019 IEEE Asia-Pacific Microwave Conference (APMC)*, IEEE, 2019, pp. 1337–1339.

[77] M. I. Khan and F. A. Tahir, 'An angularly stable dual-broadband anisotropic cross polarization conversion metasurface', *Journal of Applied Physics*, vol. 122, no. 5, p. 053 103, 2017.

[78] B. Lin, B. Wang, W. Meng, X. Da, W. Li, Y. Fang and Z. Zhu, 'Dual-band high-efficiency polarization converter using an anisotropic metasurface', *Journal of Applied Physics*, vol. 119, no. 18, p. 183 103, 2016.

[79] M. Murtaza, A. Rashid, T. Ullah, F. A. Tahir and S. A. A. Zaidi, 'An angularly stable broadband cross-polarization conversion metasurface', in *2019 13th European Conference on Antennas and Propagation (EuCAP)*, IEEE, 2019, pp. 1–3.

[80] H. Chen, H. Ma, S. Qu, J. Wang, Y. Li, H. Yuan and Z. Xu, 'Ultra-wideband polarization conversion metasurfaces', in *Proceedings of 2014 3rd Asia-Pacific Conference on Antennas and Propagation*, IEEE, 2014, pp. 1009–1011.

[81] H. Chen, J. Wang, H. Ma, S. Qu, Z. Xu, A. Zhang, M. Yan and Y. Li, 'Ultra-wideband polarization conversion metasurfaces based on multiple plasmon resonances', *Journal of Applied Physics*, vol. 115, no. 15, p. 154 504, 2014.

[82] M. I. Khan and F. A. Tahir, 'A broadband cross-polarization conversion anisotropic metasurface based on multiple plasmon resonances', *Chinese Physics B*, vol. 27, no. 1, p. 014 101, 2018.

[83] M. I. Khan, Z. Khalid and F. A. Tahir, 'Linear and circular-polarization conversion in x-band using anisotropic metasurface', *Scientific reports*, vol. 9, no. 1, pp. 1–11, 2019.

[84] F. A. Tahir *et al.*, 'A broadband metasurface for cross polarization conversion applications', in *2019 IEEE International Conference on Computational Electromagnetics (ICCEM)*, IEEE, 2019, pp. 1–2.

[85] R. Izhar, M. Wahidi, F. A. Tahir *et al.*, 'An anisotropic dual-broadband cpc metasurface', in *2019 International Conference on Microwave and Millimeter Wave Technology (ICMMT)*, IEEE, 2019, pp. 1–2.

[86] R. Izhar, M. Wahidi, F. A. Tahir, Q. H. Abbasi *et al.*, 'A broadband polarization rotator metasurface', in *2019 International Conference on Microwave and Millimeter Wave Technology (ICMMT)*, IEEE, 2019, pp. 1–2.

[87] N. Katsarakis, T. Koschny, M. Kafesaki, E. Economou and C. Soukoulis, 'Electric coupling to the magnetic resonance of split ring resonators', *Applied physics letters*, vol. 84, no. 15, pp. 2943–2945, 2004.

[88] S. Bhattacharyya, 'An ultra-thin wide-angle cross polarization conversion metasurface with enhanced bandwidth', in *2017 International Symposium on Antennas and Propagation (ISAP)*, IEEE, 2017, pp. 1–2.

[89] R. A. Shelby, D. R. Smith and S. Schultz, 'Experimental verification of a negative index of refraction', *science*, vol. 292, no. 5514, pp. 77–79, 2001.

[90] C. M. Soukoulis and M. Wegener, 'Past achievements and future challenges in the development of three-dimensional photonic metamaterials', *Nature photonics*, vol. 5, no. 9, pp. 523–530, 2011.

[91] C. Qu, S. Ma, J. Hao, M. Qiu, X. Li, S. Xiao, Z. Miao, N. Dai, Q. He, S. Sun *et al.*, 'Tailor the functionalities of metasurfaces based on a complete phase diagram', *Physical review letters*, vol. 115, no. 23, p. 235 503, 2015.

[92] L. Wang, S. Ge, W. Hu, M. Nakajima and Y. Lu, 'Graphene-assisted high-efficiency liquid crystal tunable terahertz metamaterial absorber', *Optics Express*, vol. 25, no. 20, pp. 23 873–23 879, 2017.

[93] H.-X. Xu, S. Tang, S. Ma, W. Luo, T. Cai, S. Sun, Q. He and L. Zhou, 'Tunable microwave metasurfaces for high-performance operations: Dispersion compensation and dynamical switch', *Scientific reports*, vol. 6, no. 1, pp. 1–10, 2016.

[94] F. Liu, O. Tsilipakos, A. Pitilakis, A. C. Tasolamprou, M. S. Mirmoosa, N. V. Kantartzis, D.-H. Kwon, J. Georgiou, K. Kossifos, M. A. Antoniades *et al.*, 'Intelligent metasurfaces with continuously tunable local surface impedance for multiple reconfigurable functions', *Physical Review Applied*, vol. 11, no. 4, p. 044 024, 2019.

[95] H. Yang, X. Cao, F. Yang, J. Gao, S. Xu, M. Li, X. Chen, Y. Zhao, Y. Zheng and S. Li, 'A programmable metasurface with dynamic polarization, scattering and focusing control', *Scientific reports*, vol. 6, no. 1, pp. 1–11, 2016.

[96] K. M. Kossifos, L. Petrou, G. Varnava, A. Pitilakis, O. Tsilipakos, F. Liu, P. Karousios, A. C. Tasolamprou, M. Seckel, D. Manessis *et al.*, 'Toward the realization of a programmable metasurface absorber enabled by custom integrated circuit technology', *IEEE Access*, vol. 8, pp. 92 986–92 998, 2020.

[97] L. Li, T. Jun Cui, W. Ji, S. Liu, J. Ding, X. Wan, Y. Bo Li, M. Jiang, C.-W. Qiu and S. Zhang, 'Electromagnetic reprogrammable coding-metasurface holograms', *Nature communications*, vol. 8, no. 1, pp. 1–7, 2017.

[98] X. Wan, M. Q. Qi, T. Y. Chen and T. J. Cui, 'Field-programmable beam reconfiguring based on digitally-controlled coding metasurface', *Scientific reports*, vol. 6, no. 1, pp. 1–8, 2016.

[99] H. Jiang, Y. Cui and Y. Jiang, 'Two-dimensional tunable polarization-dependent absorptions for binary and ternary coding', *Optical Materials Express*, vol. 10, no. 3, pp. 787–795, 2020.

[100] H.-X. Xu, S. Sun, S. Tang, S. Ma, Q. He, G.-M. Wang, T. Cai, H.-P. Li and L. Zhou, 'Dynamical control on helicity of electromagnetic waves by tunable metasurfaces', *Scientific reports*, vol. 6, no. 1, pp. 1–10, 2016.

[101] Z. Tao, X. Wan, B. C. Pan and T. J. Cui, 'Reconfigurable conversions of reflection, transmission, and polarization states using active metasurface', *Applied Physics Letters*, vol. 110, no. 12, p. 121 901, 2017.

[102] A. Li, S. Kim, Y. Luo, Y. Li, J. Long and D. F. Sievenpiper, 'High-power transistor-based tunable and switchable metasurface absorber', *IEEE Transactions on Microwave Theory and Techniques*, vol. 65, no. 8, pp. 2810–2818, 2017.

[103] F. Zhang, W. Zhang, Q. Zhao, J. Sun, K. Qiu, J. Zhou and D. Lippens, 'Electrically controllable fishnet metamaterial based on nematic liquid crystal', *Optics express*, vol. 19, no. 2, pp. 1563–1568, 2011.

[104] K. M. Kossifos, M. A. Antoniades, J. Georgiou, A. H. Jaafar and N. T. Kemp, 'An optically-programmable absorbing metasurface', in *2018 IEEE International Symposium on Circuits and Systems (ISCAS)*, IEEE, 2018, pp. 1–5.

[105] X. Chen, Z. Tian, Y. Lu, Y. Xu, X. Zhang, C. Ouyang, J. Gu, J. Han and W. Zhang, 'Electrically tunable perfect terahertz absorber based on a graphene salisbury screen hybrid metasurface', *Advanced Optical Materials*, vol. 8, no. 3, p. 1 900 660, 2020.

[106] C. Huang, A. Zappone, G. C. Alexandropoulos, M. Debbah and C. Yuen, 'Reconfigurable intelligent surfaces for energy efficiency in wireless communication', *IEEE Transactions on Wireless Communications*, vol. 18, no. 8, pp. 4157–4170, 2019.

[107] M. Di Renzo, A. Zappone, M. Debbah, M.-S. Alouini, C. Yuen, J. De Rosny and S. Tretyakov, 'Smart radio environments empowered by reconfigurable intelligent surfaces: How it works, state of research, and the road ahead', *IEEE journal on selected areas in communications*, vol. 38, no. 11, pp. 2450–2525, 2020.

[108] M. A. ElMossallamy, H. Zhang, L. Song, K. G. Seddik, Z. Han and G. Y. Li, 'Reconfigurable intelligent surfaces for wireless communications: Principles, challenges, and opportunities', *IEEE Transactions on Cognitive Communications and Networking*, vol. 6, no. 3, pp. 990–1002, 2020.

[109] C. Molero, Á. Palomares-Caballero, A. Alex-Amor, I. Parellada-Serrano, F. Gamiz, P. Padilla and J. F. Valenzuela-Valdés, 'Metamaterial-based reconfigurable intelligent surface: 3d meta-atoms controlled by graphene structures', *IEEE Communications Magazine*, vol. 59, no. 6, pp. 42–48, 2021.

[110] A. Elzanaty, A. Guerra, F. Guidi and M.-S. Alouini, 'Reconfigurable intelligent surfaces for localization: Position and orientation error bounds', *IEEE Transactions on Signal Processing*, vol. 69, pp. 5386–5402, 2021.

[111] S. Kisseleff, W. A. Martins, H. Al-Hraishawi, S. Chatzinotas and B. Ottersten, 'Reconfigurable intelligent surfaces for smart cities: Research challenges and opportunities', *IEEE Open Journal of the Communications Society*, vol. 1, pp. 1781–1797, 2020.

[112] M. Faenzi, G. Minatti, D. González-Ovejero, F. Caminita, E. Martini, C. Della Giovampaola and S. Maci, 'Metasurface antennas: New models, applications and realizations', *Scientific reports*, vol. 9, no. 1, pp. 1–14, 2019.

[113] A. Shahvarpour, A. A. Melcon and C. Caloz, 'Anisotropic meta-substrate conical-beam leaky-wave antenna', in *2010 Asia-Pacific Microwave Conference*, IEEE, 2010, pp. 299–302.

[114] M. Caiazzo, S. Maci and N. Engheta, 'A metamaterial surface for compact cavity resonators', *IEEE Antennas and Wireless Propagation Letters*, vol. 3, no. 1, pp. 261–264, 2004.

[115] R. A. York, 'Tunable dielectrics for rf circuits', *Multifunctional adaptive microwave circuits and systems*, vol. 1, pp. 159–207, 2009.

[116] W. D. Palmer, 'Tunable dielectrics for rf circuits', 2009.

[117] M. Aldrigo, M. Dragoman, E. Laudadio, S. Iordanescu, M. Modreanu, I. Povey, F. Nastase, S. Vulpe, P. Stipa, A. Di Donato *et al.*, 'Microwave applications of zirconium-doped hafnium oxide ferroelectrics: From nanoscale calculations up to experimental results', in *2020 IEEE/MTT-S International Microwave Symposium (IMS)*, IEEE, 2020, pp. 520–523.

[118] F. P. Casares-Miranda, P. Otero, E. Marquez-Segura and C. Camacho-Penalosa, 'Wire bonded interdigital capacitor', *IEEE Microwave and Wireless Components Letters*, vol. 15, no. 10, pp. 700–702, 2005.

[119] A. Di Florio-Di Renzo, S. Trovarello, M. Aldrigo, D. Masotti, M. Dragoman and A. Costanzo, 'Nonlinear circuit model of idcs on ferroelectric nanomaterial for reconfigurable applications', in *2022 European Microwave Conference (EuMC)*, IEEE, 2022.